DISCLAIMER FOR FRONT PAGE OF MATERIALS TO BE MADE AVAILABLE VIA ETI INTERNET SITE

1. "Save to the extent set out in paragraph 2 below, this document and its contents are made available to you via the ETI's Internet Site "as is" without any representations, conditions, warranties or other assurance of any kind. The ETI and the authors, together with their employees, directors, servants or agents exclude to the maximum extent permissible by law all representations, warranties, conditions or other assurance whatsoever (whether express or implied) regarding the use of this document or its content including any warranties of title, merchantability, accuracy, completeness, non-infringement or that the document or its contents are of satisfactory or any particular quality or fit for any particular purpose. Any person accessing this document and using it or any of its contents accepts all risk in doing so.

2. Notwithstanding any statement to the contrary contained on the face of this document, the ETI confirms that the authors of the document have consented to its publication by the ETI."

Energy Technologies Institute

PerAWaT

WG3 WP1 D4: PERFORMANCE AND WAKE STRUCTURE OF A FULL-SCALE HORIZONTAL AXIS AXIAL FLOW TURBINE

Authors	C. F. Fleming, S. C. McIntosh, R. H. J. Willden
Version	2.0
Date	16/11/12

Revision History		
Issue / Version	**Issue Date**	**Summary**
0.1	14/09/12	First draft for review by GH
0.2	28/09/12	Revision in line with GH review
1.0	07/11/12	Second revision in line with GH review
2.0	16/11/12	Minor additions requested by GH

Executive Summary

This report contains results and analysis of 3D RANS simulated flows through a generic full scale tidal turbine operating in various flow conditions. Conditions simulated include varying levels of shear, vertical position through the water column, turbine spacing and yaw angle. Additionally simulations of a towerless rotor are presented, including a comparison to the results of the University of Edinburgh model of the same towerless rotor. Results presented include thrust and power metrics as well as wake profiles. Results are analysed and contrasted with respect to perturbations in each flow condition leading to observations on their influence.

In particular shear is observed to increase the power delivered by the turbine (with mass flux through the channel held constant), as is increasing the elevation of the turbine through the shear profile. Additionally shear is observed to increase the rate of wake recovery. Reducing the lateral spacing, and therefore increasing the area blockage ratio, increases the thrust and power delivered by the turbine, consistent with existing theory. Removing the tower from the simulations increases the thrust and power experienced by the turbine, as well as removing the torque ripple. Lower power is extracted by the turbine when operating in yawed flows, and a lower thrust coefficient is observed. However, the blade loading is distinctly different from the unyawed cases, as shown in plots of azimuthally-distributed rotor torque.

Comparison to the University of Edinburgh simulation results is done on a consistent area blockage basis.

The turbine wake is parameterised by considering a force balance for a turbine operating in a confined flow, and converting the resulting 'top-hat' wake velocity profile into an Gaussian distribution with equivalent momentum and standard deviation. This model is valid at the end of the near-wake. The near-wake ends at a downstream location where the pressure has equalised in the cross-stream direction and the velocity profile exhibits a self-similar form. For the current set of simulations this point has been identified at a distance of five diameters downstream of the rotor plane.

Relationships between operating conditions and wake model parameters are determined.

All of the results presented here are based on unsteady blade-resolved simulations, where the simulated flow field has been averaged over one full rotor revolution. The full set of revolution-averaged flow field data generated in this study is available on the PerAWaT SFTP server.

This report fulfils the acceptance criteria for Deliverable WG3 WP1 D4, which are:

- Assessment of the influence of turbulence, flow profile, yaw angle and relative depth on performance and near wake structure of a bare and ducted axial flow turbine.

- Parameterisation of the simulated near-wakes.

Table of Contents

1 Introduction

This work forms deliverable D4 of Work Group 3 Work Package 1 of the PerAWaT project. Computational simulations are carried out on bare and ducted variants of an axial flow tidal turbine under a range of operating conditions. Device performance is examined for various degrees of flow shear, rotor elevation, lateral spacing (blockage), and yaw.

A semi-empirical model of the velocity deficit downstream of the turbine is developed, in a similar fashion to that of (Gretton, 2012). A Gaussian distribution of velocity, based on turbine thrust and blockage, is assumed at the end of the near-wake. The effect of the various operating conditions on the model parameters is investigated systematically.

Section 2 gives details of the computational model such as geometry and boundary conditions. Each of the parameters governing the operating conditions are presented and their range of values are tabulated. A comprehensive list of all simulations run is laid out.

The format and location of simulation results are described in Section 3. The general performance metrics are defined here.

The wake parameterisation is presented in Section 4. Firstly, the theoretical background of the model is explained, leading to a parametric description of the velocity profile at the end of the near wake. The model is compared to the simulation results, and model parameters for every simulated case are tabulated. Cases corresponding to particular flow conditions, such as shear or yaw, are isolated, and trends in the wake model parameters are highlighted.

The effect of each set of operating conditions upon turbine performance and wake recovery is analysed in Section 5. Notable physical flow features are identified in each case. This section also presents a comparison with the computational model carried out by the University of Edinburgh.

A comprehensive set of results from the computational and wake models is laid out in the appendix.

2 Simulation Details

2.1 Geometry

2.1.1 Rotor

The rotor geometry has been provided by the PerAWaT consortium. It is a three-bladed axial flow design, with a diameter of 18 m. The diameter of the nacelle and spinner is 3 m, and the spinner has an elliptical profile with a ratio of 1.5:1. The turbine geometry is described in detail in WG3 WP5 D1 (Gretton & Ingram, 2011).

2.1.2 Tower

The tower is a hollow steel cylinder with a diameter of 2 m and a thickness of 0.05 m. A simple design study was carried out, where the effects of regular and extreme wave loading was considered. The failure mode of the tower is buckling due to the overturning moment caused by the horizontal current and wave induced loads on the rotor and tower. The results are presented in Table 1, where u_∞ is the free-stream velocity, $u_{\text{wave max}}$ is the peak wave-induced velocity, H_d is the significant wave height, T is the wave period, λ is the wavelength, and d is the minimum tower diameter. The wave-induced velocity is calculated using the well-known Morison equation.

Table 1: Tower diameter for various loading cases.

Case	Description	u_∞ [m s^{-1}]	H_d [m]	T [s]	λ [m]	d [m]
A	No wave loading: Steady load due to current only (u_∞) on operating rotor	3	-	-	-	1.90
B	Regular operation: Instantaneous combined load due to u_∞ and $u_{\text{wave max}}$ on operating rotor. Current and wave loading on support structure.	3	2	3	14.08	1.91
C	Extreme wave event: Current and wave loading on support structure (turbine not operating)	3	8	6.01	56.4	0.09[*]

---

[*] The unfeasibly small tower diameter resulting from this calculation only shows that Case C is not the critical loading state for the turbine.

2.1.3 Computational Domain

The turbine is modelled in a domain of rectangular cross-section. The channel depth is constant at 36 m ($2D$). The width, W, and rotor elevation, H, are varied so that the effects of blockage and shear can be examined. Further details are given in Section 2.4. The upstream and downstream distances are set at $3D$ and $6D$ respectively, consistent with simulations in WG3 WP1 D1 (McIntosh, Fleming, & Willden, 2010).
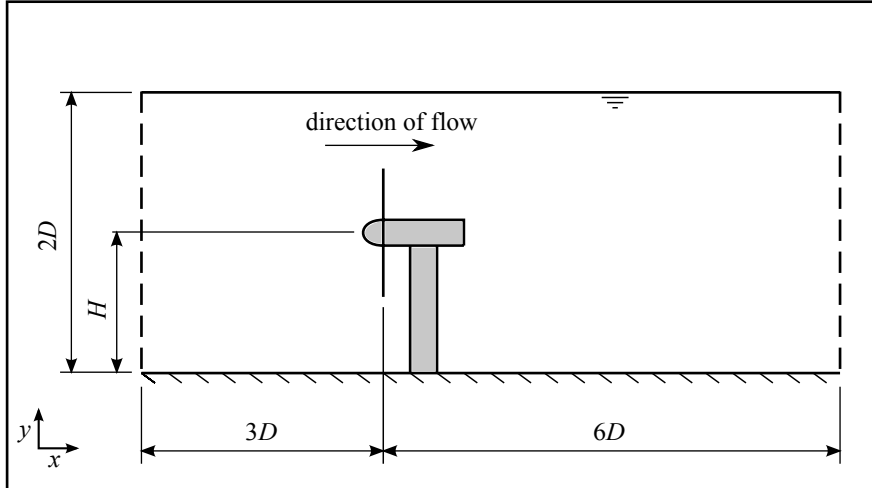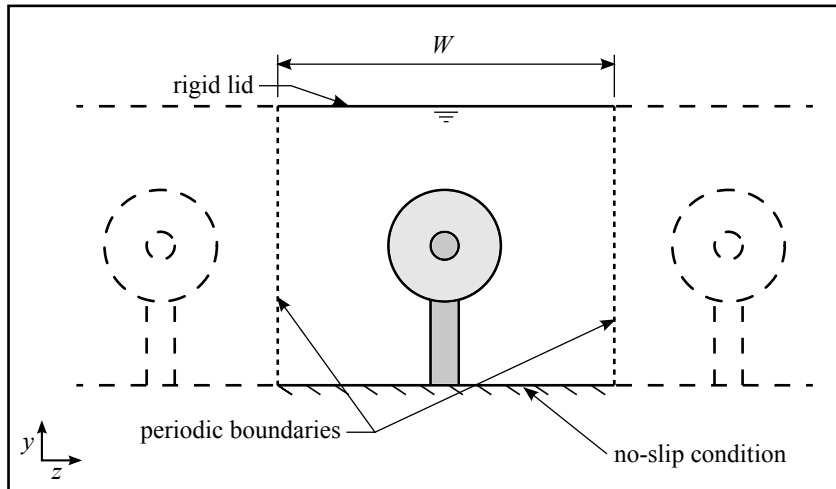
Figure 1: Elevation view of computational domain.

Figure 2: Axial view of computational domain.

2.2 Mesh

The mesh generation procedure is described in detail in deliverable WG3 WP1 D3 (Schlichting & Gersten, 2000). A cutplane through the rotor blade around the 80% radial station is shown in Figure 3. Mesh resolution at the blades is limited by available computational capacity. The wall-adjacent prism elements have a height corresponding to a non-dimensional distance of $100 < y^+ < 500$, and wall functions are used to model the boundary layer.
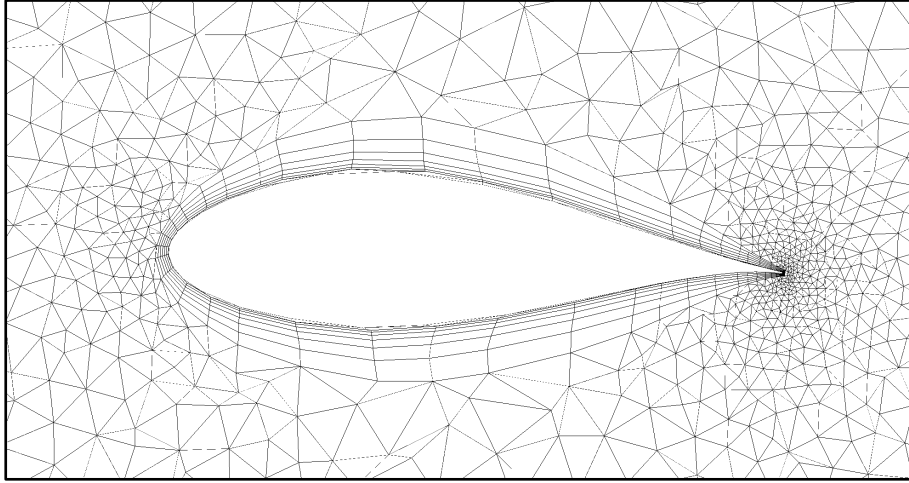

Figure 3: Cutplane showing mesh resolution in the vicinity of the rotor blade at radial distance $r = 0.8R$.

Mesh resolution in the rotor region is shown in Figure 4. The maximum tetrahedral element dimension in the far field is equivalent to $2c$, where c is the chord length of the rotor blade at the 80% radial station.
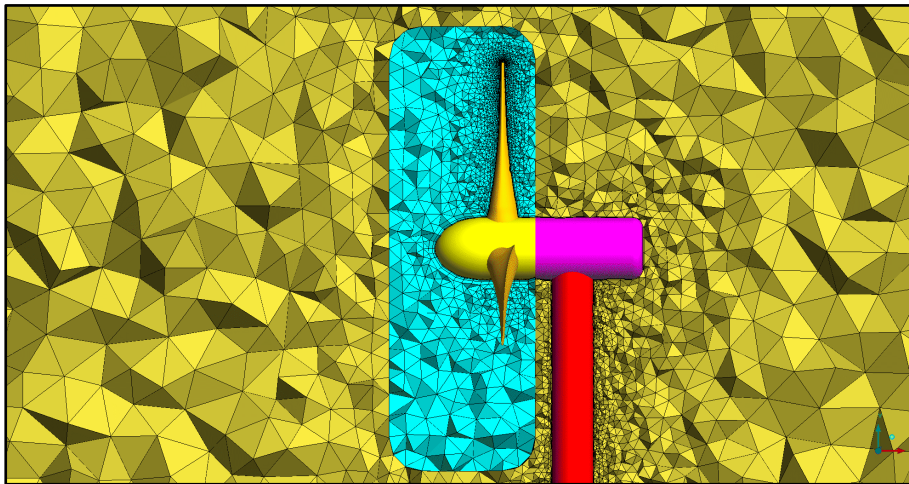

Figure 4: Vertical cutplane showing the mesh resolution in the rotor region.
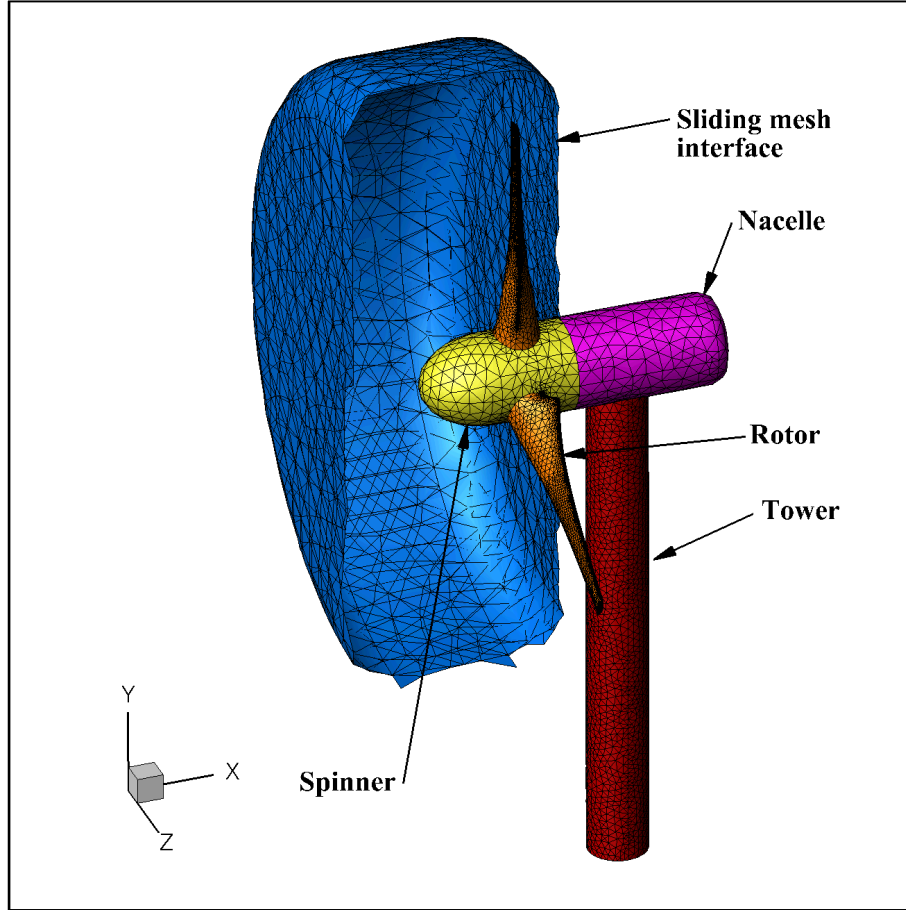
Figure 5: General arrangement of turbine, showing location of sliding mesh interface.

2.3 Computational Setup

2.3.1 Solver

The Reynolds Averaged Navier Stokes (RANS) equation solver ANSYS FLUENT is used. Turbulence is modelled with the $k - \omega$ SST model. This choice is based on work reported in WG3 WP1 D1 (McIntosh, Fleming, & Willden, 2010).

2.3.2 Sliding Mesh

Angular motion of the rotor is achieved via a sliding mesh technique available in ANSYS FLUENT. The rotor advances 2° every timestep. Temporal convergence is demonstrated in the torque history plots presented in the Appendix.

2.3.3 Sheared Velocity

Velocity and turbulence parameters are prescribed at the domain inlet. Where a velocity profile is prescribed, matching profiles of the turbulence model parameters are also prescribed, to produce meaningful values of turbulence intensity upstream of the turbine.

The velocity profile is set via a bed roughness coefficient, c_f and a reference velocity u_{nom}. The friction velocity u_τ follows,

$$u_\tau = u_{\text{nom}}\sqrt{\frac{c_f}{2}}, \tag{1}$$

from which the applied bed shear, τ_w, is calculated,

$$\tau_w = \rho u_\tau |u_\tau|. \tag{2}$$

The sheared velocity profile (as a function of $\eta \equiv y/d$, where d is the water depth) is assumed to take the form of one half of a fully-developed Poiseuille flow, where the shear force $\tau(\eta)$ drops linearly from a wall-maximum of τ_w to a minimum of 0 at the free-surface.

$$\tau(\eta) = \tau_w(1-\eta) = \mu_t \frac{du}{d\eta}\frac{d\eta}{dy} \tag{3}$$

Taking the ansatz for eddy viscosity (Schlichting & Gersten, 2000),

$$\nu_t = \frac{1}{6}u_\tau d\kappa(1-(1-\eta)^2)(1+2(1-\eta)^2), \tag{4}$$

Eq. (3) can be integrated to yield the velocity profile for a turbulent Poiseuille flow,

$$u(\eta) = \frac{u_\tau}{\kappa}\ln\left(\frac{\eta(2-\eta)}{2\eta^2-4\eta+3}\right) + u_h, \tag{5}$$

where $\kappa = 0.41$ is the Kármán constant and u_h is the streamwise velocity at the free-surface.

The profile is defined in terms of the average velocity across the channel, u_{nom}

$$u_{\text{nom}} = \int_0^1 u(\eta)d\eta \tag{6}$$

which is solved for u_h,

$$u_h = u_{\text{nom}} - \bar{c} \tag{7}$$

where,

$$\bar{c} = \frac{u_\tau}{\kappa}\left(\ln\left(\frac{4}{3}\right) - \frac{\pi}{\sqrt{2}} + \sqrt{2}\,\text{atan}\frac{1}{\sqrt{2}}\right) \tag{8}$$

The profile of turbulent kinetic energy k is defined as

$$k = \frac{\tau_t}{a\,\rho} = \frac{u_\tau^2(1-\eta)}{a}, \tag{9}$$

where $a = 0.3$ is a turbulence constant (Schlichting & Gersten, 2000). A definition for turbulence intensity follows,

$$TI = 100\sqrt{\frac{2}{3}k}. \tag{10}$$

The specific dissipation rate of the turbulence, ω, is defined as

$$\omega = \frac{k}{\nu_t}, \tag{11}$$
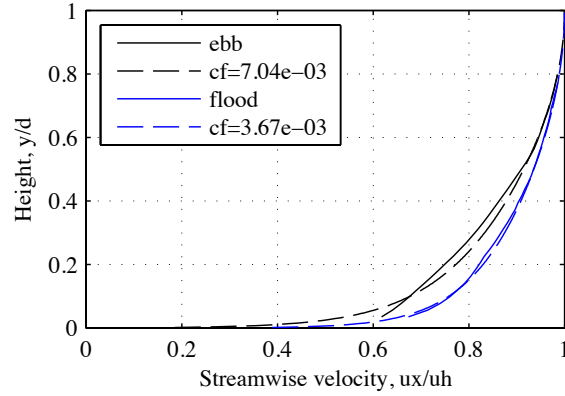
where ν_t is the turbulent eddy viscosity.

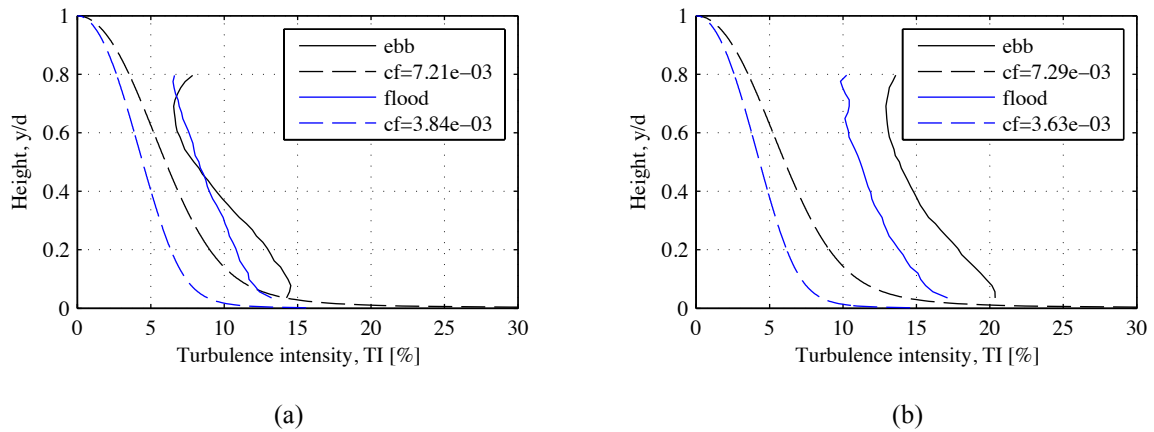Figure 6: Time averaged velocity profile for the Fall of Warness compared to analytical profile described by Eq. (5).

(a)

(b)

Figure 7: Time averaged turbulence intensity profiles for the Fall of Warness compared to analytical profile described by Eq. (10), where a high-pass filter with cut-offs of one minute (a) and one hour (b) is applied to the raw data.

Three velocity profiles, identified as S0, S1 and S2, are employed in this work. Profile S0 corresponds to uniform flow, while S1 and S2 are sheared profiles. The degree of shear for these profiles is based on measurements from a site at the Fall of Warness (data obtained from EMEC, see Figure 6), with profile S1 corresponding to the ebb tide and profile S2 corresponding to the flood tide. Figure 7 illustrates profiles of turbulence intensity for the same flow. The raw velocity signals are filtered to separate the tidal harmonics from the turbulent fluctuations. A high-pass filter is applied with a cut-off of one minute and one hour. For both cases, fluctuations in the tidal data are higher than the analytical predictions. It is suggested that mechanisms for turbulent production, additional to bed shear, occur in real tidal flows that are not accounted for in the current model. Whilst not achieving as close a match to the experimental data as that seen for the velocity profiles, the analytical turbulence profiles are considered sufficient for the current work; producing representative values with the required dependence on bed shear.

An upstream nominal velocity of $u_{nom} = 2$ m s^{-1} is set for all simulations. For uniform flow, the upstream velocity is equal to this nominal velocity. In the sheared flow cases, where the velocity is a function of vertical position, the mass flow is constrained to be equal to that of the uniform flow case.

2.3.4 Periodic Sides

A periodic boundary condition is prescribed at both sides of the computational domain, simulating an infinite fence of turbines. The domain width, W, is varied to enable investigation of blockage effects.

The periodic boundary condition also enables simulation of the turbine in yawed flow. For a high yaw angle, the wake flow may pass out of the domain through one side. In this situation, an identical adjacent wake will pass into the domain through the other side.

2.3.5 Free Surface

Two methods of modelling the free surface – volume of fluid (VOF) and rigid-lid – were investigated in WG3 WP1 D1-3. The rigid lid model was found to represent the free surface sufficiently for the operating conditions studied, and hence is used here.

2.3.6 Pressure Outlet

A constant pressure of 0 Pa is applied at the outlet boundary, based on previous work in deliverable WG3 WP1 D1.

2.4 Simulation Stencil

The effects of shear, turbine elevation, turbine spacing, yawed flow and support structure are investigated in this study. The values of these parameters are tabulated in the following subsections. The effects of these parameters on turbine performance are discussed in Section 5.

2.4.1 Shear

As explained in Section 2.3.3, a sheared velocity profile is maintained by applying shear stress to the flow at the channel bed. The values of skin friction coefficient corresponding to each shear level are tabulated below.

Table 2: Shear levels and skin friction coefficients.

Label	Description	Skin friction coefficient, c_f
S0	Uniform flow	0
S1	Ebb tide	0.0035
S2	Flood tide	0.007

2.4.2 Nacelle Height

It is expected that the performance of a turbine in a sheared flow will be affected by vertical position. A turbine positioned near the free surface will encounter faster flow and should produce more power than a turbine positioned near the channel bed. The turbine heights tested are shown relative to rotor diameter, D, in Table 3.

Table 3: Turbine height relative to rotor diameter.

Label	Description	Nacelle height, y/D
H0	Low	0.35
H1	Mid-depth	0.5
H2	High	0.65

2.4.3 Lateral Spacing

The effect of blockage on turbine performance is examined by changing the centre-to-centre spacing of the turbines. This equates to altering the width of the computational domain, due to the employment of periodic boundary conditions at the side walls.

Table 4: Domain width and area blockage for different values of lateral turbine spacing.

Label	Description	Domain width, w/D	Area blockage, B
W0	Narrow domain	1.5	0.2618
W1	Wide domain	4	0.0982

2.4.4 Yaw

Two yawed flow cases are set up to enable the effect of yaw to be examined.

Table 5: Shear levels and skin friction coefficients.

Label	Description	Yaw angle, α
Y0	Axial flow	0°
Y1	Low yaw angle	15°
Y2	High yaw angle	30°

2.4.5 Tower

The turbine is simulated with no tower (Case M1) for one operating case, so that the effect of the supporting structure can be determined. Label *T0* corresponds to cases with no tower, and cases with a tower (base case) are labelled *T1*.

2.4.6 Comparison With University of Edinburgh Model

One aim within the PerAWaT project is to validate numerical results by cross-comparing independent results from participants. The present turbine model is to be compared with the model developed at the University of Edinburgh (Gretton & Ingram, 2011). One significant difference between the Oxford and Edinburgh models is the domain cross-section. The domain of the Edinburgh model has a circular cross-section, while the domain of the model presented here has a rectangular cross-section. This difference is considered to be only of secondary importance if overall blockage remains low and is matched between models (Nishino & Willden, 2012). We therefore select the Edinburgh model with a $4R$ domain radius, where R is the rotor radius, yielding an area blockage of $B = 0.0625$, which remains in the plausible realm of real installations.

Table 6: Domain width and area blockage for different values of lateral turbine spacing.

Label	Description	Domain width, w/D	Area blockage, B
W2	Edinburgh comparison	6.27	0.0625

2.4.7 Ducted Rotor Simulations

A ducted rotor is simulated in a subset of the operating conditions described above. Specifically, the effects of the following parameters are examined:

   i.   Shear

  ii.   Nacelle Height

 iii.   Lateral Spacing

 iv.   Yaw

2.4.8 Table of Simulations

The parameters discussed above are varied systematically to produce a range of simulation cases. These cases, labelled alphabetically, are tabulated in Table 7. Simulations are carried out at tip speed ratios, λ, of 3.5, 4.5 and 5.5 for each case, where

$$\lambda = \frac{u_{\text{tip}}}{u_{\text{nom}}}. \tag{12}$$

Table 7: Matrix of blade-resolved simulations presented in this document.

	Shear S	Nacelle height H	Width W	Yaw Y	Tower T	Length L	Duct D
Cases	0, 1, 2	0, 1, 2	0, 1, 2	0, 1, 2	0, 1	0, 1	0, 1
Baseline Case (BC)	2	1	1	0	1	0	0
A	BC	BC	BC	BC	BC	BC	BC
B	0	BC	BC	BC	BC	BC	BC
C	1	BC	BC	BC	BC	BC	BC
D	BC	0	BC	BC	BC	BC	BC
E	0	0	BC	BC	BC	BC	BC
F	1	0	BC	BC	BC	BC	BC
G	BC	2	BC	BC	BC	BC	BC
H	0	2	BC	BC	BC	BC	BC
I	1	2	BC	BC	BC	BC	BC
J	BC	BC	0	BC	BC	BC	BC
K	BC	BC	BC	1	BC	BC	BC
L	BC	BC	BC	2	BC	BC	BC
M1	BC	BC	BC	BC	0	BC	BC

	Shear S	Nacelle height H	Width W	Yaw Y	Tower T	Length L	Duct D
Cases	0, 1, 2	0, 1, 2	0, 1, 2	0, 1, 2	0, 1	0, 1	0, 1
Baseline Case (BC)	2	1	1	0	1	0	0
M2	BC[†]	BC	2[‡]	BC	0	BC	BC
N	BC	BC	BC	BC	BC	1	BC
O	BC	BC	BC	BC	BC	BC	1
P	0	BC	BC	BC	BC	BC	1
Q	1	BC	BC	BC	BC	BC	1
R	BC	0	BC	BC	BC	BC	1
S	BC	2	BC	BC	BC	BC	1
T	BC	BC	0	BC	BC	BC	1
U	BC	BC	BC	1	BC	BC	1
V	BC	BC	BC	2	BC	BC	1

[†] The sheared base-case velocity profile is inappropriate, as fair comparison with the University of Edinburgh model is prevented. This issue is being addressed through the inclusion of an additional case with a uniform velocity profile.

[‡] The width of the channel is set to achieve a blockage equivalent to that of the University of Edinburgh model.

3   Presentation of Data

Results for each simulation case are presented in the attached Appendix (Section 7). The data presented has been averaged over the final three revolutions of the turbine. This data is available from the PerAWaT SFTP server at the following URL:

```
sftp://engs-waves.eng.ox.ac.uk:/home/PerAWaT/WorkGroups/WG3/WP1/D4/Data/
wake_data/
```

and is organised by case, consistent with Table 7.

Temporal convergence of the model is determined when fluctuations of the force coefficients exhibit periodicity corresponding to the angular velocity of the rotor. The model continues to run for at least three revolutions beyond the point of temporal convergence. The reported rotor force coefficients (Section 3.1) are the average of the unsteady force coefficients sampled over the final three periodic revolutions of the rotor.

The instantaneous flow field is written to file every five timesteps (10˚) during the final revolution. The resulting thirty-six sets of data are averaged to produce a time-averaged flow field corresponding to one full revolution of the turbine. The wake velocity deficit (Section 3.2) is calculated from this time-averaged flow field.

3.1   Force Coefficients

The streamwise thrust on the rotor, spinner and nacelle, T, is reported in normalised form,

$$C_T = \frac{T}{\frac{1}{2}\rho u_{\text{nom}}^2 \pi R^2},\tag{13}$$

where C_T is the coefficient of thrust, u_{nom} is the nominal velocity (defined in Section 2.3.3), and R is the rotor radius. Note that we exclude the tower thrust from the reported thrust coefficient. The mechanical power extracted by the rotor and spinner is reported in a similar form.

$$C_P = \frac{P}{\frac{1}{2}\rho u_{\text{nom}}^3 \pi R^2},\tag{14}$$

Torque histories are presented for the final three revolutions of the turbine for each case. The torque coefficient is defined as

$$C_Q = \frac{Q}{\frac{1}{2}\rho u_{\text{nom}}^2 \pi R^3},\tag{15}$$

where Q is torque. Note that $C_Q = \frac{C_P}{\lambda}$.

3.2 Wake Velocity Deficit

The velocity deficit in the wake is presented in normalised form, allowing fair comparison between sheared and non-sheared flow cases. The quantity $u_{\text{def nor}}$ is defined as

$$u_{\text{def nor}} = 1 - \frac{u(y)}{u_\infty(y)},$$

(16)

where $u(y)$ is the velocity at a given downstream location, and $u_\infty(y)$ is the prescribed velocity profile.

4 Wake Parameterisation

The velocity deficit in the near wake is parameterised via a least squares fit to a Gaussian profile, defined as

$$u = u_{b4} - (u_{b4} - u_{cl})e^{\frac{-r^2}{2\sigma^2}},$$

(17)

where r is the radial position, u_{4b} is the bypass flow velocity, u_{4cl} is the centreline flow velocity and σ is the standard deviation. The variables u_{4b} and u_{4t} are calculated via an inversion of Linear Momentum Actuator Disk Theory (LMADT) for a turbine operating in a constrained flow (Houlsby, Draper, & Oldfield, 2008). The arrangement is illustrated in Figure 8 below, where the velocities are labelled according to location.

Figure 8: One dimensional linear momentum actuator disc theory in a finite medium bounded by a parallel-sided tube, taken from Houlsby, Draper, & Oldfield (2008).

The following set of equations is solved numerically, producing values of velocity coefficients α_2, α_4 and β_4 for a prescribed turbine thrust C_x and flow blockage B,

$$\alpha_2 = \frac{(1 + \alpha_4)}{(1 + B) + \sqrt{(1 - B)^2 + B(1 - 1/\alpha_4)^2}},$$ (18)

$$\beta_4 = \frac{(1 - B\alpha_2)}{(1 - B\,\alpha_2/\alpha_4)},$$ (19)

$$C_x = \beta_4^2 - \alpha_4^2.$$ (20)

These equations are solved by finding a root of the following equation which lies on the interval $0 - 1$.

$$\frac{\alpha_4\left(\alpha_4 + B\alpha_4 - (B^2\alpha_4^2 - B\alpha_4^2 - 2B\alpha_4 + B + \alpha_4^2)^{\frac{1}{2}}\right)}{B(3\alpha_4 - 1)} - \frac{\alpha_4}{B}$$
$$- \frac{\alpha_4\left(\alpha_4 + (\alpha_4^2 + C_x)^{\frac{1}{2}}\right)(\alpha_4 - 1)}{BC_x} = 0$$ (21)

The velocity coefficients relate the flow velocities at the rotor plane and in the wake to the upstream flow velocity.

$$u_{t2} = \alpha_2 u_1$$ (22)

$$u_{t4} = \alpha_4 u_1$$ (23)

$$u_{b4} = \beta_4 u_1$$ (24)

Note that for sheared flow, u_1 is equivalent to the nominal velocity, u_{nom}, defined previously.

The inversion of LMADT produces a top-hat profile at station 4 (see Figure 8). Here it is assumed that static pressure has attained a constant value across the wake (parallel streamlines). This method of predicting the near wake deficit is similar to that detailed by Gretton (2012), but differs in the technique used for mapping the theoretical top-hat profile to the assumed Gaussian distribution. In this case the Gaussian profile (17) is determined by matching the standard deviation (width) and momentum (deficit) of the top-hat distribution.

The standard deviation of a top-hat profile is defined as follows

$$\sigma^2 = \frac{\int_0^{r_d} u(r)r^2 \mathrm{d}r}{\int_0^{r_d} u(r)dr}$$ (25)

$$\sigma = \frac{r_d}{\sqrt{3}}$$ (26)

where r_d is the radius of a circular domain of equivalent area to the channel. Combining Eq. (26) with the Gaussian profile in Eq. (17) yields

$$u = u_{4b} - (u_{4b} - u_{4cl})e^{-\frac{3r^2}{2r_d^2}} \tag{27}$$

The momentum of the top hat profile is

$$M_{LMADT} = \pi\rho(u_{4t}^2 r_t^2 + u_{4b}^2 r_d^2 - u_{b4}^2 r_t^2) \tag{28}$$

The momentum of the Gaussian profile is

$$M_{GAUSS} = \pi\rho(u_{4b}r_d^2 - 4(u_{b4} - u_{cl})u_{4t}\sigma^2 + (u_{b4} - u_{cl})^2\sigma) \tag{29}$$

Equating Eq. (28) with Eq. (29) produces the relation

$$(u_{b4} - u_{cl}) = 2u_{b4} - (-r_t^2 u_{b4}^2 + r_t^2 u_{t4}^2 + 4\sigma^2 u_{b4}^2)^{\frac{1}{2}} \tag{30}$$

which is solved for u_{cl}, thus fully defining the parameterised profile.

4.1 Results of Wake Parameterisation

The accuracy of this model is now assessed via comparison to a least-squares fit to the simulation data at a station located five diameters downstream of the rotor plane. Constants for both profiles are tabulated below (Table 8, Table 9, Table 10). Wake profiles, comparing the parametric model, to the simulation data and associated least-squares Gaussian given in the Appendix.

Table 8: Wake parameterisation constants comparing least squares Gaussian fit to the Gaussian wake model, Eq. (17), 5D downstream of rotor plane (λ=3.5).

Case	ID	u_{4b}		u_{cl}		σ	
		fit	model	fit	model	fit	model
A	BC	2.22	2.23	0.82	0.87	0.68	0.58
B	S0	2.13	2.12	0.64	0.82	0.67	0.58
C	S1	2.21	2.2	0.78	0.85	0.67	0.58
D	H0	2.1	2.09	0.81	0.81	0.68	0.58
E	S0 H0	2.13	2.12	0.63	0.83	0.7	0.58
F	S1 H0	2.11	2.1	0.78	0.82	0.67	0.58
G	H2	2.32	2.34	0.78	0.92	0.69	0.58
H	S0 H2	2.14	2.12	0.61	0.83	0.69	0.58
I	S1 H2	2.28	2.27	0.73	0.89	0.69	0.58

Case	ID	u_{4b} fit	model	u_{cl} fit	model	σ fit	model
J	W0	2.3	2.41	1.02	1.07	0.64	0.58
K	Y1	2.2	2.22	0.97	0.97	0.65	0.58
L	Y2	2.17	2.18	1.33	1.22	0.6	0.58

Table 9: Wake parameterisation constants comparing least squares Gaussian fit to the Gaussian wake model, Eq. (17), 5D downstream of rotor plane (λ=4.5).

Case	ID	u_{4b}		u_{cl}		σ	
		fit	model	fit	model	fit	model
A	BC	2.24	2.25	0.74	0.76	0.7	0.58
B	S0	2.15	2.14	0.61	0.72	0.72	0.58
C	S1	2.22	2.22	0.73	0.75	0.7	0.58
D	H0	2.12	2.11	0.75	0.71	0.71	0.58
E	S0 H0	2.15	2.14	0.59	0.73	0.75	0.58
F	S1 H0	2.13	2.12	0.69	0.72	0.73	0.58
G	H2	2.34	2.36	0.69	0.81	0.71	0.58
H	S0 H2	2.16	2.14	0.56	0.72	0.72	0.58
I	S1 H2	2.3	2.29	0.67	0.78	0.72	0.58
J	W0	2.32	2.45	0.96	0.98	0.66	0.58
K	Y1	2.22	2.24	0.9	0.86	0.64	0.58
L	Y2	2.18	2.2	1.33	1.13	0.58	0.58

Table 10: Wake parameterisation constants comparing least squares Gaussian fit to the Gaussian wake model, Eq. (17), 5D downstream of rotor plane (λ=5.5).

Case	ID	u_{4b}		u_{cl}		σ	
		fit	model	fit	model	fit	model
A	BC	2.25	2.27	0.79	0.69	0.73	0.58
B	S0	2.16	2.16	0.67	0.65	0.75	0.58
C	S1	2.23	2.24	0.75	0.67	0.74	0.58
D	H0	2.13	2.13	0.74	0.64	0.75	0.58
E	S0 H0	2.16	2.16	0.65	0.66	0.78	0.58

Case	ID	u_{4b} fit	model	u_{cl} fit	model	σ fit	model
F	S1 H0	2.14	2.13	0.73	0.65	0.77	0.58
G	H2	2.35	2.37	0.73	0.73	0.75	0.58
H	S0 H2	2.17	2.16	0.63	0.65	0.75	0.58
I	S1 H2	2.31	2.31	0.71	0.71	0.75	0.58
J	W0	2.32	2.48	1.01	0.91	0.67	0.58
K	Y1	2.23	2.25	0.93	0.79	0.68	0.58
L	Y2	2.19	2.2	1.34	1.07	0.58	0.58

4.2 Analysis of Wake Parameterisation

In this section, the influence of the following operating conditions on the end-of-near-wake velocity profile is discussed:

- bed shear

- turbine elevation

- tip speed ratio

- blockage

- yaw

The thrust coefficient C_x on which the velocity parameters (u_{t4}, u_{b4}, etc) in Eq. (21) are dependent is normalised on the root-mean square of the projected incident velocity profile (see Figure 10). Hence the force balance in Eqs. (18) and (20) is valid for sheared as well as uniform flows.

4.2.1 Bed Shear

Table 11: Effect of bed shear on near-wake parameters for λ = 4.5.

Case	ID	u_{4b}		u_{cl}		σ	
		fit	model	fit	model	fit	model
B	S0	2.15	2.14	0.61	0.72	0.72	0.58
C	S1	2.22	2.22	0.73	0.75	0.7	0.58
A	S2	2.22	2.23	0.82	0.87	0.68	0.58

Table 11 shows an increase in centreline and bypass velocities with increasing shear. This is consistent with elevated velocities at the inflow for increasing levels of shear. This effect is captured well by the analytical model.

4.2.2 Rotor Elevation

Table 12: Effect of rotor elevation on near-wake parameters for $\lambda = 4.5$.

Case	ID	u_{4b}		u_{cl}		σ	
		fit	model	fit	model	fit	model
D	H0	2.12	2.11	0.75	0.71	0.71	0.58
A	H1	2.22	2.23	0.82	0.87	0.68	0.58
G	H2	2.34	2.36	0.69	0.81	0.71	0.58

Table 12 shows an increase in bypass flow velocity with increasing shear, explained by moving up in the profile. No clear trend is visible for centreline velocity. It is suggested here that a non-linear coupling between turbine performance and velocity shear may be responsible.

4.2.3 Tip-speed-ratio

Table 13: Effect of tip speed ratio on near-wake parameters for the base case.

Case	λ	u_{4b}		u_{cl}		σ	
		fit	model	fit	model	fit	model
A	3.5	2.22	2.23	0.82	0.87	0.68	0.58
A	4.5	2.24	2.25	0.74	0.76	0.7	0.58
A	5.5	2.25	2.27	0.79	0.69	0.73	0.58

Table 13 shows the dependence of the form of the profile on tip-speed-ratio. Variations in centreline and bypass velocities are captured well by the analytical model. Changes in wake width (σ) are not captured – σ is assumed constant by the model. The assumption of a 'top-hat' deficit is only valid for turbines with a uniform radial loading. It is suggested that variations in wake width are due to non-uniformities in radial loading; a turbine specific property not captured by this general model.

4.2.4 Blockage

Table 14: Effect of blockage on near-wake parameters for λ = 4.5.

Case	ID	u_{4b}		u_{cl}		σ	
		fit	model	fit	model	fit	model
J	W0	2.32	2.45	0.96	0.98	0.66	0.58
A	W1	2.22	2.23	0.82	0.87	0.68	0.58

Table 14 shows an increase in both bypass and centreline velocities with increasing flow blockage. This is an expected result, well-captured by the analytical model.

4.2.5 Yaw

Table 15: Effect of yaw on near-wake parameters for λ = 4.5.

Case	ID	u_{4b}		u_{cl}		σ	
		fit	model	fit	model	fit	model
A	Y0	2.22	2.23	0.82	0.87	0.68	0.58
K	Y1	2.22	2.24	0.9	0.86	0.64	0.58
L	Y2	2.18	2.2	1.33	1.13	0.58	0.58

Table 15 shows the dependence of wake constants on flow yaw. Most notable is the decrease in cross-stream width (σ) with increasing yaw. The analytical model is unable to capture this effect.

5 Detailed Studies

In the following sections we detail comparisons of physical interest; the influence of flow shearing (uniform and two profiles considered), hub elevation (3 heights) through each of the these profiles, lateral spacing (and hence blockage) between turbines (two widths), flow yawing (unyawed and two yaw angles considered) and the presence or not of the tower.

Additionally we make comparison to the simulations of the University of Edinburgh performed as part of WP3 WP5. For these simulations the tower is removed, uniform flow is applied at the inlet boundary, and the width of our domain has been adjusted to present the same area blockage as achieved by the Edinburgh simulations (6.25% by area).

5.1 Velocity Profile
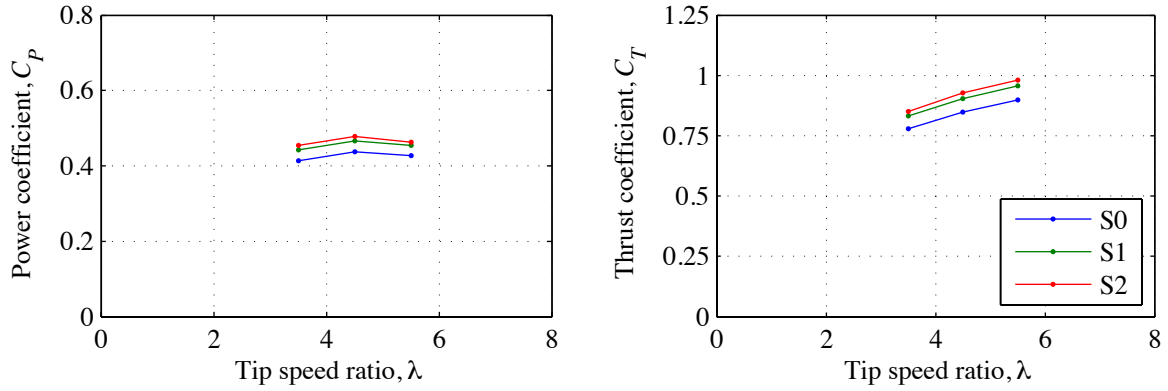
Figure 9: Power and thrust coefficients for three levels of shear.

Three profiles are considered;

i.   S0 – uniform flow (case B)

ii.   S1 – low shear (case C)

iii. S2 – high shear (case A) – Base Case

The three profiles deliver the same mass flux through the simulated channel. Increasing the level of shear is found to increase the power delivered by the turbine. Accordingly there is an increase in the thrust force experienced by the turbine. The increase in power generated is consistent with the increase in kinetic flux through the undisturbed stream through the turbine plane.
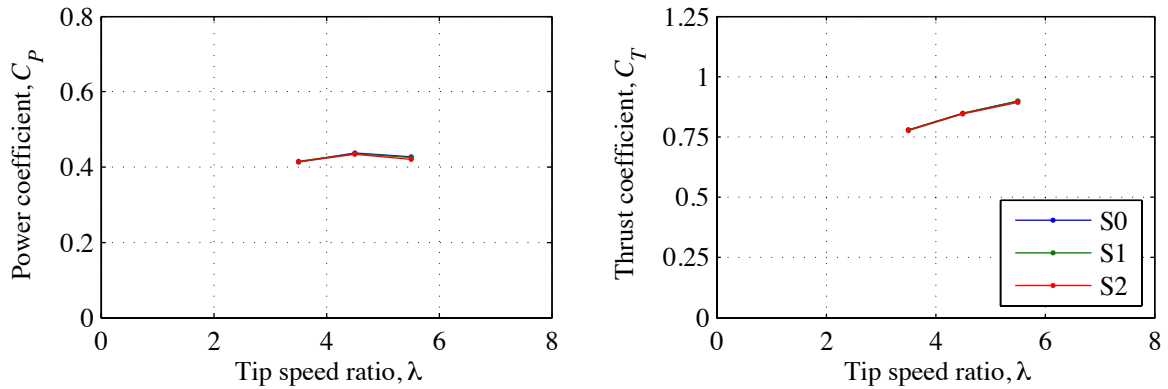
Figure 10: Power and thrust coefficients for three levels of shear.

Normalizing the power delivered on the mean cubed unperturbed velocity (as opposed to the cube of the average velocity) is found to collapse the power curve onto a single curve. Likewise the thrust curves can be collapsed in a similar manner as shown in the figures above. This is consistent with the findings when simulating the EDF flume 1/30th scale model (McIntosh, Fleming, & Willden, 2011).
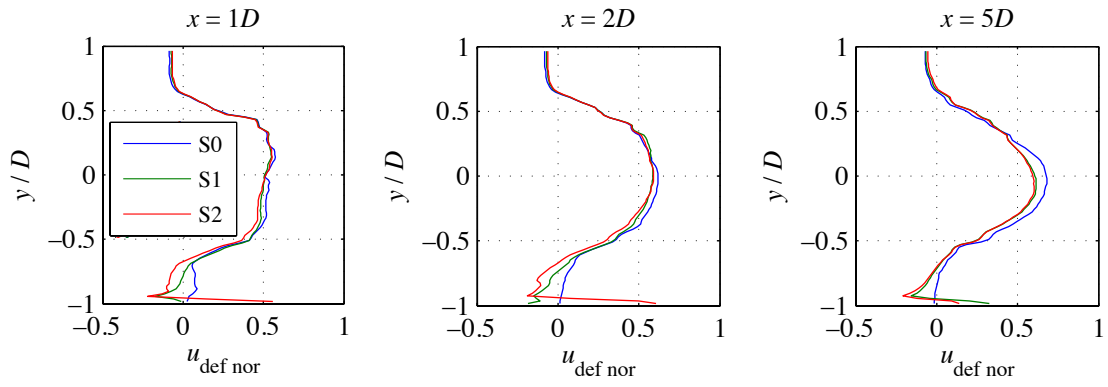
Figure 11: Distribution of normalised velocity deficit at the vertical midplane of the domain at various locations downstream of the turbine.

The centreline velocity deficit at the end of the near-wake (5D) is greater for the uniform flow case (S0) than for the sheared flow cases (S1, S2), as shown in Figure 11.

5.2 Turbine Elevation
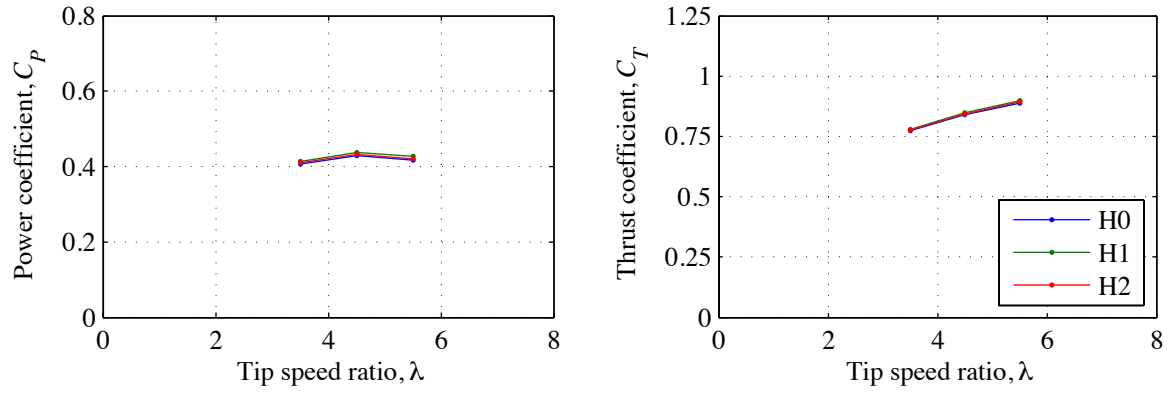
Figure 12: Power and thrust coefficients for three elevations in uniform flow (S0).
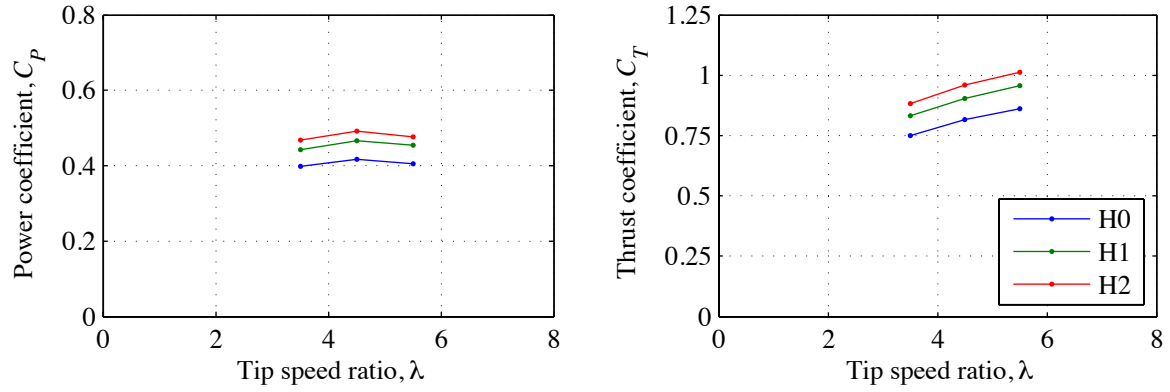
Figure 13: Power and thrust coefficients for three elevations in low shear (S1).
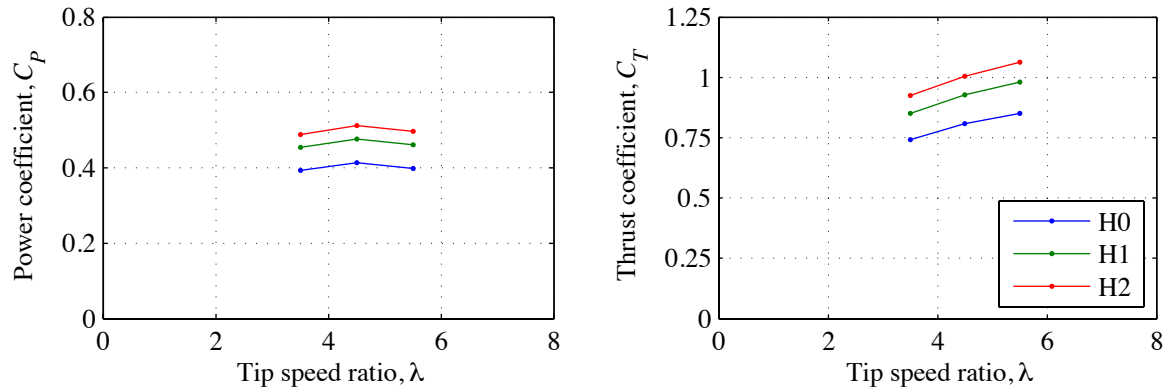
Figure 14: Power and thrust coefficients for three elevations in high shear (S2).

Three elevations are considered for each of the three profiles;

i. H0 – low elevation (cases E, F, D in increasing levels of shear)

ii. H1 – mid-depth elevation (cases B, C, A in increasing levels of shear)

iii. H2 – high elevation (cases H, I, G in increasing levels of shear)

As expected there is little dependency on turbine elevation for the uniform flow case, with force and power coefficients remaining relatively unchanged.

Moving the turbine up through the water column into high flow speeds results in a gradual and substantial increase in power and thrust.

For the high shear case (Figure 14), the peak power is increased by 24% between the lowest and highest elevations considered; $C_{P\,\mathrm{max}} = 0.4132$ and $C_{P\,\mathrm{max}} = 0.5124$ respectively. It should be noted that this difference in performance and turbine thrust is achieved for not unrealistic turbine positioning and shear conditions (Section 2.3.3) and likely reflects true performance range in realistic offshore conditions.

Raising the turbine through the sheared profile has little impact on the wake recovery as plotted in terms of $u_{\mathrm{def\,nor}}$ (see Figure 44, Figure 29 and Figure 59). There is however a significant increase in the magnitude of the torque ripple as the turbine moves up through the water column (see Figure 45, Figure 30 and Figure 60).

5.3 Lateral Spacing (Channel Width)
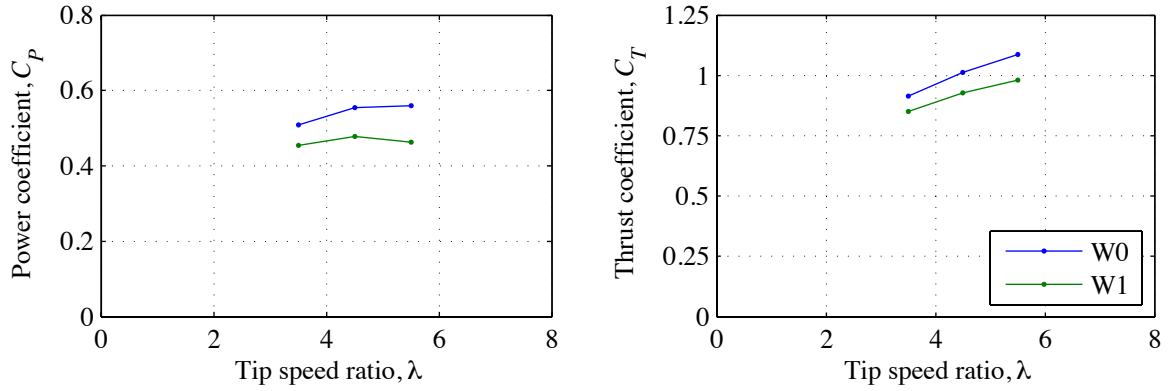
Figure 15: Power and thrust coefficients for two lateral spacings.

Two channel widths are considered;

i. W0 – narrow channel 1.5D (Case J)

ii. W1 – wide channel 4D (case A) – Base Case

The channel widths correspond to blockage ratios of 26.18% (1.5D), 9.82% (4D). As expected blockage has a substantial impact on the power extracted. Following theory by Garrett & Cummins (2007) in which maximum power is given by:

$$C_{P\,max} = C_{P\,Betz} \frac{1}{(1-B)^2} \tag{7}$$

Theoretical maximum performance for the given levels of blockage would therefore be $C_{P\,max} = 1.087$ and $C_{P\,max} = 0.729$ for the narrow and wide channels respectively. It also follows that for a real turbine we might expect an increase in power between the low and high blockage cases of circa 49%.

The recorded maximum powers are 0.560 and 0.477 respectively, which represents a considerably smaller uplift of 17.3%. The higher blockage channel allows the turbine to achieve a greater pressure drop and thus carry a larger thrust force (Nishino & Willden, 2012). Consequently the peak power operating point is shifted to a higher tip-speed-ratio for the narrower case. In fact, within the tip-speed-ratios considered the peak power has not yet been obtained (although it is unlikely to be considerably more than that already achieved). The narrow channel turbine achieves a higher core flow velocity than the wider channel turbine, which is consistent with blockage theory (see velocity traverses at 1D downstream of turbine). Also note that the bypass velocity is higher for the narrower case.

5.4 Yawed Flow
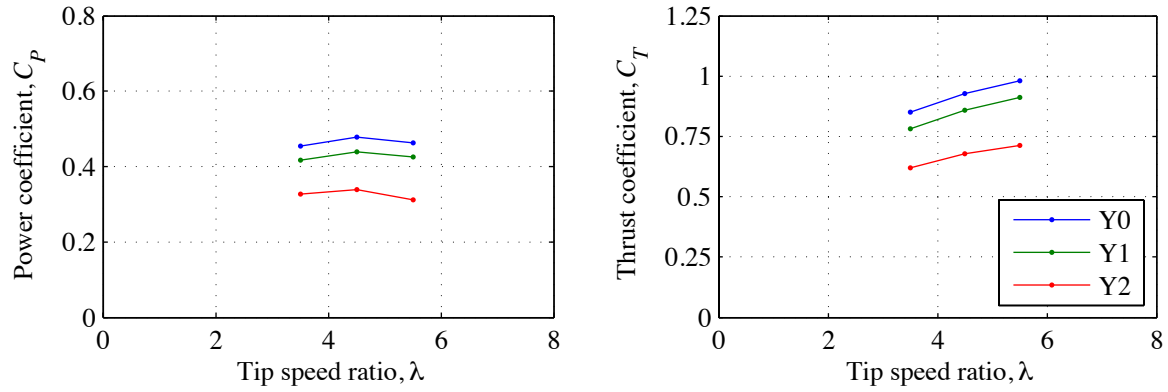
Figure 16: Effect of yaw. Y0 corresponds to a yaw angle of 0˚; Y1 corresponds to a yaw angle of 15˚; Y2 corresponds to a yaw angle of 30˚.

Two yaw angles were considered together with the unyawed base case.

   i.   Y0 – Unyawed base case (case A) – Base Case

   ii.   Y1 – Yaw angle 15˚ (case K)

   iii. Y2 - Yaw angle 30˚ (case L)

As expected the reduction in incident flow velocity normal to the turbine face leads to a reduction in the overall thrust and power coefficients for the turbine. However, it is possible that the individual rotor blades will undergo larger localised loading fluctuations when operating in yawed flows. The periodic fluctuation in torque for a single blade is shown in Figure 17 below. The rotor is operating in flow with a yaw of 15˚.
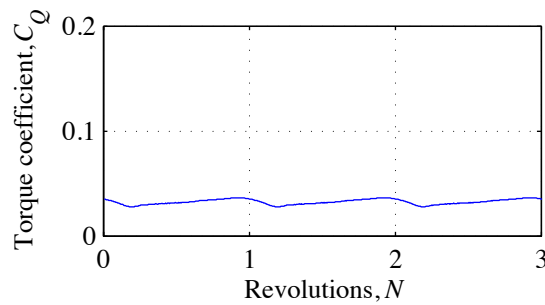
Figure 17: Torque on a single blade of a rotor operating at a 15˚ yaw angle for three revolutions.

5.5 Presence of Duct
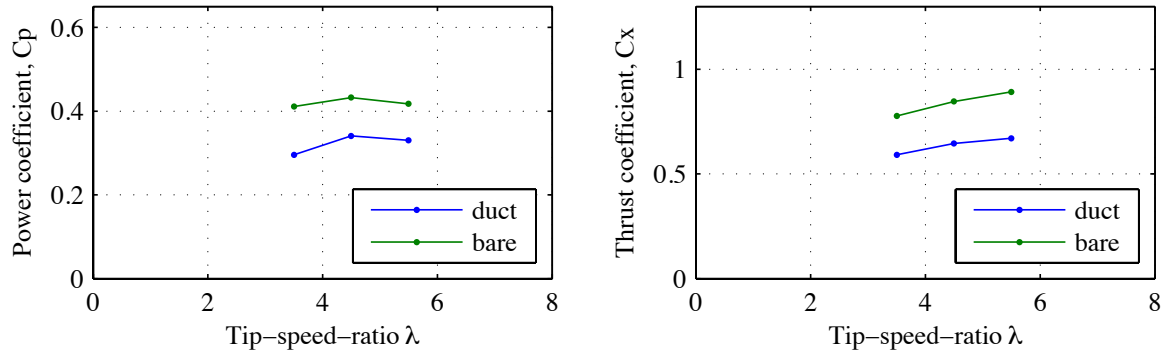
Figure 18: Power and thrust coefficients with and without a duct (base case, 0˚ yaw).

The presence of a duct is considered for a number of perturbations on the base case.

i. S2 – ducted base case (case M)

ii. S0 – ducted uniform flow (case N)

iii. S1 – ducted low shear (case O)

iv. H0 – ducted low elevation (cases P)

v. H2 – ducted high elevation (cases Q)

vi. W0 – ducted narrow channel 1.5D (Case R)

vii. Y1 – ducted low yaw angle 15˚ (case S)

viii. Y2 - ducted high yaw angle 30˚ (case T)

The primary influence of enclosing a rotor within a duct is the reduction of both power and stream-wise thrust developed by the rotor. This effect is illustrated by in Figure 18. Power and thrust coefficients are shown normalised by the overall frontal area presented by the device; the rotor diameter for the bare turbine and the outer duct diameter for the ducted rotor. The influence of a duct on rotor performance agrees with a previous ducted study documented in WG3WP1 D2.

Perturbations on the base case for the ducted device are found to follow a broadly similar pattern to the studies presented above for the bare rotor. Detailed performance metrics and wake parameterisations are given in the Appendix for each case.

A single significant departure in the similarity of the ducted / bare rotor perturbations is observed for the yawed flow simulations. Here, the duct appears to interact with the yawed flow, increasing the effective blockage.
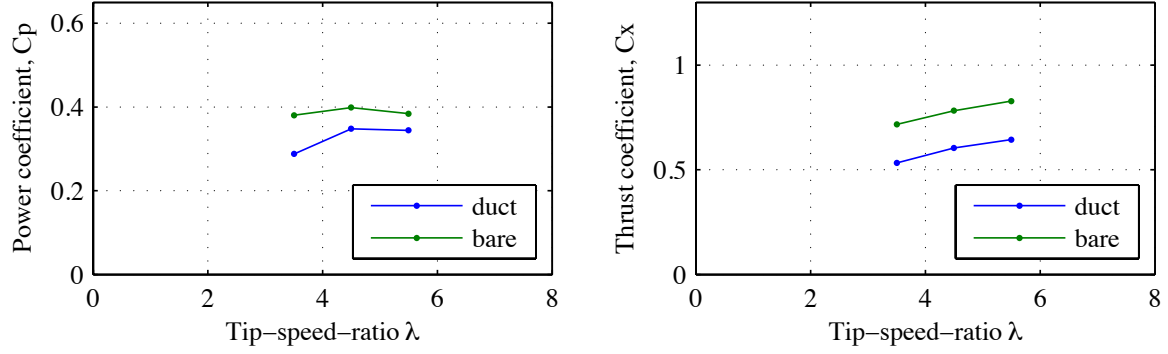
Figure 19: Power and thrust coefficients with and without a duct (base case, 15˚ yaw).

Figure 19 shows a comparison of power and thrust coefficients for the bare and ducted turbines operating in a 15˚ yawed flow. The bare turbine is shown to outperform the ducted device, although by a smaller margin than shown for the zero yaw flow case (Figure 18).
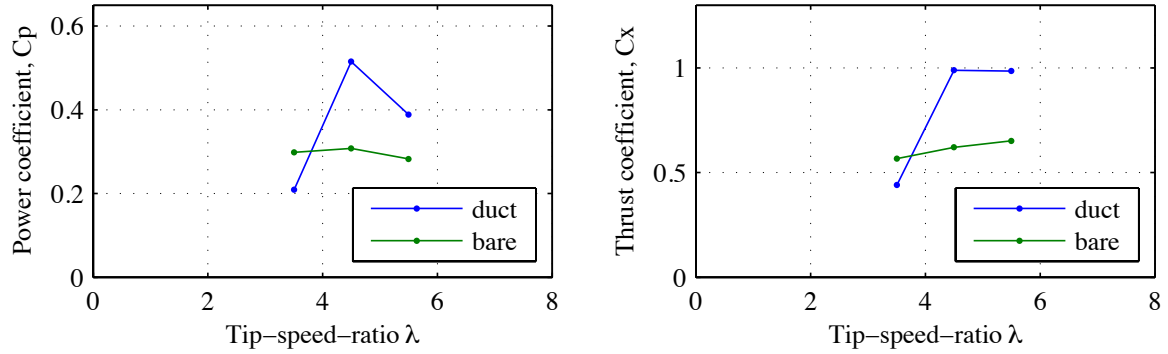
Figure 20: Power and thrust coefficients with and without a duct (base case, 30˚ yaw).

Increasing the yaw angle to 30˚ results in a marked increase in both rotor power extraction and axial thrust for the ducted device accompanied by a decrease in same metrics for the bare rotor (Figure 20). The appearance of a large-scale region of separated flow on the downstream side of the rotor ducting, and hence an associated increase in effective blockage, is considered responsible for this sharp increase in power extraction by the ducted device.

5.6 Presence of Tower
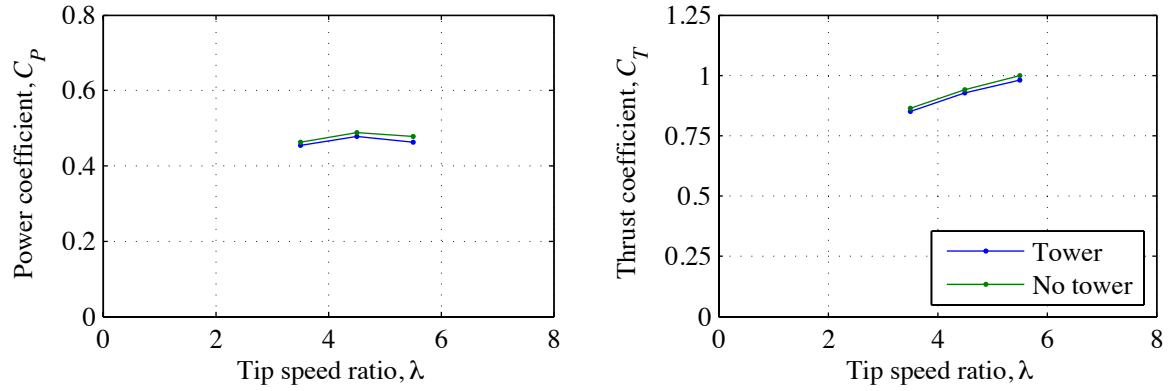
Figure 21: Power and thrust coefficients with and without the tower present.

Two cases are compared to determine the effect of the tower.

i.   With tower (case A) – Base Case

ii.   Without tower (case M1)

Note that the thrust coefficients shown above exclude the thrust force experienced by the tower. The tower, when present, acts as a momentum sink extracting energy from the flow. Removing the tower enables the towerless rotor to achieve a higher thrust and extract more power from the flow.

The wake behind the towerless rotor is relatively more dependent on tip speed ratio than that of the base case with tower (see particularly the lower portions of the vertical velocity traverses). The implication is that, particularly, in the lower part of the water column, the tower has a more dominant effect on the flow field than tip speed ratio.
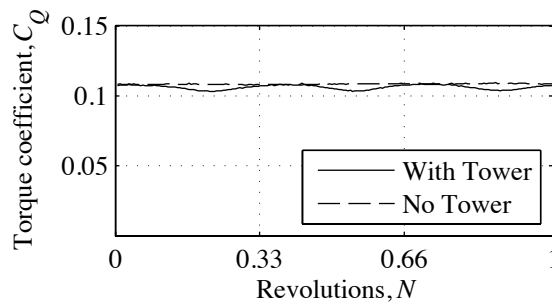
Figure 22: Comparison of case A (with tower) and case M1 (with no tower), showing the periodic effect of the tower on the rotor torque.

The towerless rotor is, as expected, observed to have no torque ripple, as shown in Figure 22 above. Note that for the base case the magnitude of the torque fluctuation is approximately 5% of the mean value.

5.7 Comparison With University of Edinburgh Model
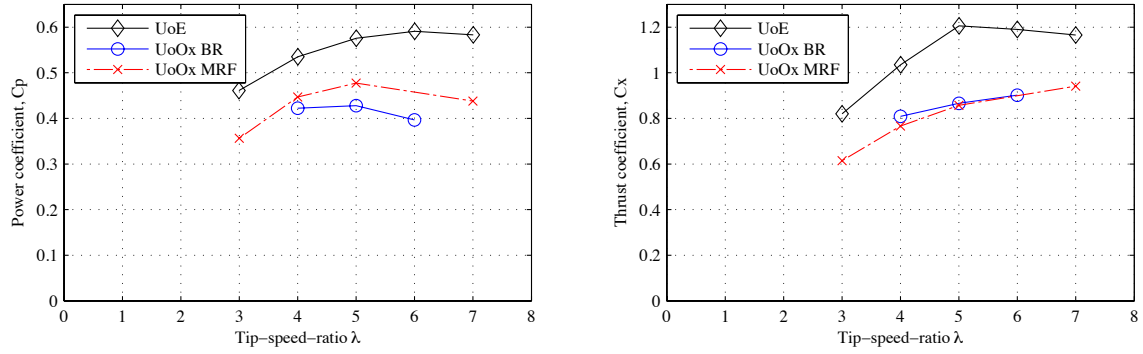
Figure 23: Power and thrust coefficients for the M2 case and the University of Edinburgh model.

A special case with an area blockage ratio equal to that of the University of Edinburgh simulation has been conducted. This is designated case M2 and labelled "UoOx BR" in Figure 23. Agreement between the "UoOx BR" and "UoE" simulations is considered poor. To further investigate this mismatch a new model, "UoOx MRF", was constructed. This model comprises a moving reference frame rotor enclosed in a $4R$ cylindrical domain. Mesh resolution was matched as closely as possible to the "UoE" case. There is a good agreement in thrust between the "UoOx BR" and "UoOx MRF" simulations. Agreement in power is less satisfactory.

6 References

Fleming, C. F., McIntosh, S. C., & Willden, R. H. (2011). WG3 WP1 D2: Report on model setup for ducted horizontal-axis axial flow turbines.

Garrett, C., & Cummins, P. (2007). The efficiency of a turbine in a tidal channel. Journal of Fluid Mechanics.

Gretton, G. I. (2012). WG3 WP5 D3: A parameterization of the end-of-near-wake region for a 'conventional' low solidity and an open-centre high-solidity tidal current turbine. University of Edinburgh.

Gretton, G. I., & Ingram, D. M. (2011). WG3 WP5 D1: Development of a computational fluid dynamics model for a horizontal axis tidal current turbine. University of Edinburgh.

Houlsby, G. T., Draper, S., & Oldfield, M. L. (2008). Application of linear momentum actuator disc theory to open channel flow. University of Oxford, Department of Engineering Science. University of Oxford.

McIntosh, S. C., Fleming, C. F., & Willden, R. H. (2011). Optimal axial flow tidal turbine design. Proc. 9th European Wave and Tidal Energy Conference. Southampton.

McIntosh, S. C., Fleming, C. F., & Willden, R. H. (2010). WG3 WP1 D1: Report on Model Setup for Horizontal Axis Axial Flow Turbines. University of Oxford.

McIntosh, S. C., Fleming, C. F., & Willden, R. H. (2011). WG3 WP1 D3: Performance and wake structure of a model horizontal axis axial flow turbine. University of Oxford.

Nishino, T., & Willden, R. H. (2012). Effects of 3D channel blockage and turbulent wake mixing on the limit of power extraction by tidal turbines. Int. J. Heat Fluid Flow .

Schlichting, H., & Gersten, K. (2000). Boundary Layer Theory, 8th Edition. Springer.

7 Appendix

Table 16: Matrix of blade-resolved simulations presented in this document.

	Shear S	Nacelle height H	Width W	Yaw Y	Tower T	Length L	Duct D
Cases	0, 1, 2	0, 1, 2	0, 1, 2	0, 1, 2	0, 1	0, 1	0, 1
Baseline Case (BC)	2	1	1	0	1	0	0
A	BC	BC	BC	BC	BC	BC	BC
B	0	BC	BC	BC	BC	BC	BC
C	1	BC	BC	BC	BC	BC	BC
D	BC	0	BC	BC	BC	BC	BC
E	0	0	BC	BC	BC	BC	BC
F	1	0	BC	BC	BC	BC	BC
G	BC	2	BC	BC	BC	BC	BC
H	0	2	BC	BC	BC	BC	BC
I	1	2	BC	BC	BC	BC	BC
J	BC	BC	0	BC	BC	BC	BC
K	BC	BC	BC	1	BC	BC	BC
L	BC	BC	BC	2	BC	BC	BC
M1	BC	BC	BC	BC	0	BC	BC
M2	BC[§]	BC	2[**]	BC	0	BC	BC
N	BC	BC	BC	BC	BC	1	BC
O	BC	BC	BC	BC	BC	BC	1
P	0	BC	BC	BC	BC	BC	1

[§] The sheared base-case velocity profile is inappropriate, as fair comparison with the University of Edinburgh model is prevented. This issue is being addressed through the inclusion of an additional case with a uniform velocity profile.

[**] The width of the channel is set to achieve a blockage equivalent to that of the University of Edinburgh model.

|	Shear S	Nacelle height H	Width W	Yaw Y	Tower T	Length L	Duct D
Cases	0, 1, 2	0, 1, 2	0, 1, 2	0, 1, 2	0, 1	0, 1	0, 1
Baseline Case (BC)	2	1	1	0	1	0	0
Q	1	BC	BC	BC	BC	BC	1
R	BC	0	BC	BC	BC	BC	1
S	BC	2	BC	BC	BC	BC	1
T	BC	BC	0	BC	BC	BC	1
U	BC	BC	BC	1	BC	BC	1
V	BC	BC	BC	2	BC	BC	1

7.1 Case A - Base Case - High Shear
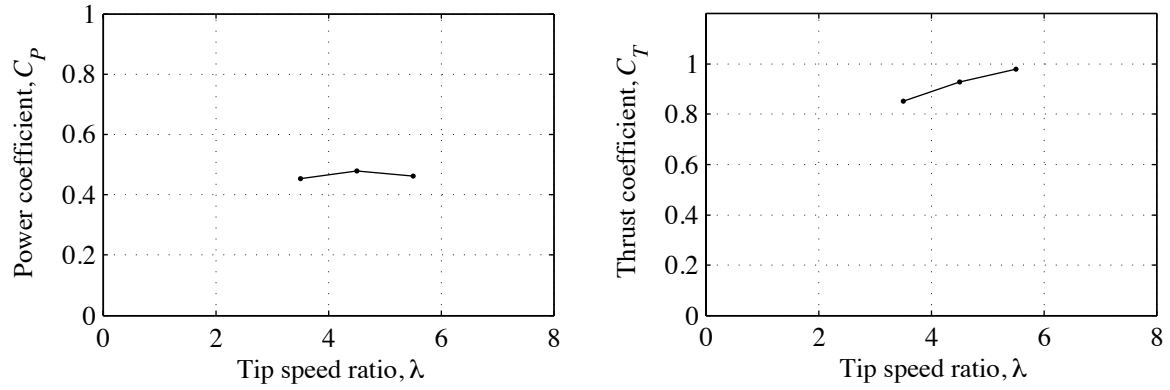
Figure 24: Power and thrust coefficients.
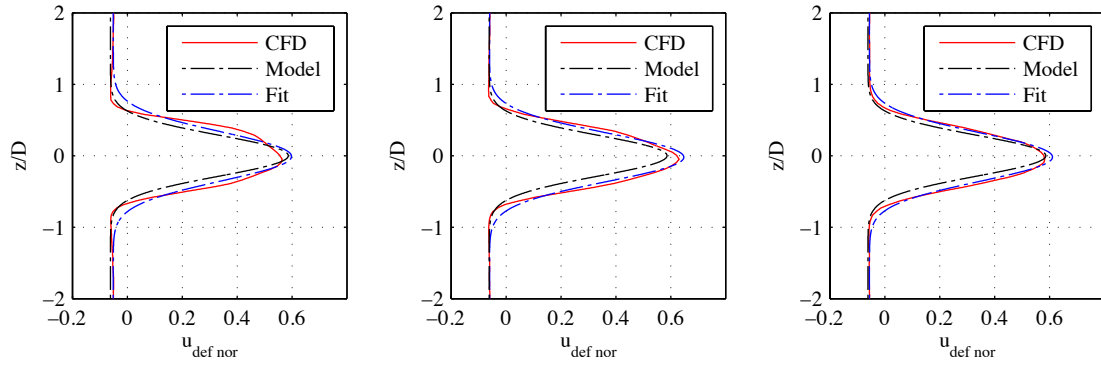
Figure 25: Parametric model of wake velocity deficit (λ = 3.5; 1D, 2D, 5D).
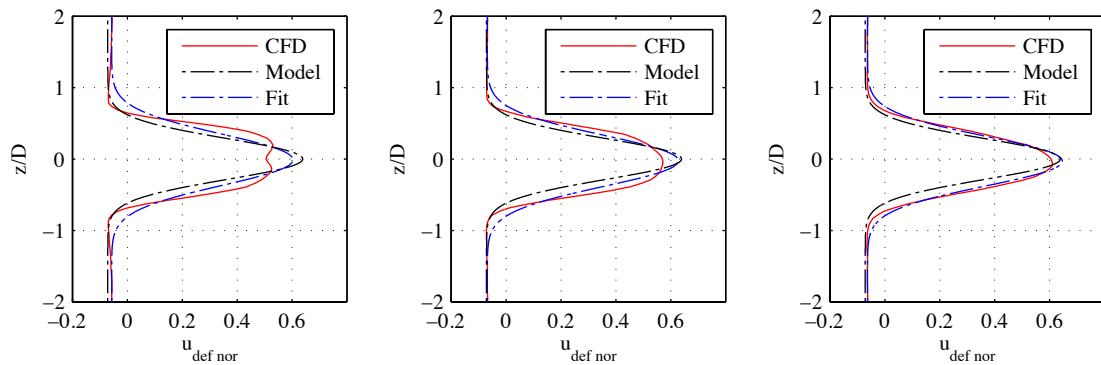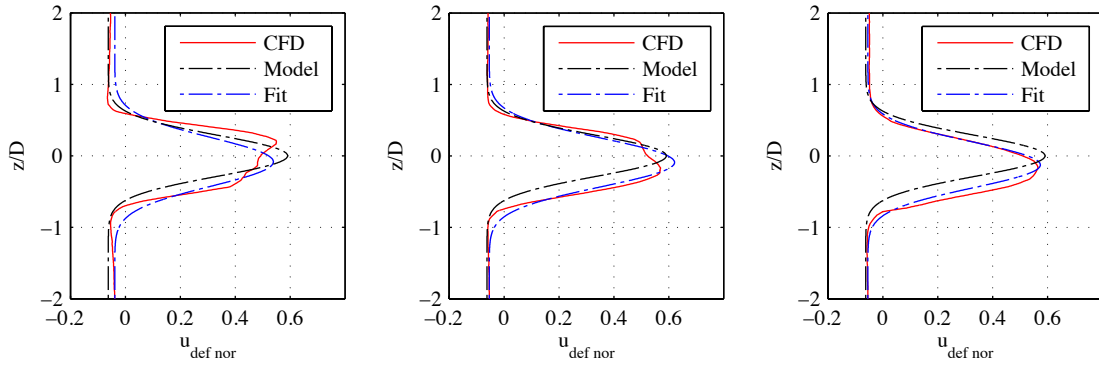

Figure 26: Parametric model of wake velocity deficit (λ = 4.5; 1D, 2D, 5D).
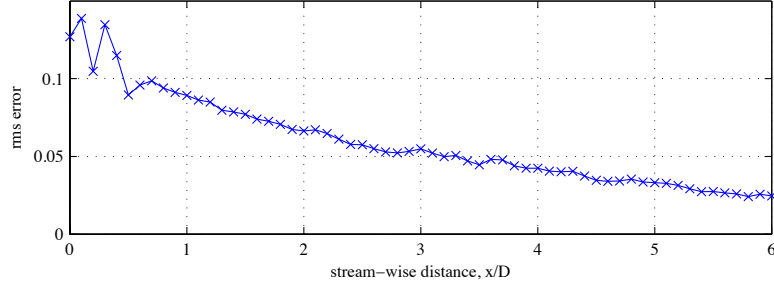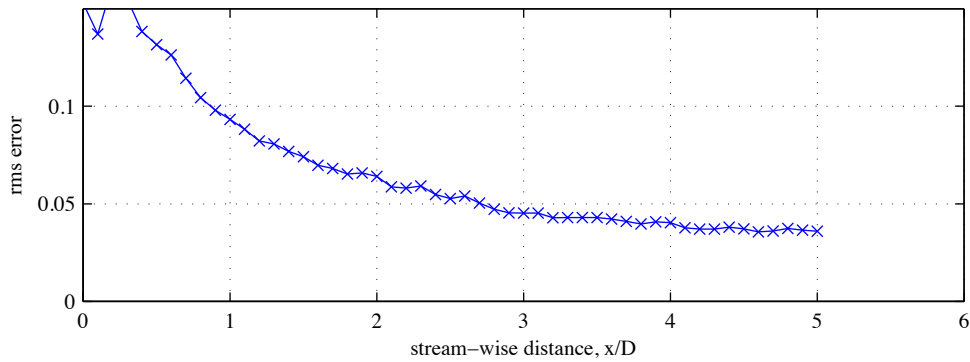
Figure 27: Root mean square error of least-squares fit to simulation data, showing improvement of agreement with downstream distance ($\lambda = 4.5$).
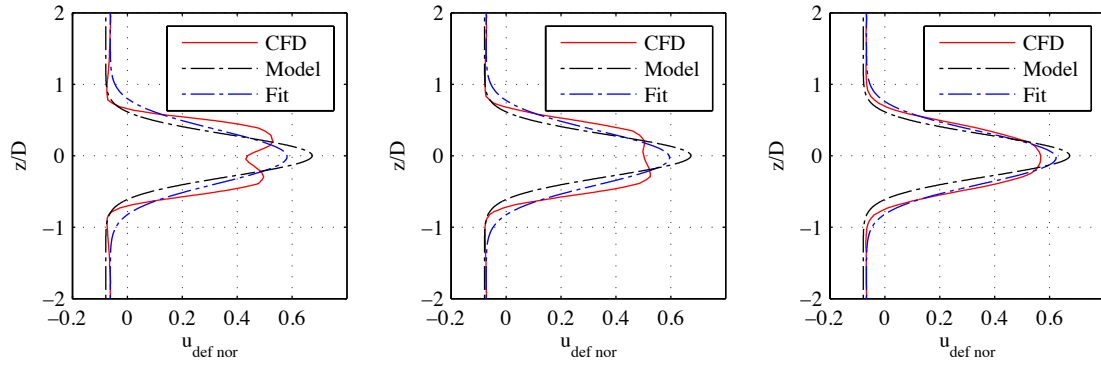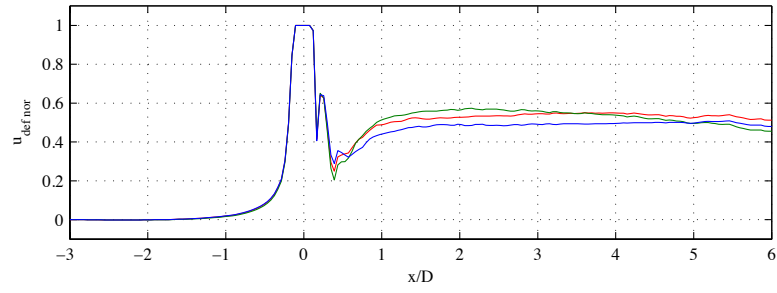

Figure 28: Parametric model of wake velocity deficit ($\lambda = 5.5$; $1D$, wD, $5D$).
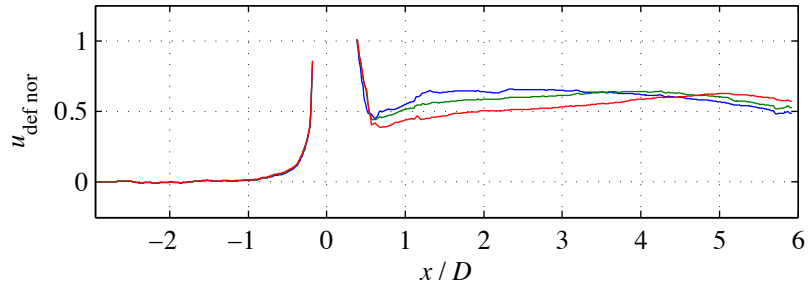
Figure 29: Centreline normalised velocity deficit profiles for $\lambda = 3.5$ (blue), $\lambda = 4.5$ (green), and $\lambda = 5.5$ (red).
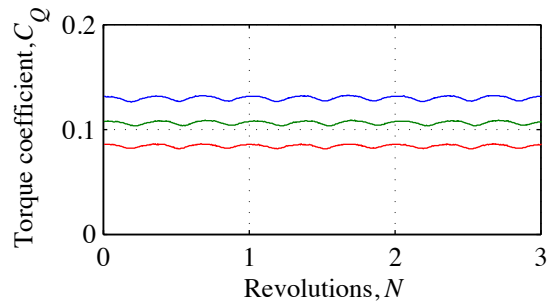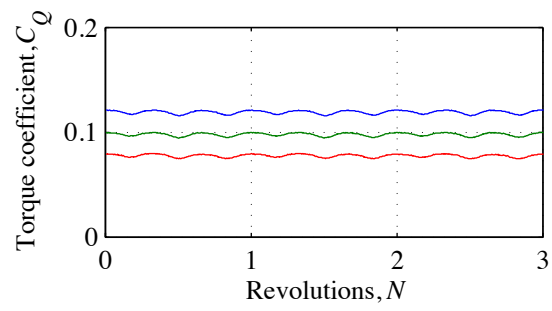

Figure 30: Rotor torque traces for the final revolutions of simulation for $\lambda = 3.5$ (blue), $\lambda = 4.5$ (green), and $\lambda = 5.5$ (red).

7.2 Case B - Uniform Flow
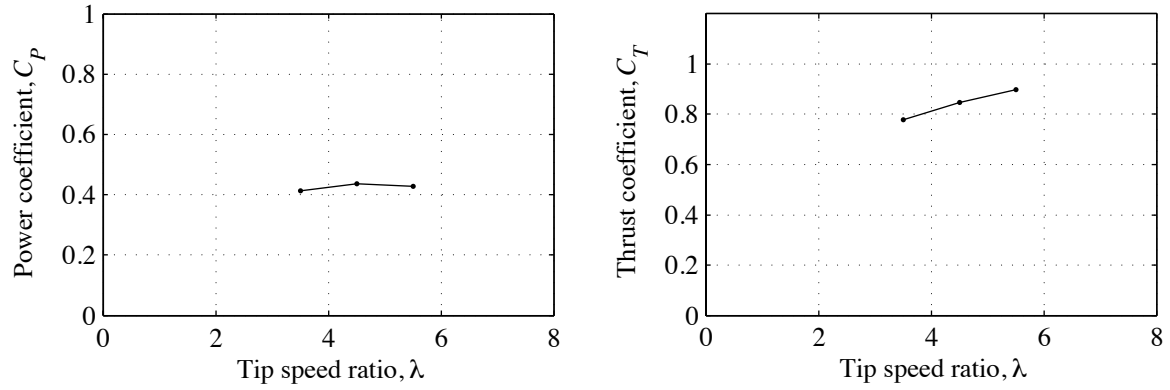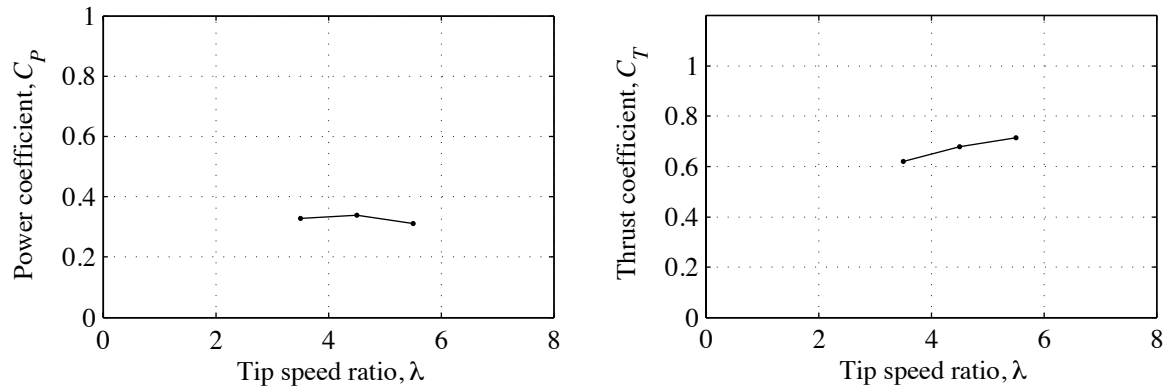

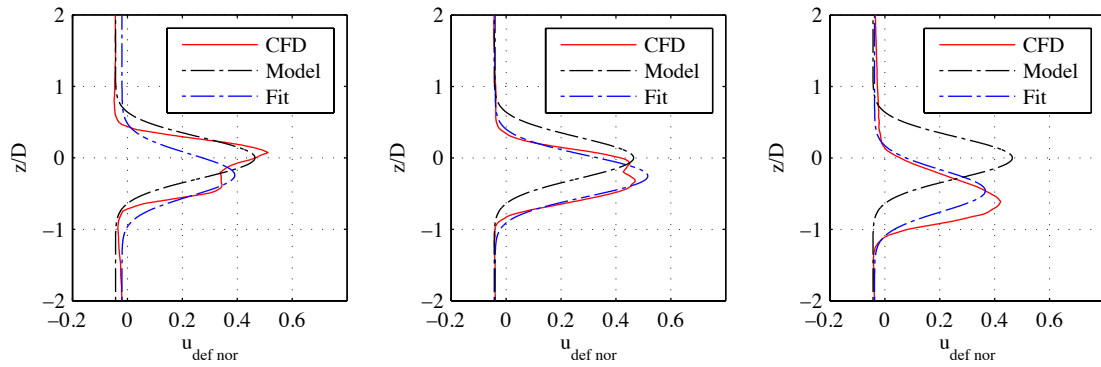Figure 31: Power and thrust coefficients.
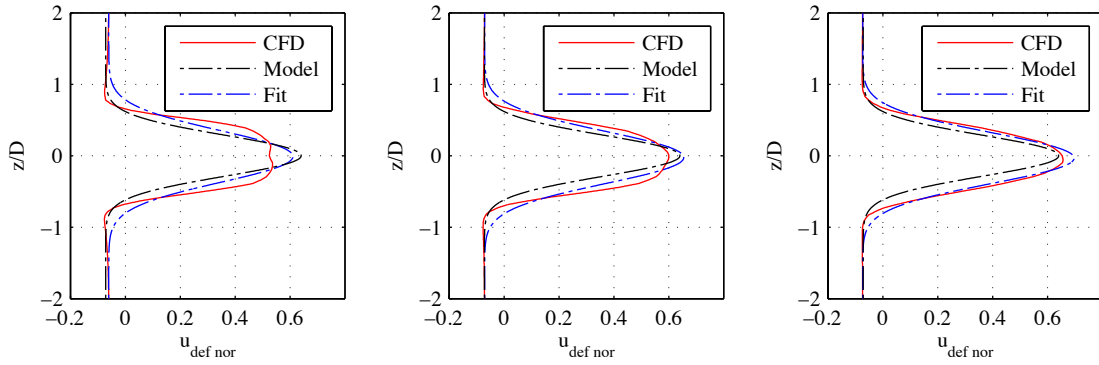
Figure 32: Parametric model of wake velocity deficit ($\lambda = 4.5$; $1D$, $2D$, $5D$).
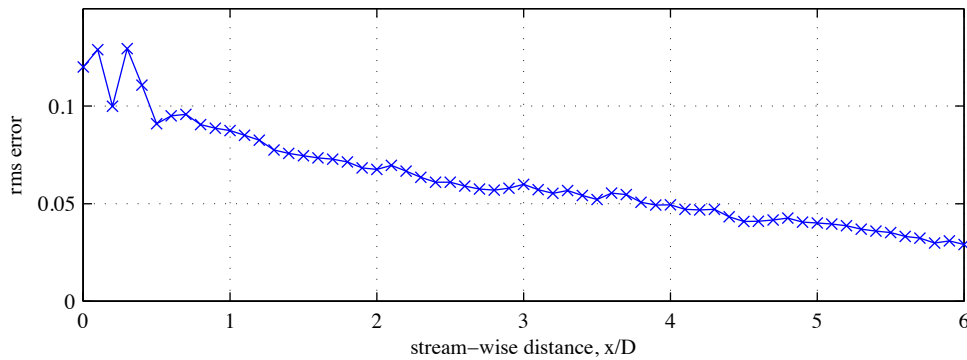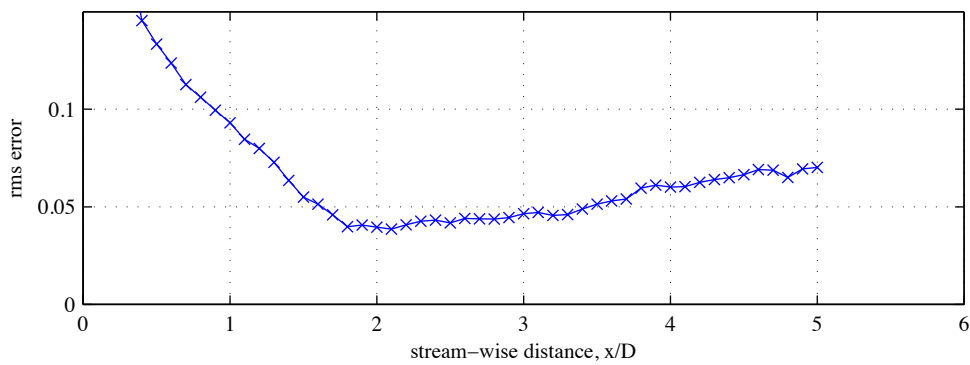

Figure 33: Root mean square error of least-squares fit to simulation data, showing improvement of agreement with downstream distance ($\lambda = 4.5$).
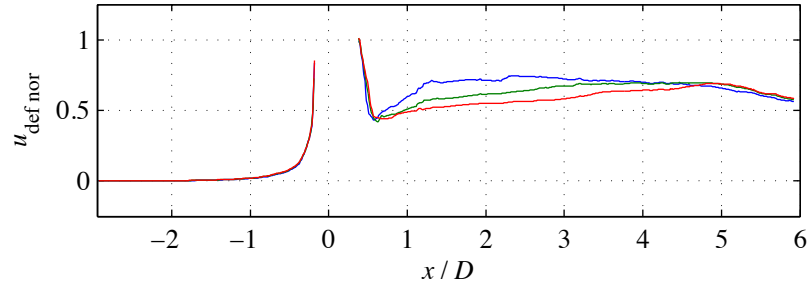
Figure 34: Centreline normalised velocity deficit profiles for λ = 3.5 (blue), λ = 4.5 (green), and λ = 5.5 (red).
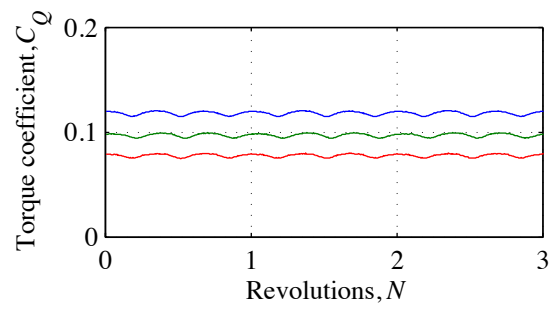
Figure 35: Rotor torque traces for the final revolutions of simulation for λ = 3.5 (blue), λ = 4.5 (green), and λ = 5.5 (red).

7.3 Case C - Low Shear
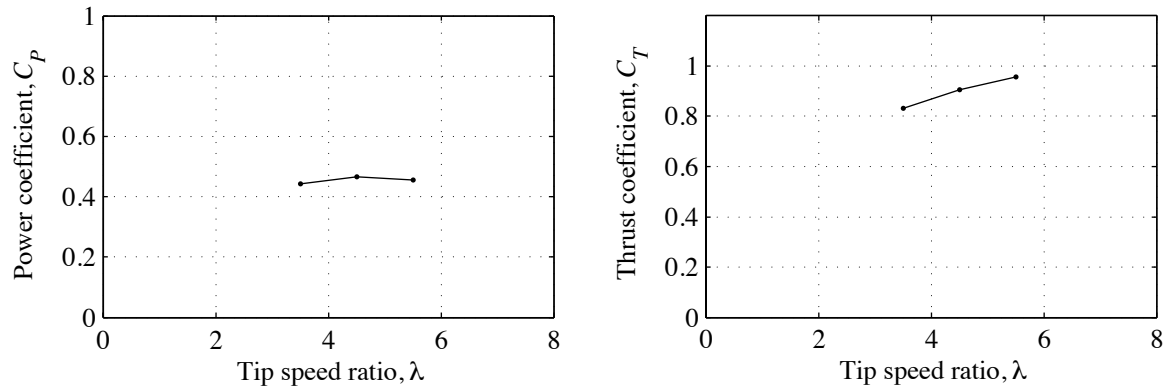
Figure 36: Power and thrust coefficients.
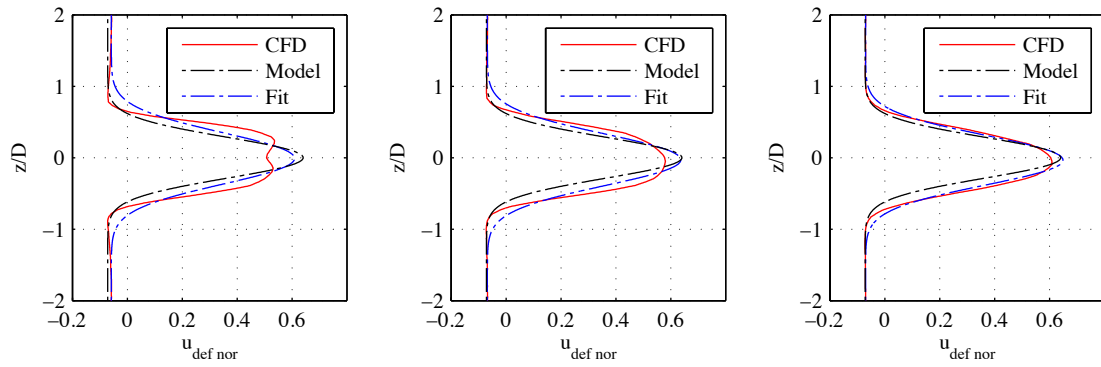
Figure 37: Parametric model of wake velocity deficit (λ = 4.5; 1*D*, 2*D*, 5*D*).
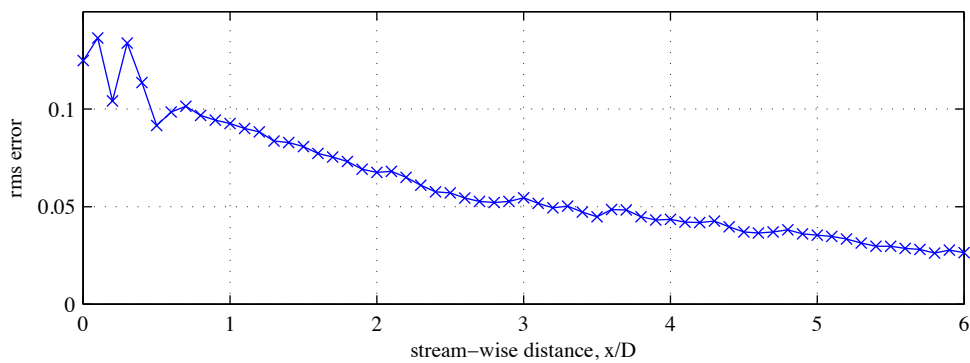
Figure 38: Root mean square error of least-squares fit to simulation data, showing improvement of agreement with downstream distance (λ = 4.5).
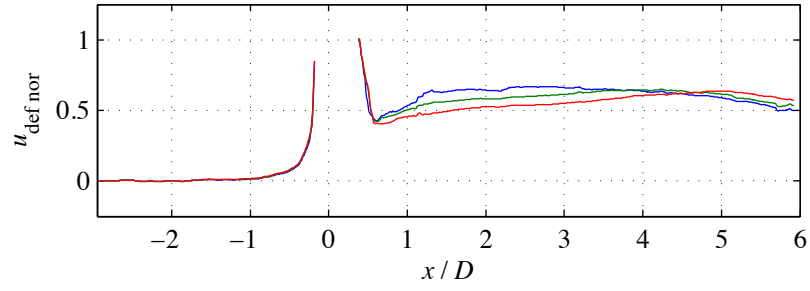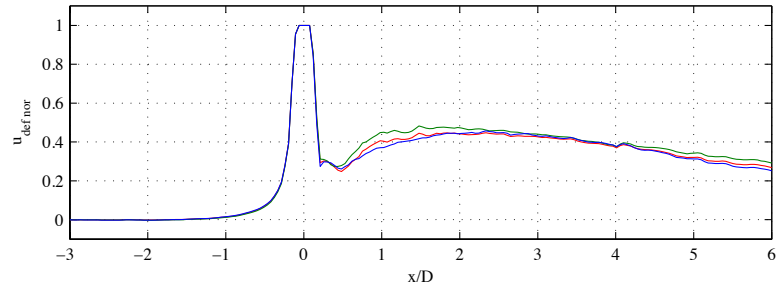
Figure 39: Centreline normalised velocity deficit profiles for λ = 3.5 (blue), λ = 4.5 (green), and λ = 5.5 (red).
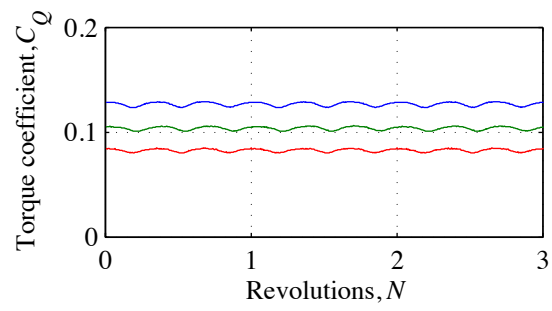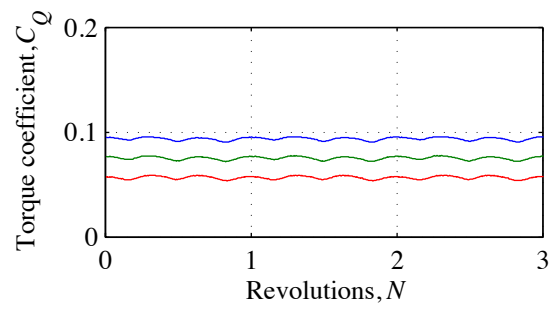

Figure 40: Rotor torque traces for the final revolutions of simulation for λ = 3.5 (blue), λ = 4.5 (green), and λ = 5.5 (red).

7.4 Case D - High Shear - Low Elevation
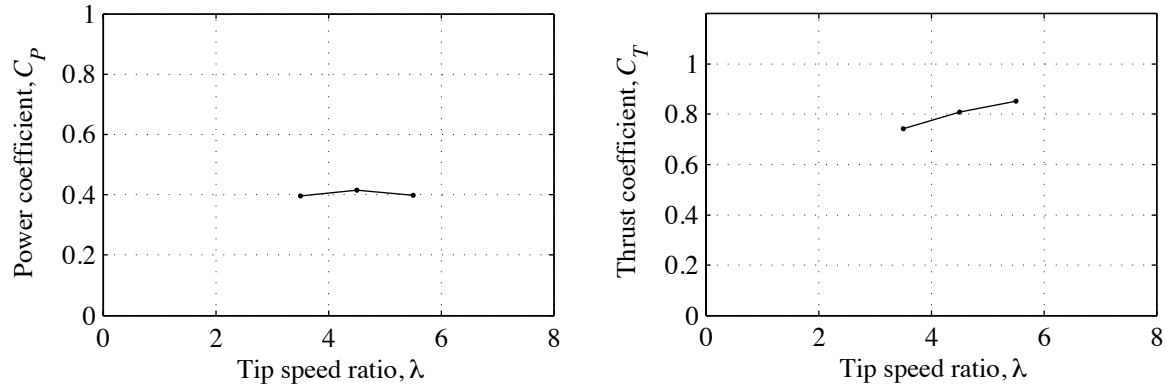
Figure 41: Power and thrust coefficients.
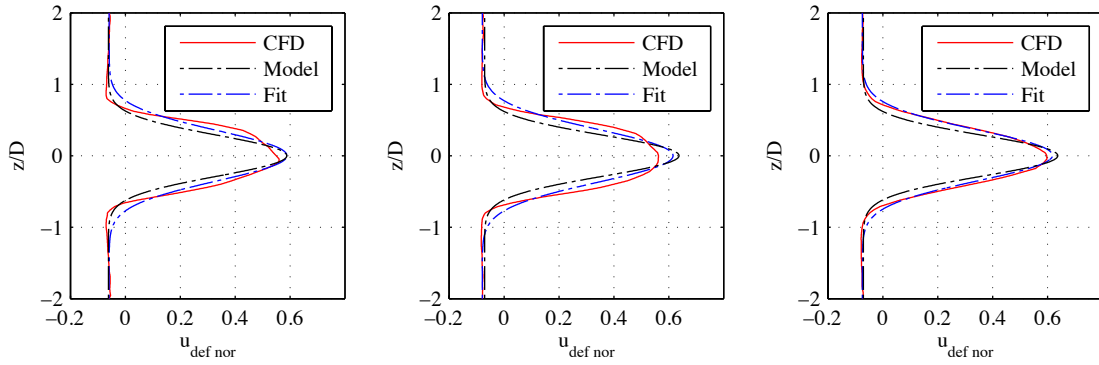
Figure 42: Parametric model of wake velocity deficit ($\lambda = 4.5$; $1D$, $2D$, $5D$).
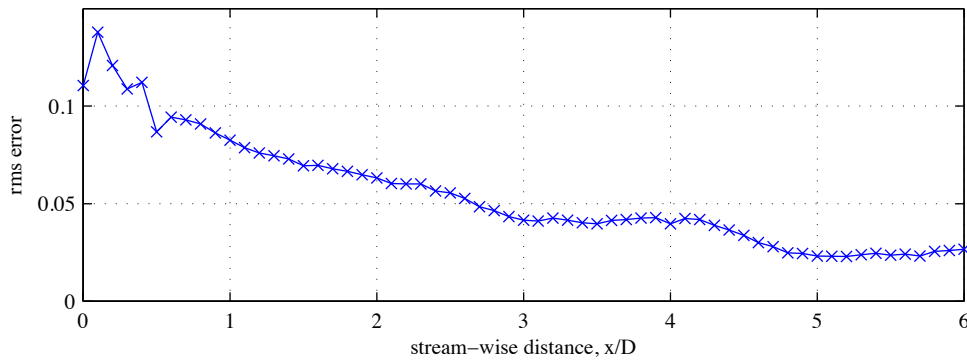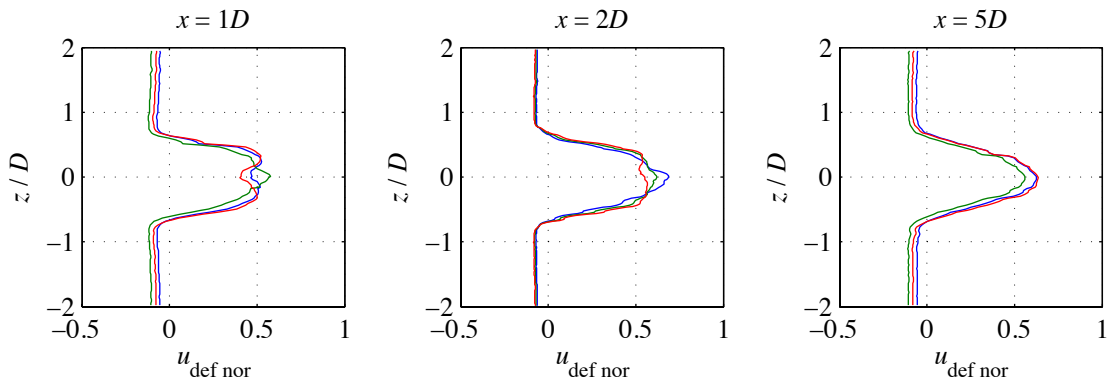

Figure 43: Root mean square error of least-squares fit to simulation data, showing improvement of agreement with downstream distance ($\lambda = 4.5$).
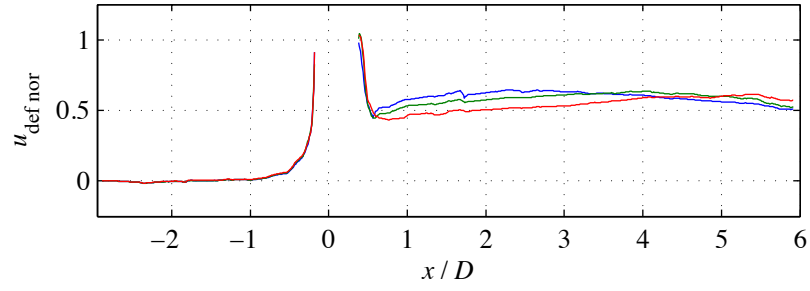
Figure 44: Centreline normalised velocity deficit profiles for λ = 3.5 (blue), λ = 4.5 (green), and λ = 5.5 (red).
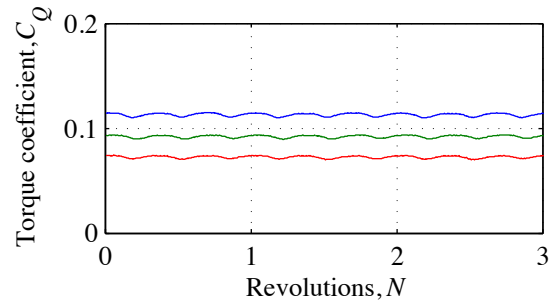
Figure 45: Rotor torque traces for the final revolutions of simulation for λ = 3.5 (blue), λ = 4.5 (green), and λ = 5.5 (red).

7.5 Case E - Uniform Flow - Low Elevation
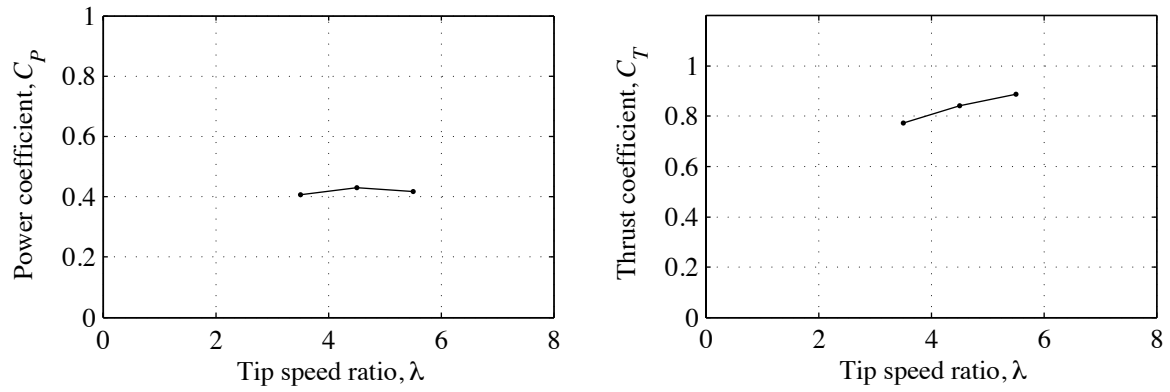
Figure 46: Power and thrust coefficients.
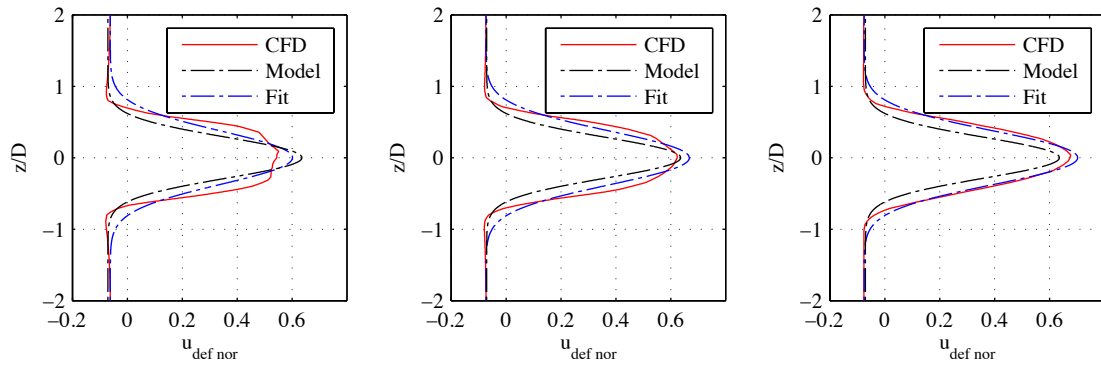
Figure 47: Parametric model of wake velocity deficit ($\lambda = 4.5$; 1D, 2D, 5D).
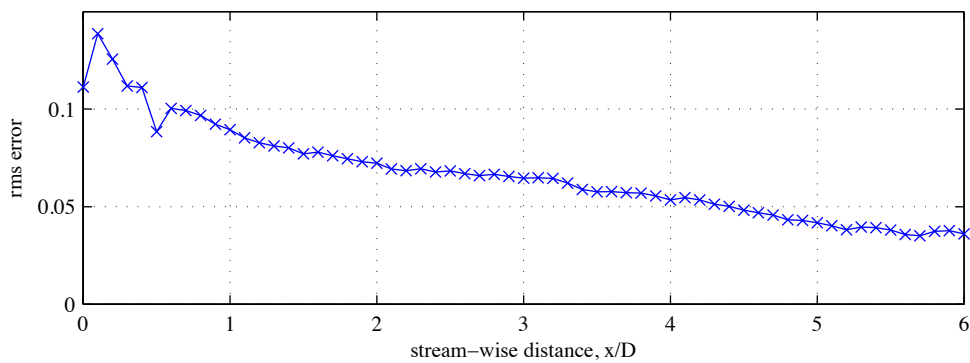
Figure 48: Root mean square error of least-squares fit to simulation data, showing improvement of agreement with downstream distance ($\lambda = 4.5$).
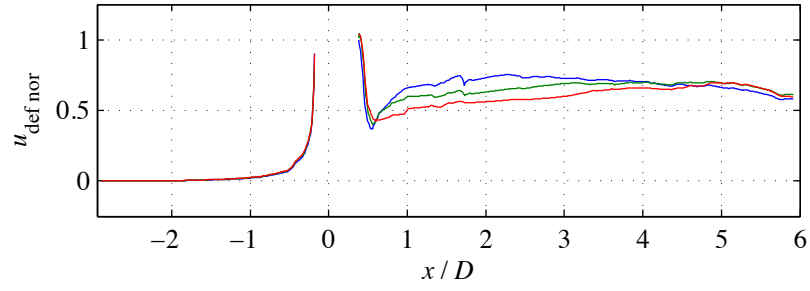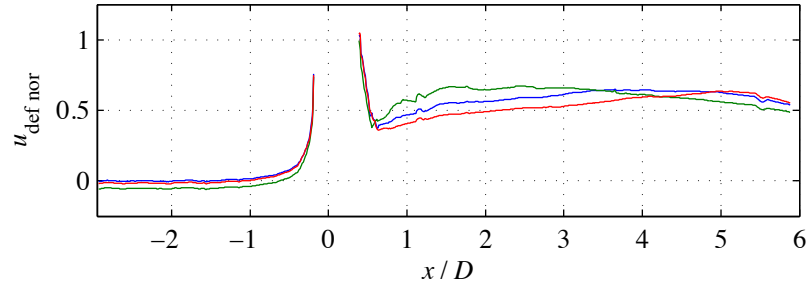
Figure 49: Centreline normalised velocity deficit profiles for λ = 3.5 (blue), λ = 4.5 (green), and λ = 5.5 (red).
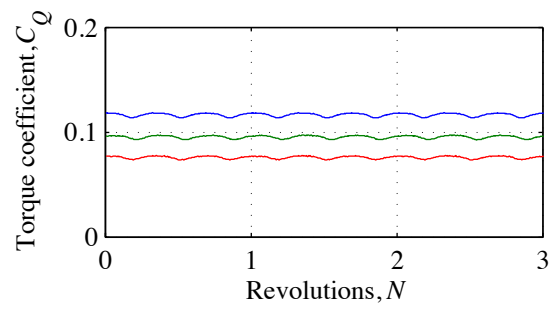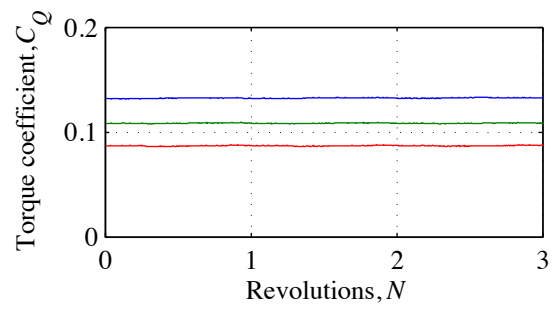

Figure 50: Rotor torque traces for the final revolutions of simulation for λ = 3.5 (blue), λ = 4.5 (green), and λ = 5.5 (red).

7.6 Case F - Low Shear - Low Elevation
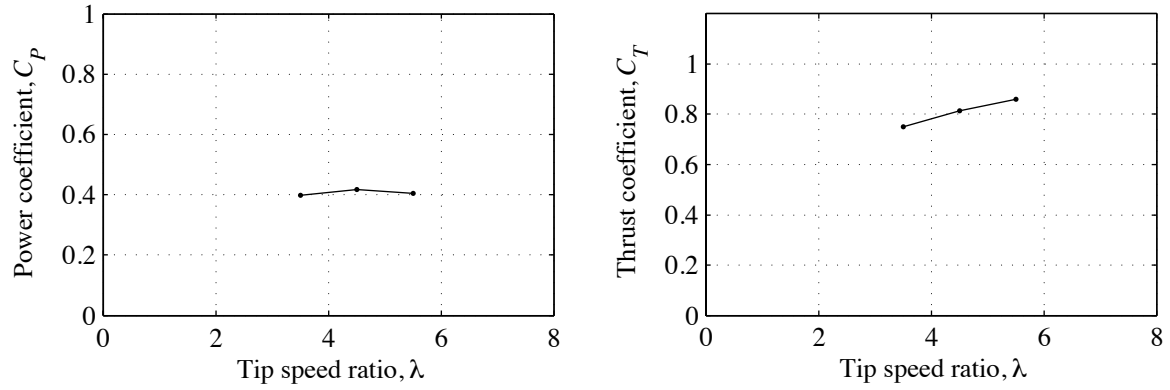
Figure 51: Power and thrust coefficients.
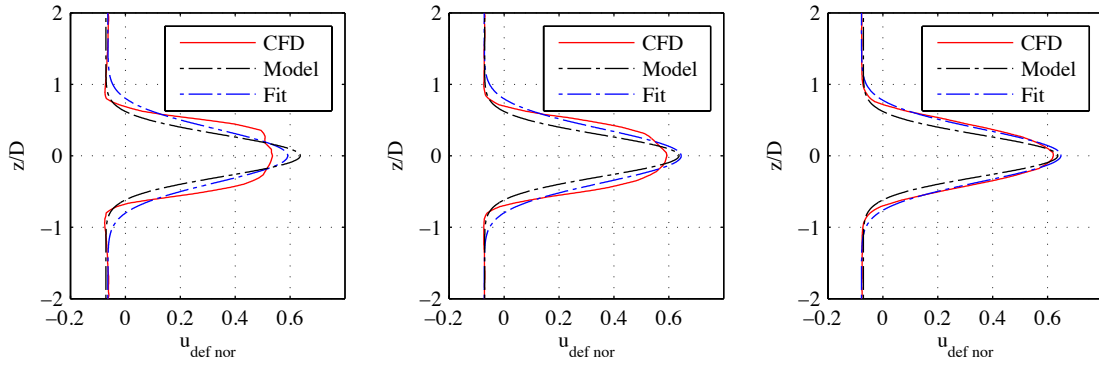
Figure 52: Parametric model of wake velocity deficit ($\lambda = 4.5$; $1D$, $2D$, $5D$).
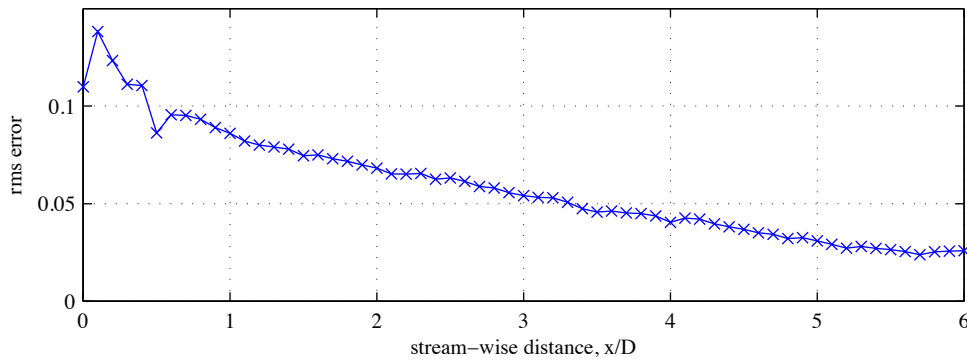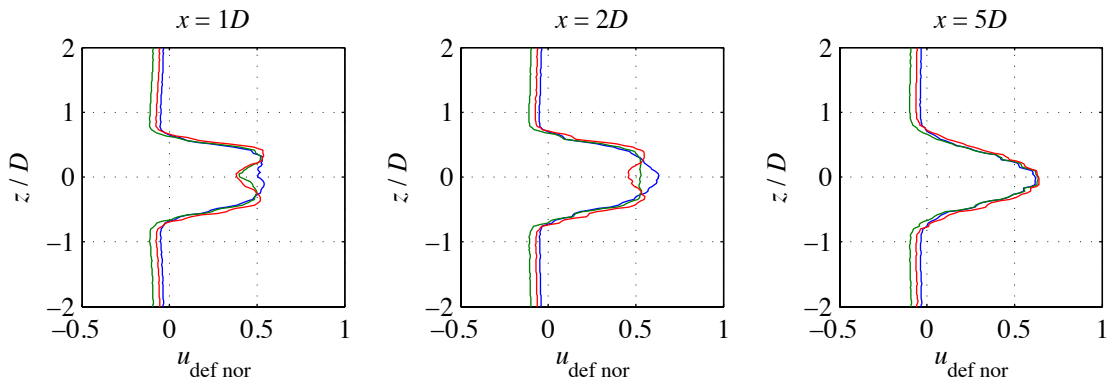

Figure 53: Root mean square error of least-squares fit to simulation data, showing improvement of agreement with downstream distance ($\lambda = 4.5$).
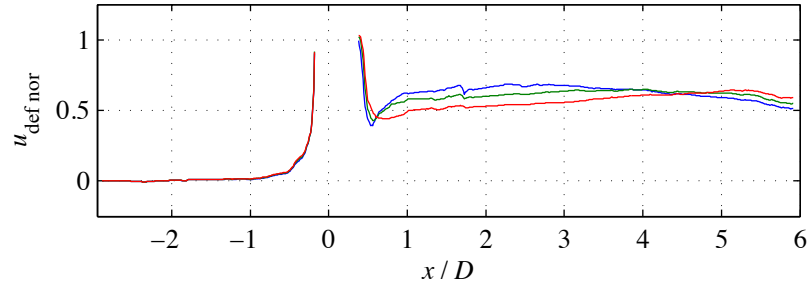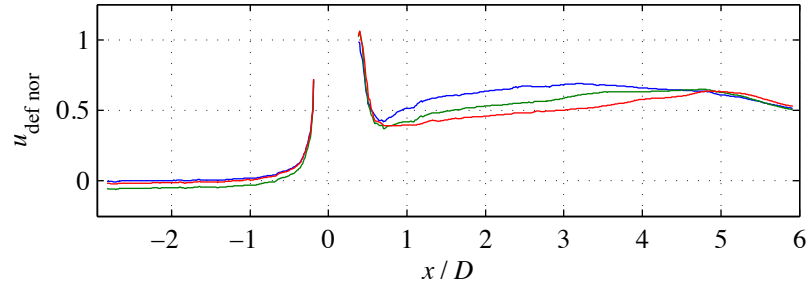
Figure 54: Centreline normalised velocity deficit profiles for $\lambda = 3.5$ (blue), $\lambda = 4.5$ (green), and $\lambda = 5.5$ (red).
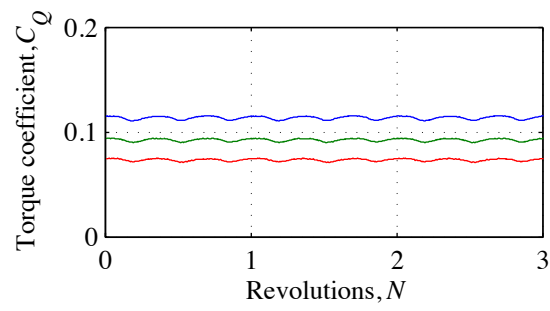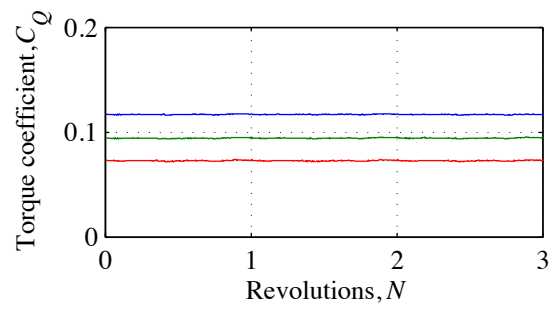

Figure 55: Rotor torque traces for the final revolutions of simulation for $\lambda = 3.5$ (blue), $\lambda = 4.5$ (green), and $\lambda = 5.5$ (red).

7.7 Case G - High Shear - High Elevation
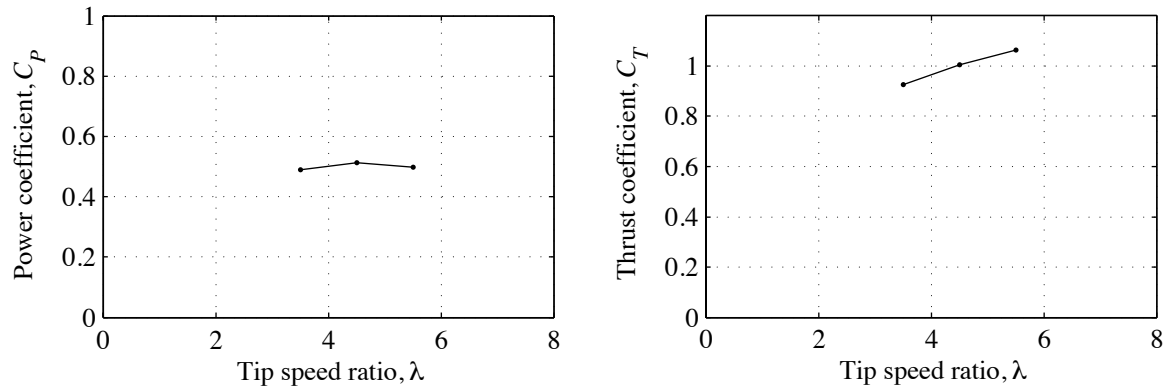
Figure 56: Power and thrust coefficients.
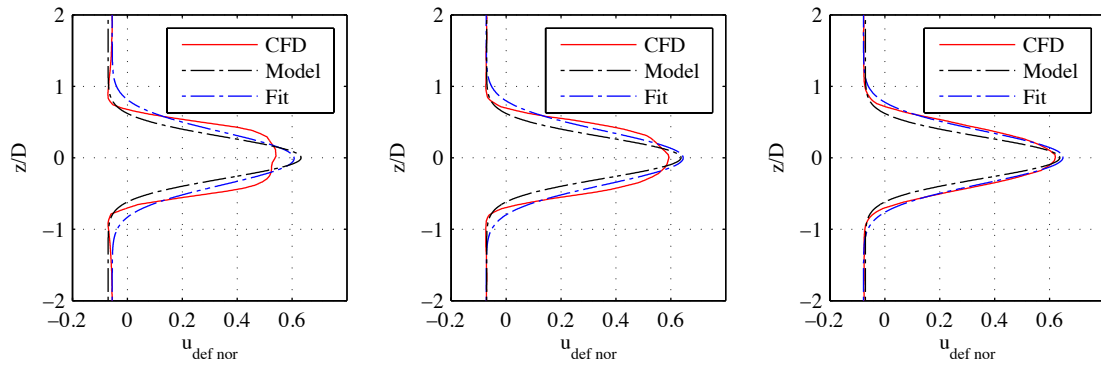
Figure 57: Parametric model of wake velocity deficit (λ = 4.5; 1D, 2D, 5D).
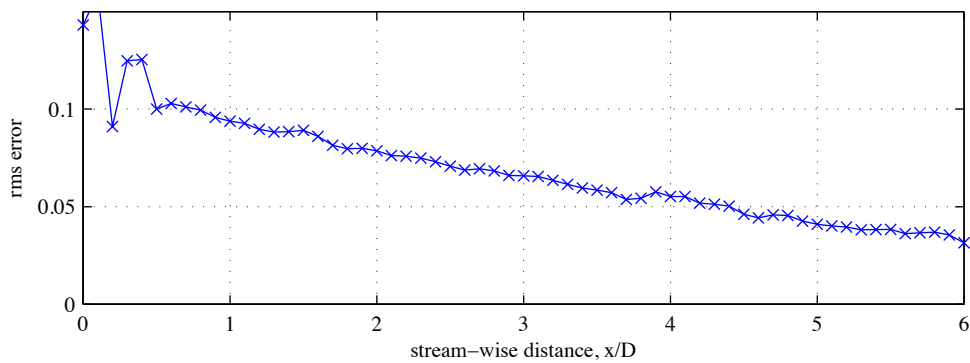
Figure 58: Root mean square error of least-squares fit to simulation data, showing improvement of agreement with downstream distance (λ = 4.5).
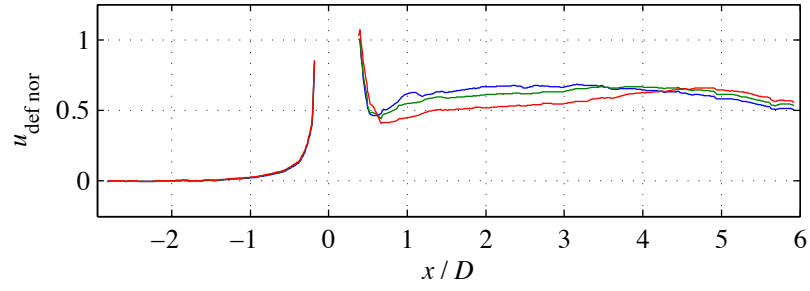
Figure 59: Centreline normalised velocity deficit profiles for λ = 3.5 (blue), λ = 4.5 (green), and λ = 5.5 (red).
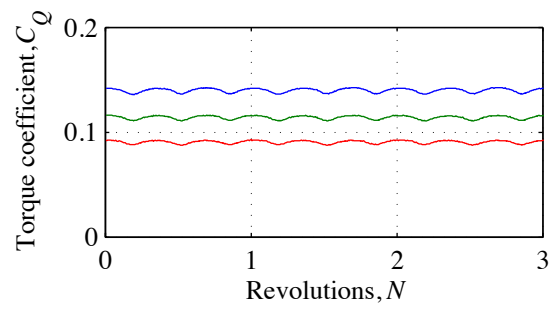
Figure 60: Rotor torque traces for the final revolutions of simulation for λ = 3.5 (blue), λ = 4.5 (green), and λ = 5.5 (red).

7.8 Case H - Uniform Flow - High Elevation
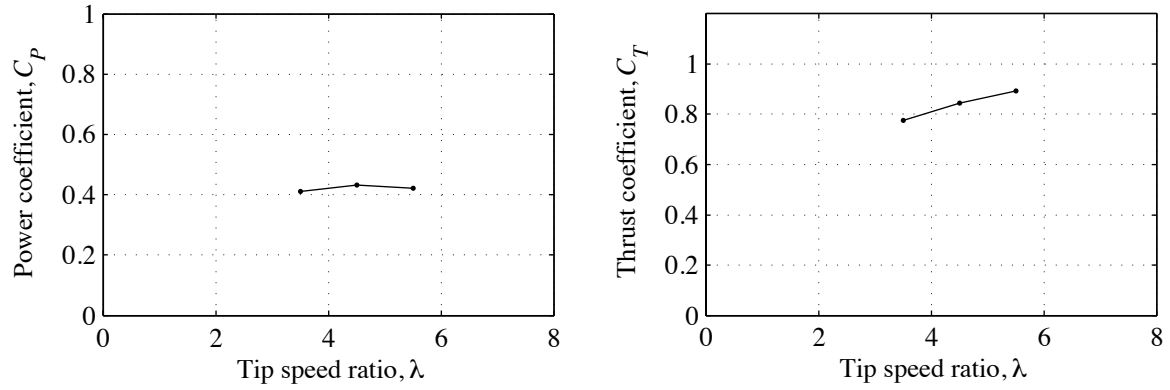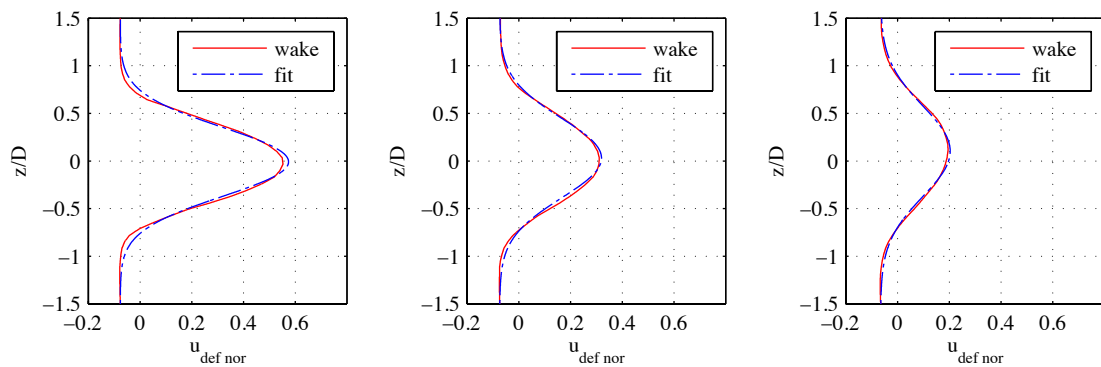

Figure 61: Power and thrust coefficients.
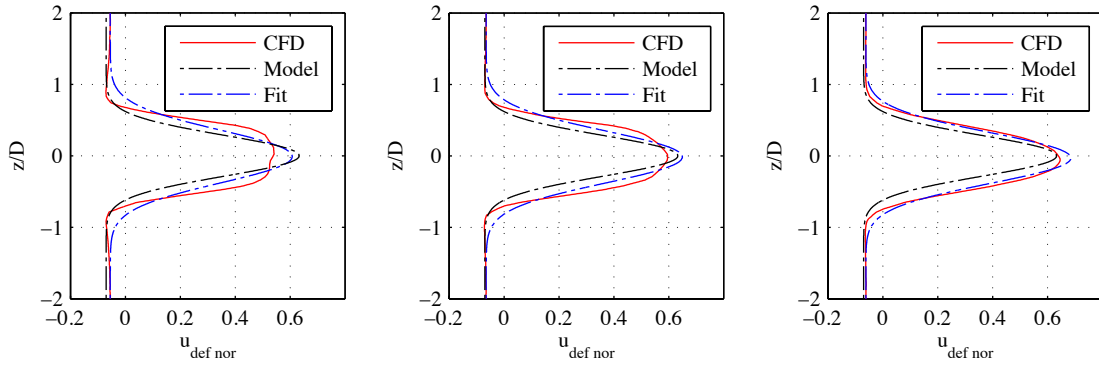
Figure 62: Parametric model of wake velocity deficit ($\lambda = 4.5$; $1D$, $2D$, $5D$).
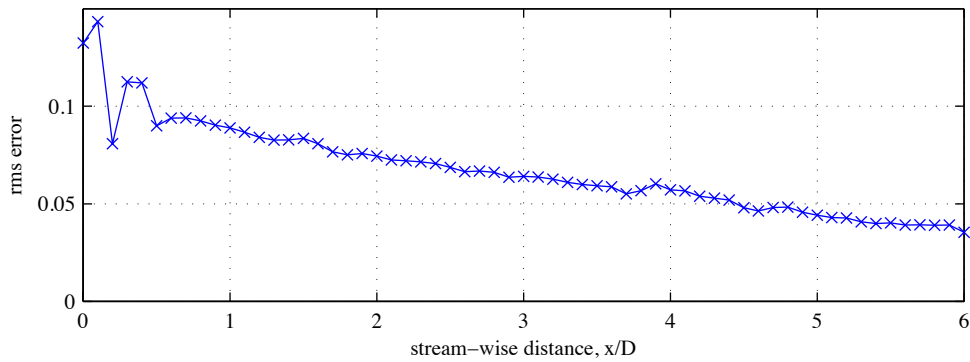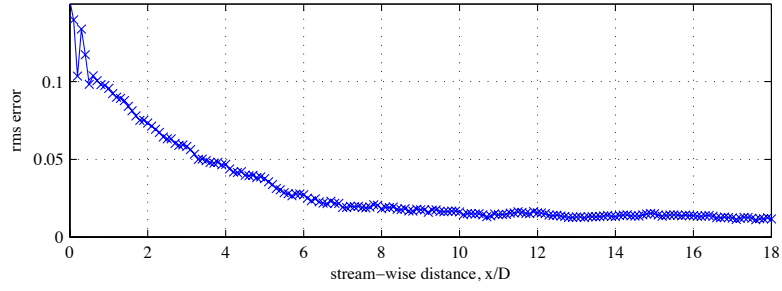

Figure 63: Root mean square error of least-squares fit to simulation data, showing improvement of agreement with downstream distance ($\lambda = 4.5$).
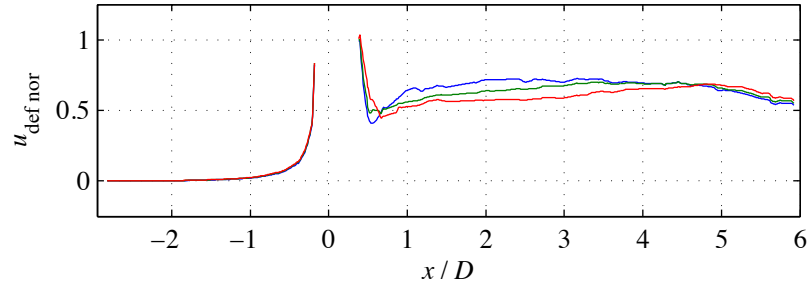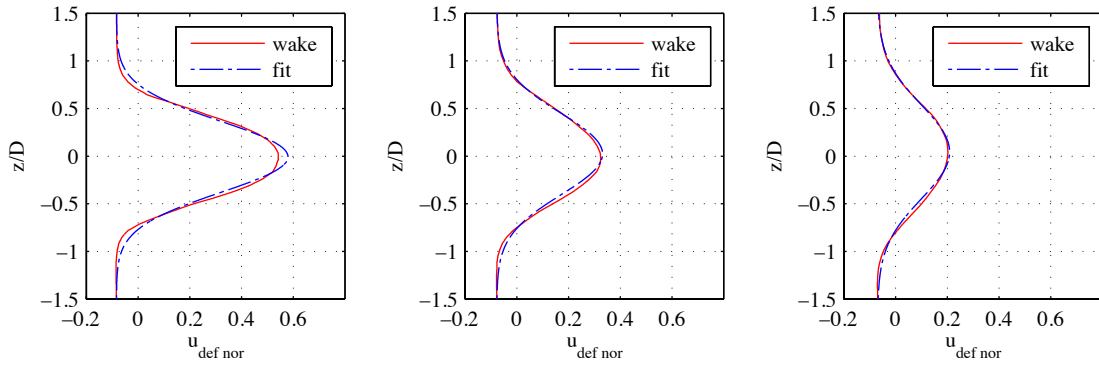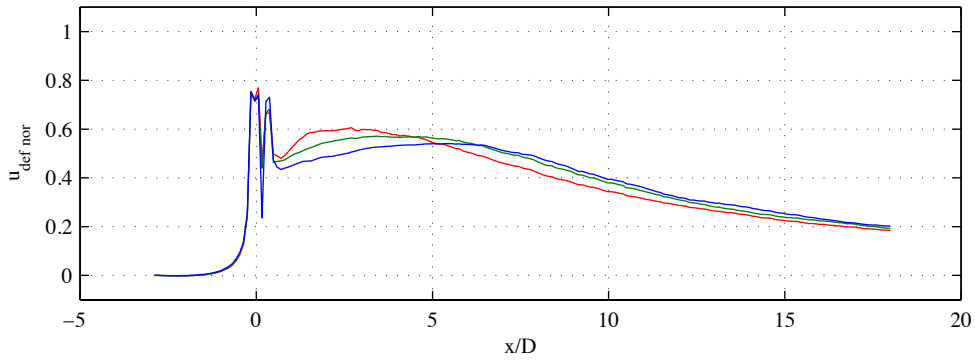
Figure 64: Centreline normalised velocity deficit profiles for λ = 3.5 (blue), λ = 4.5 (green), and λ = 5.5 (red).
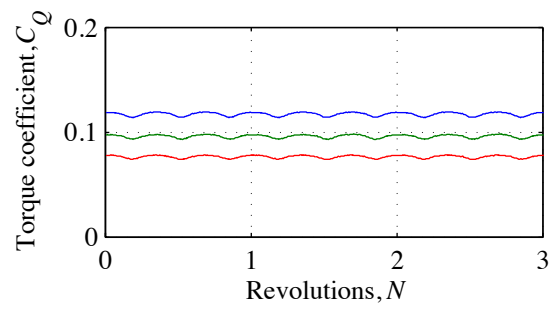
Figure 65: Rotor torque traces for the final revolutions of simulation for λ = 3.5 (blue), λ = 4.5 (green), and λ = 5.5 (red).

7.9 Case I - Low Shear - High Elevation
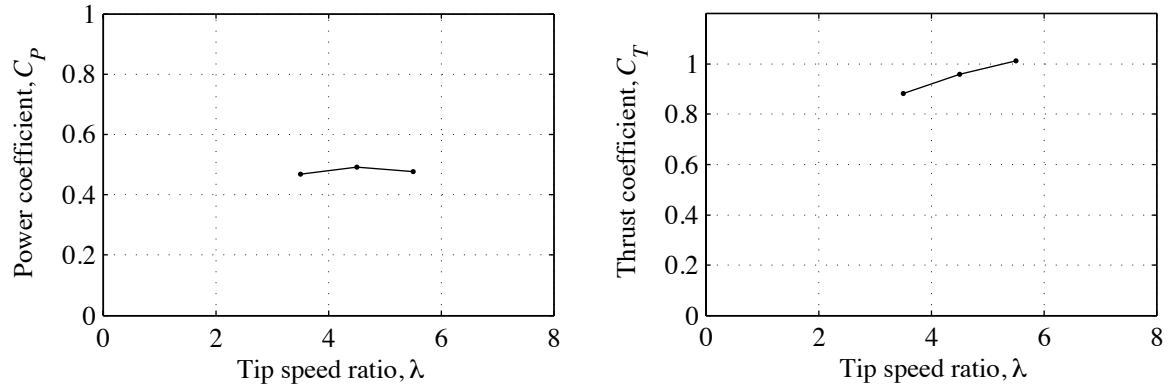
Figure 66: Power and thrust coefficients.
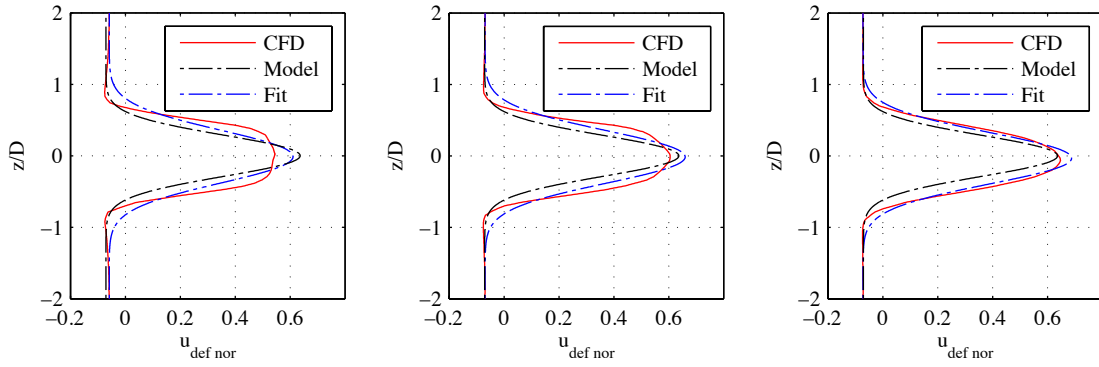
Figure 67: Parametric model of wake velocity deficit ($\lambda = 4.5$; 1D, 2D, 5D).
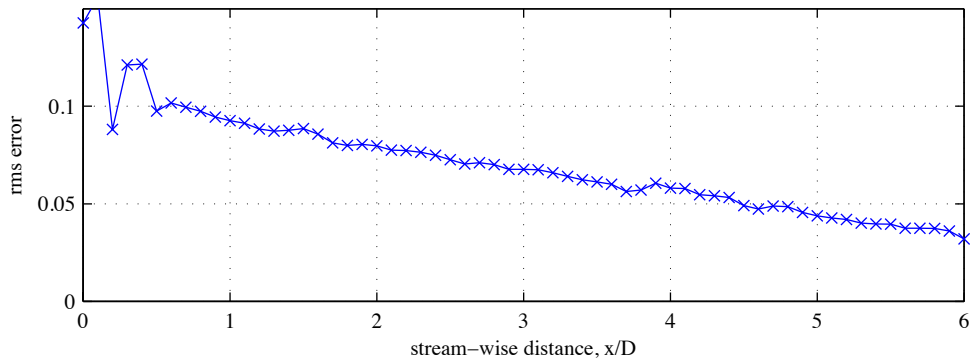
Figure 68: Root mean square error of least-squares fit to simulation data, showing improvement of agreement with downstream distance ($\lambda = 4.5$).
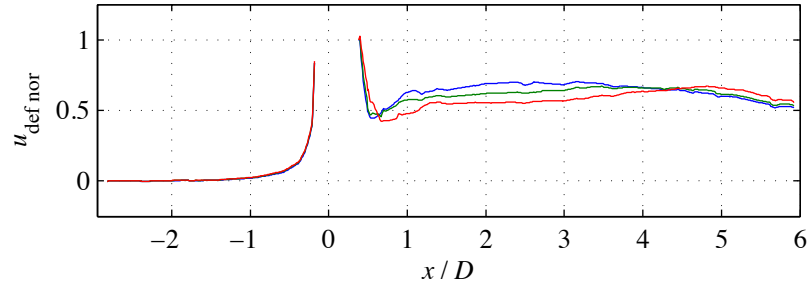
Figure 69: Centreline normalised velocity deficit profiles for λ = 3.5 (blue), λ = 4.5 (green), and λ = 5.5 (red).
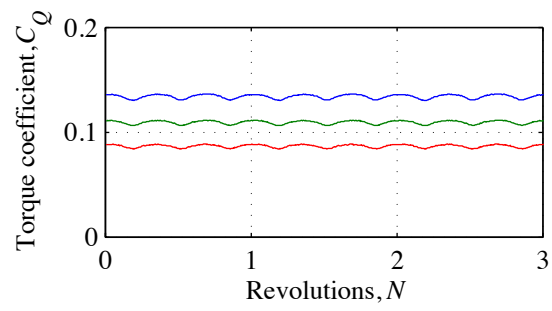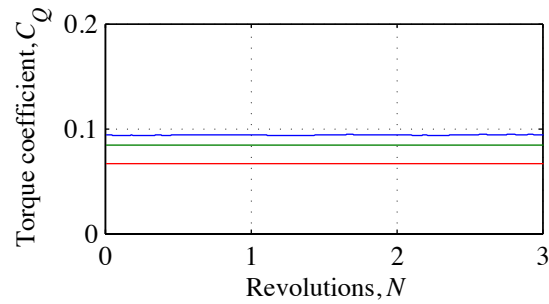

Figure 70: Rotor torque traces for the final revolutions of simulation for λ = 3.5 (blue), λ = 4.5 (green), and λ = 5.5 (red).

7.10 Case J - Narrow Domain
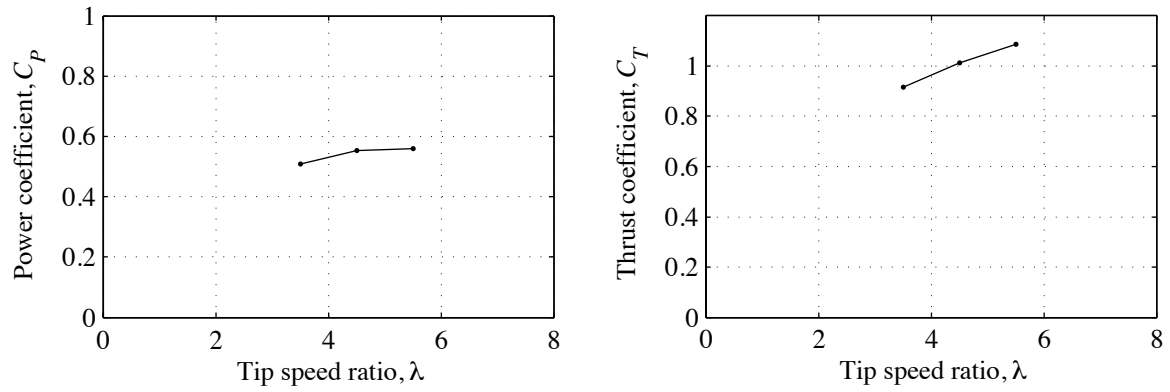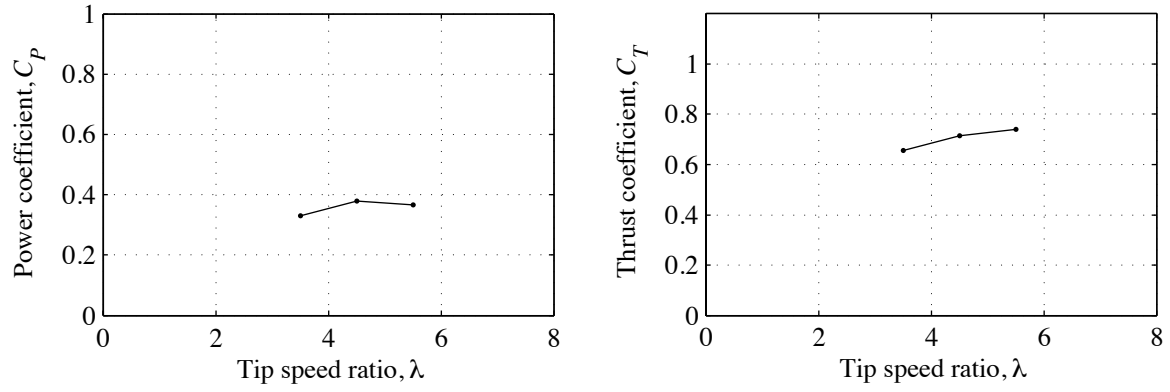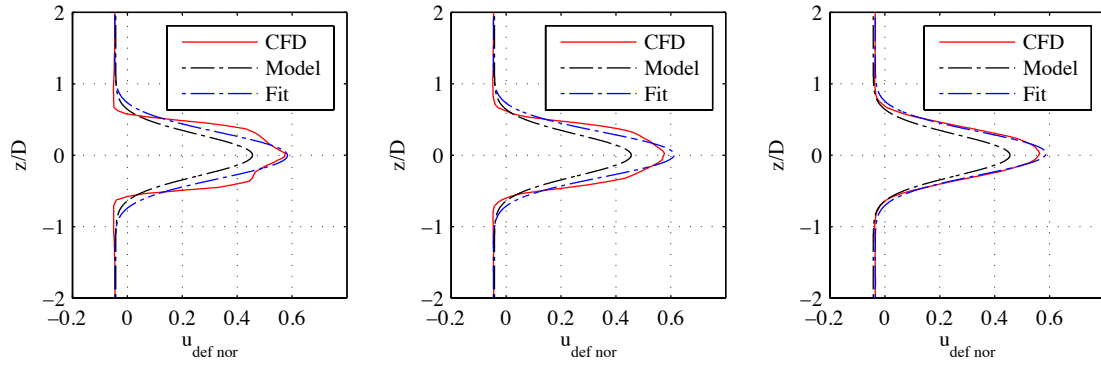

Figure 71: Power and thrust coefficients.
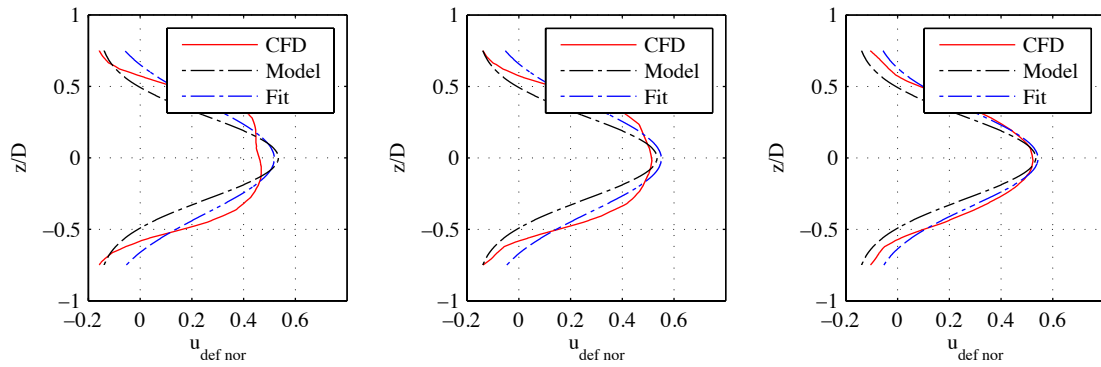
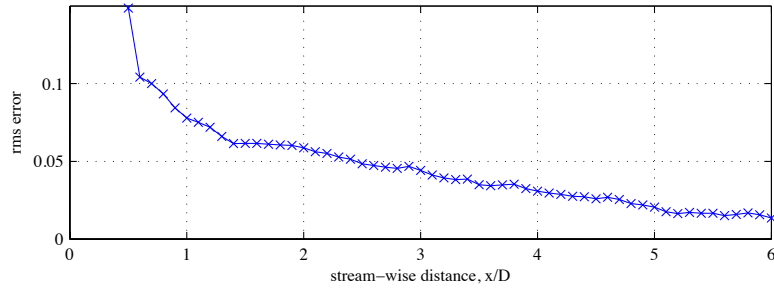Figure 72: Parametric model of wake velocity deficit ($\lambda = 4.5$; 1D, 2D, 5D).
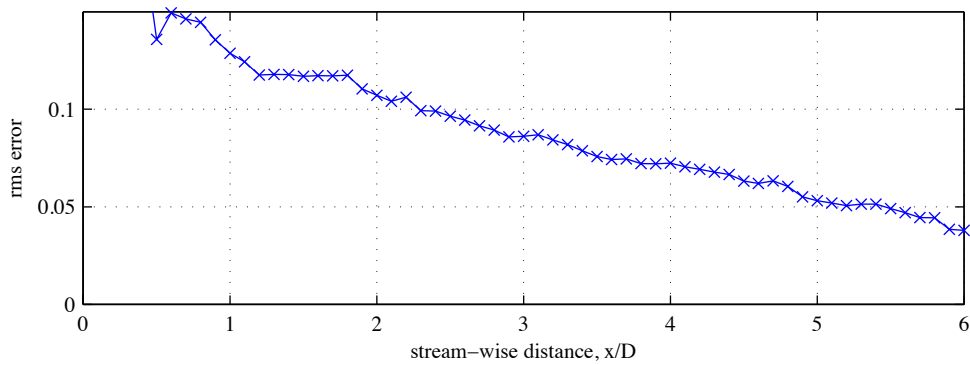
Figure 73: Root mean square error of least-squares fit to simulation data, showing improvement of agreement with downstream distance ($\lambda = 4.5$).
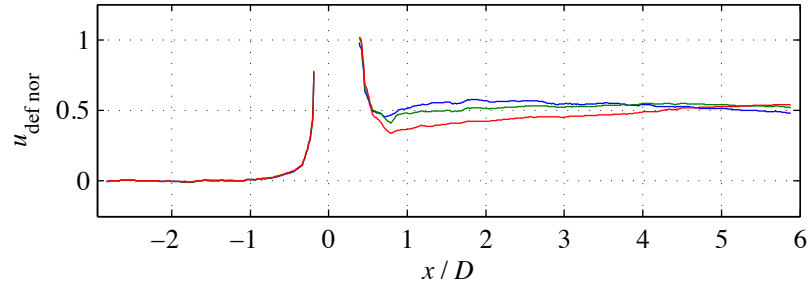
Figure 74: Centreline normalised velocity deficit profiles for $\lambda = 3.5$ (blue), $\lambda = 4.5$ (green), and $\lambda = 5.5$ (red).
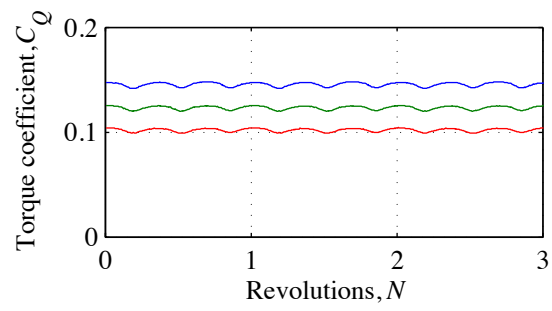
Figure 75: Rotor torque traces for the final revolutions of simulation for $\lambda = 3.5$ (blue), $\lambda = 4.5$ (green), and $\lambda = 5.5$ (red).

7.11 Case K - 15° Yaw
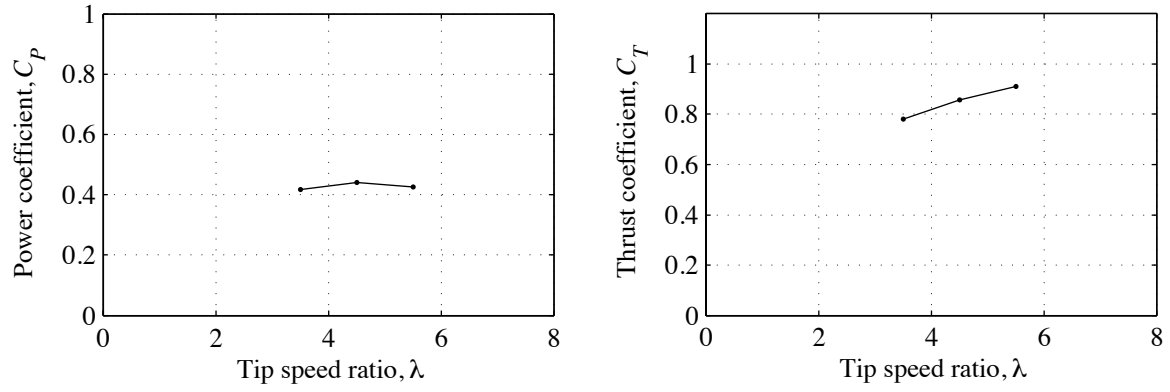
Figure 76: Power and thrust coefficients.

Figure 77: Parametric model of wake velocity deficit ($\lambda = 4.5$; $1D$, $2D$, $5D$).

Figure 78: Root mean square error of least-squares fit to simulation data, showing improvement of agreement with downstream distance ($\lambda = 4.5$).
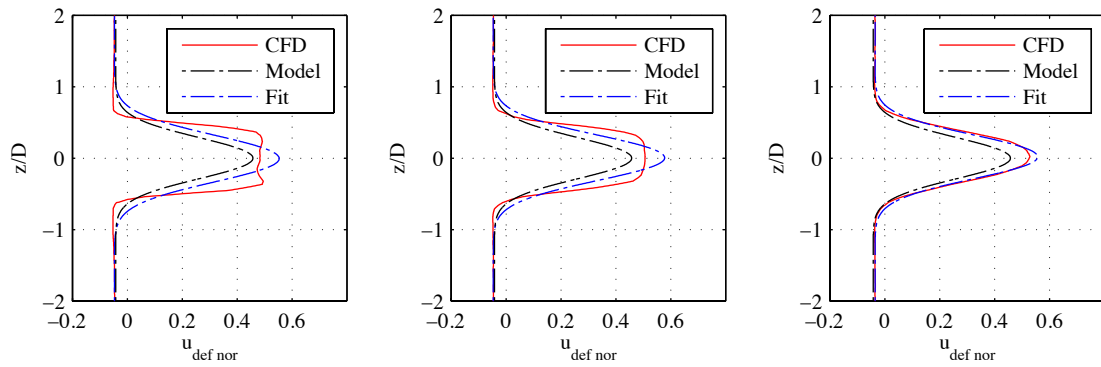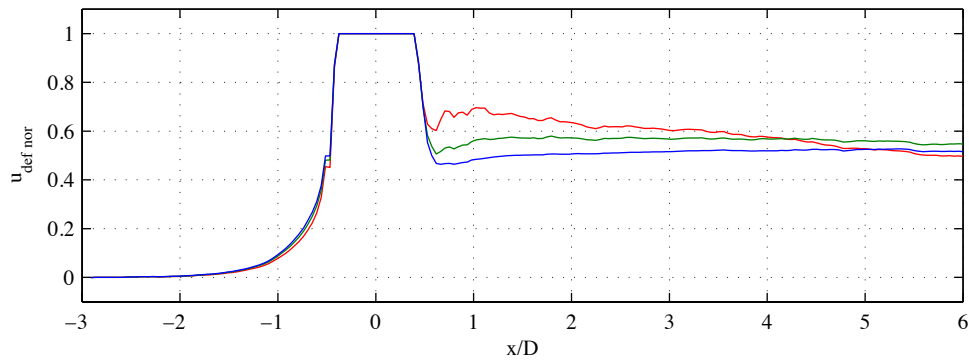
Figure 79: Centreline normalised velocity deficit profiles for $\lambda = 3.5$ (blue), $\lambda = 4.5$ (green), and $\lambda = 5.5$ (red).

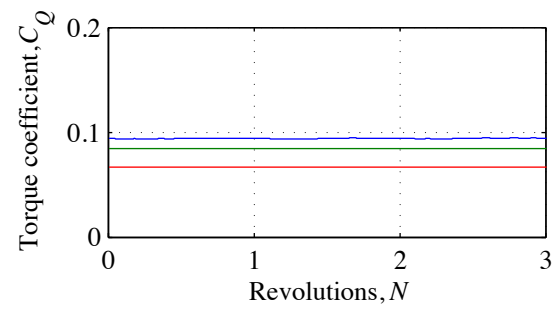
Figure 80: Rotor torque traces for the final revolutions of simulation for $\lambda = 3.5$ (blue), $\lambda = 4.5$ (green), and $\lambda = 5.5$ (red).
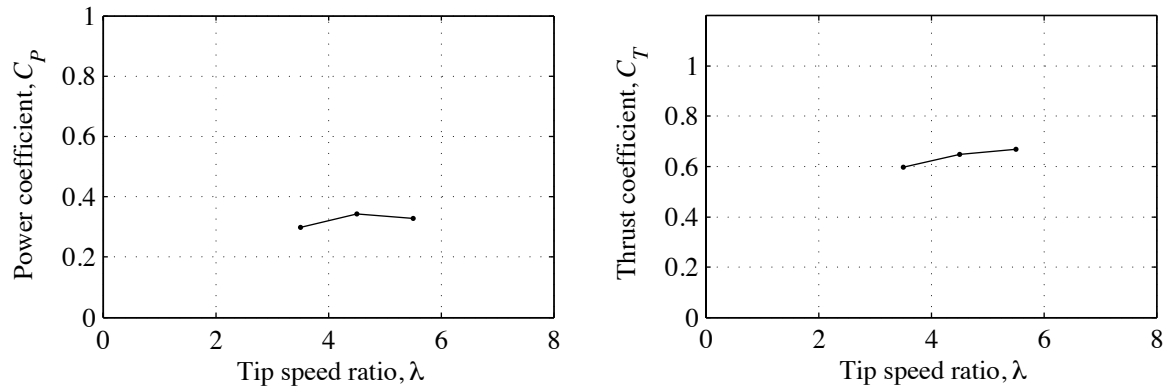
7.12 Case L - 30° Yaw
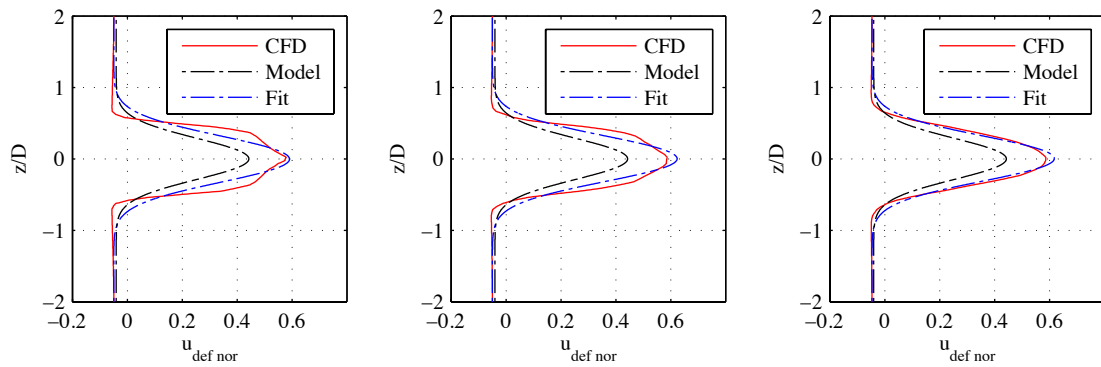

Figure 81: Power and thrust coefficients.

Figure 82: Parametric model of wake velocity deficit ($\lambda = 4.5$; $1D$, $2D$, $5D$).

Figure 83: Root mean square error of least-squares fit to simulation data, showing improvement of agreement with downstream distance ($\lambda = 4.5$).

Figure 84: Centreline normalised velocity deficit profiles for λ = 3.5 (blue), λ = 4.5 (green), and λ = 5.5 (red).

Figure 85: Rotor torque traces for the final revolutions of simulation for λ = 3.5 (blue), λ = 4.5 (green), and λ = 5.5 (red).

7.13 Case M1 - No Tower
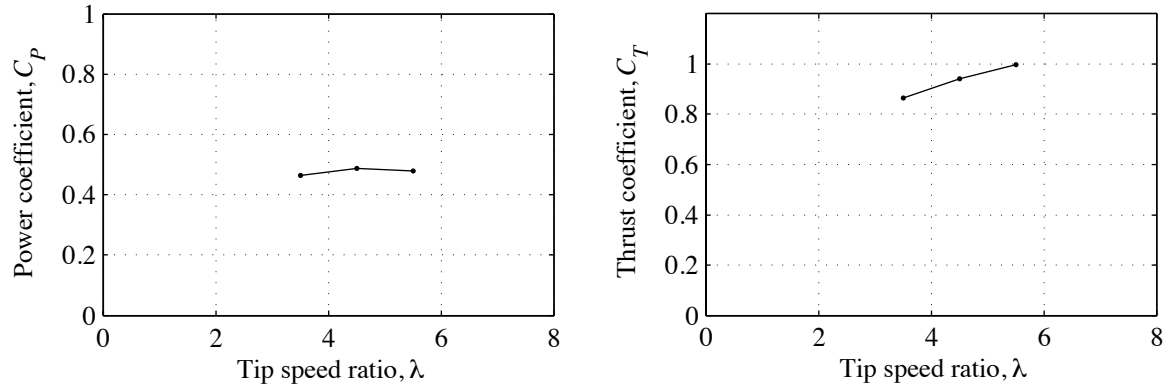
Figure 86: Power and thrust coefficients.
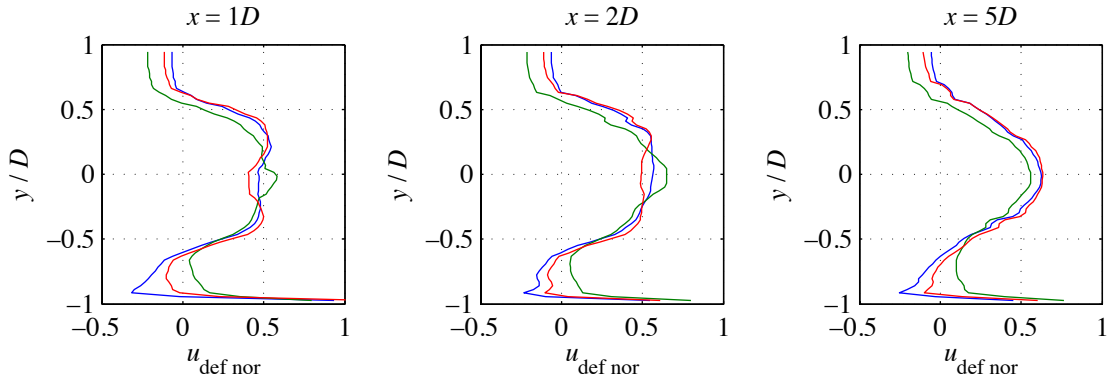
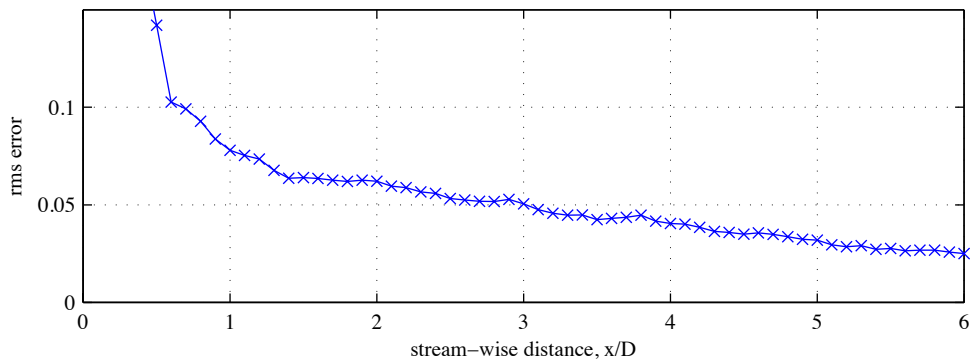Figure 87: Horizontal centre-plane normalised velocity deficit profiles.

Figure 88: Root mean square error of least-squares fit to simulation data, showing improvement of agreement with downstream distance ($\lambda = 4.5$).
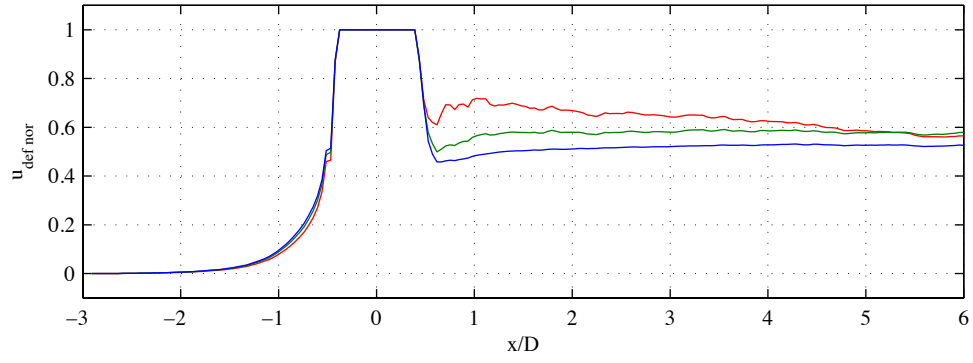
Figure 89: Centreline normalised velocity deficit profiles for λ = 3.5 (blue), λ = 4.5 (green), and λ = 5.5 (red).

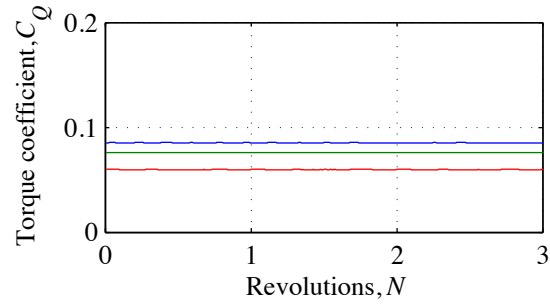
Figure 90: Rotor torque traces for the final revolutions of simulation for λ = 3.5 (blue), λ = 4.5 (green), and λ = 5.5 (red).

7.14 Case M2 - UoE Comparison
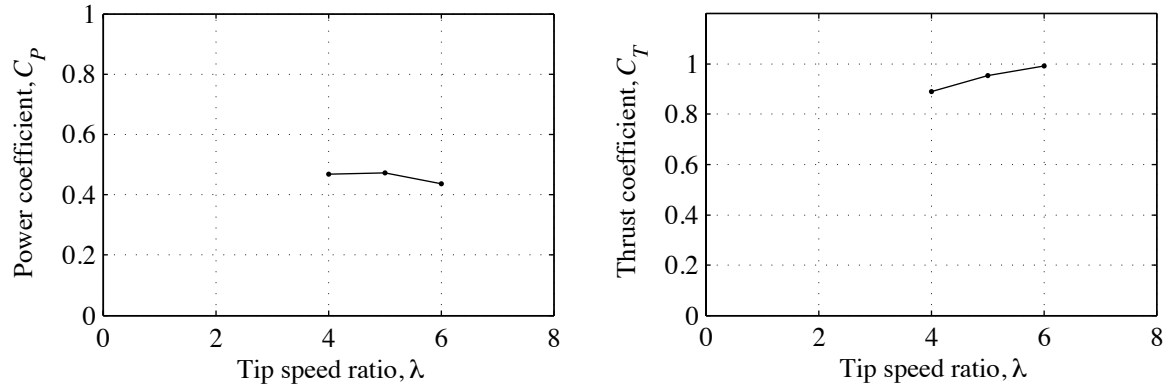
Figure 91: Power and thrust coefficients.
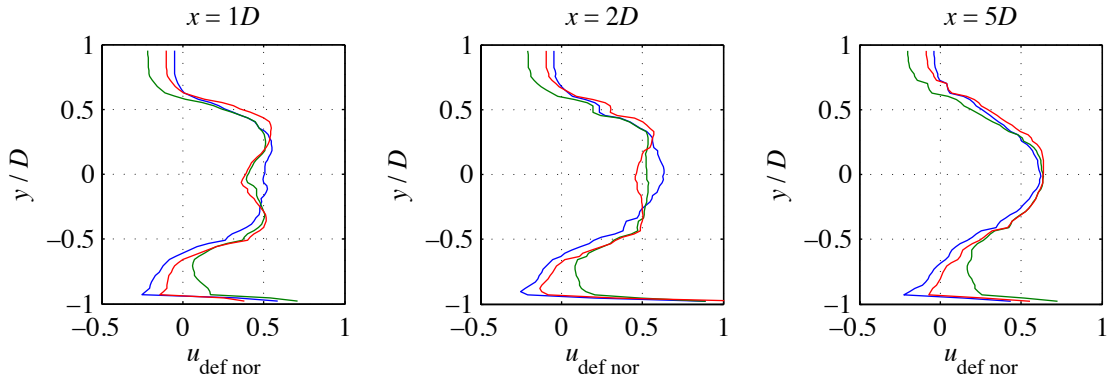
Figure 92: Vertical centre-plane normalised velocity deficit profiles.

Figure 93: Root mean square error of least-squares fit to simulation data, showing improvement of agreement with downstream distance ($\lambda = 4.5$).

Figure 94: Centreline normalised velocity deficit profiles for $\lambda = 3.5$ (blue), $\lambda = 4.5$ (green), and $\lambda = 5.5$ (red).

Figure 95: Rotor torque traces for the final revolutions of simulation for $\lambda = 3.5$ (blue), $\lambda = 4.5$ (green), and $\lambda = 5.5$ (red).

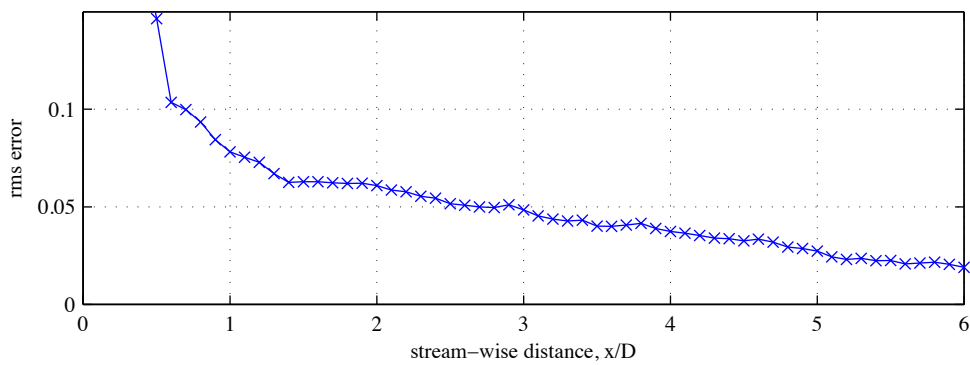## 7.15 Case N - Long Domain
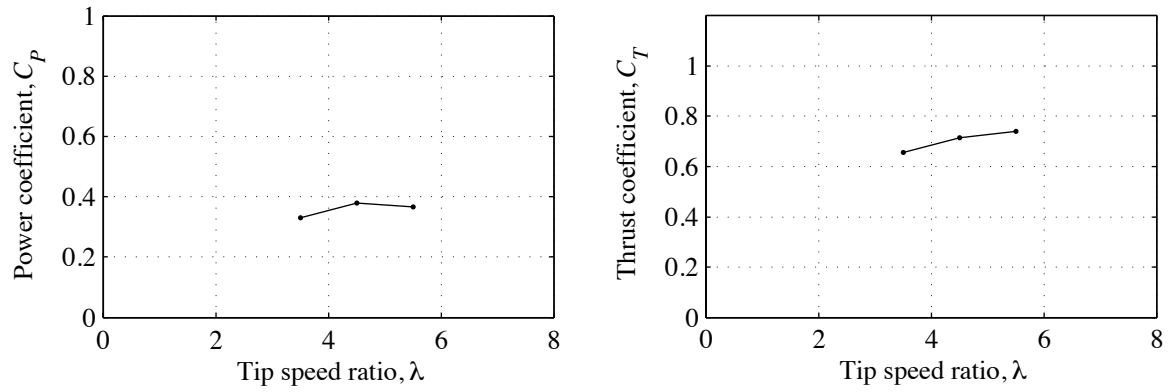
Figure 96: Power and thrust coefficients.
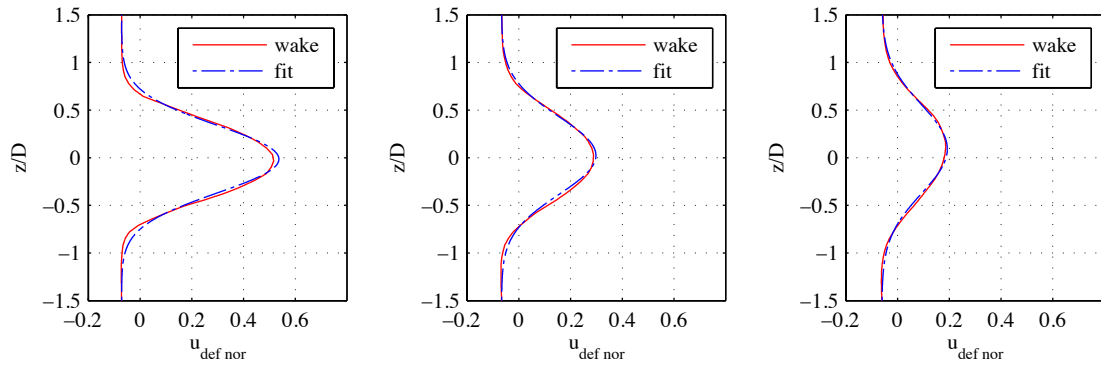
Figure 97: Parametric model of wake velocity deficit (λ = 3.5, 6D 12D 18D).

Figure 98: Parametric model of wake velocity deficit (λ = 4.5, 6D 12D 18D).

Figure 99: Root mean square error of least-squares fit to simulation data, showing improvement of agreement with downstream distance ($\lambda = 4.5$).
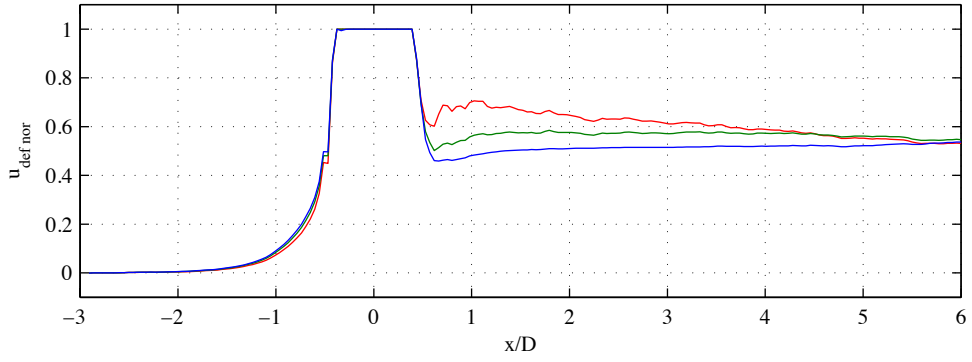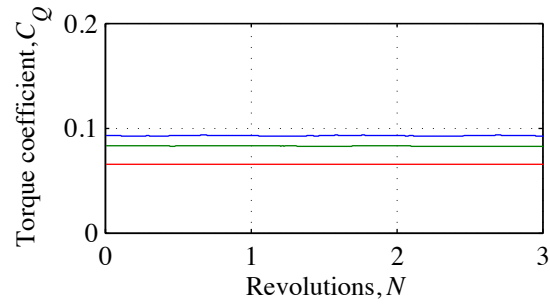

Figure 100: Parametric model of wake velocity deficit ($\lambda = 5.5$, $6D$ $12D$ $18D$).

Figure 101: Centreline normalised velocity deficit profiles for $\lambda = 3.5$ (blue), $\lambda = 4.5$ (green), and $\lambda = 5.5$ (red).

Figure 102: Rotor torque traces for the final revolutions of simulation for $\lambda = 3.5$ (blue), $\lambda = 4.5$ (green), and

$\lambda = 5.5$ (red).

7.16 Case O - Ducted Turbine - Base Case - High Shear
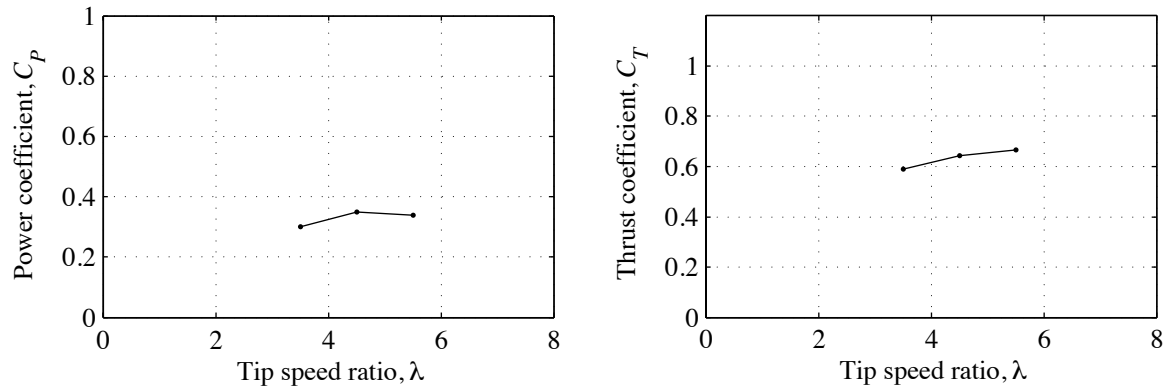

Figure 103: Power and thrust coefficients.
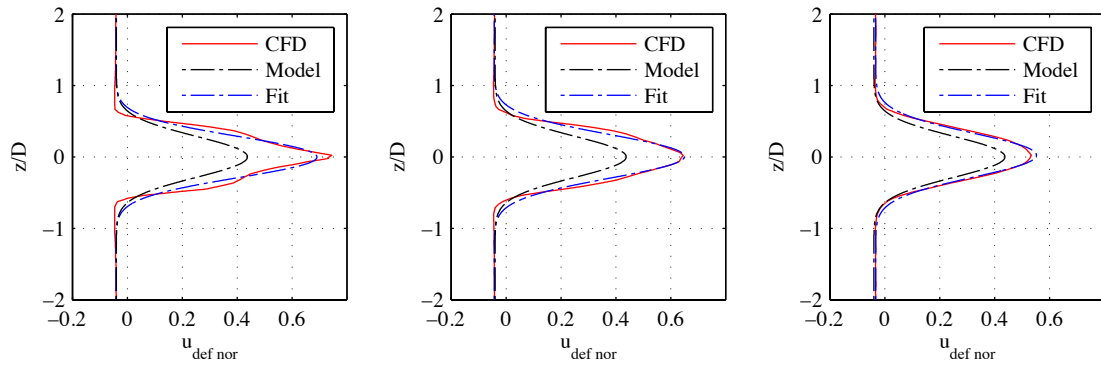
Figure 104: Parametric model of wake velocity deficit (λ = 3.5; 1D, 2D, 5D).
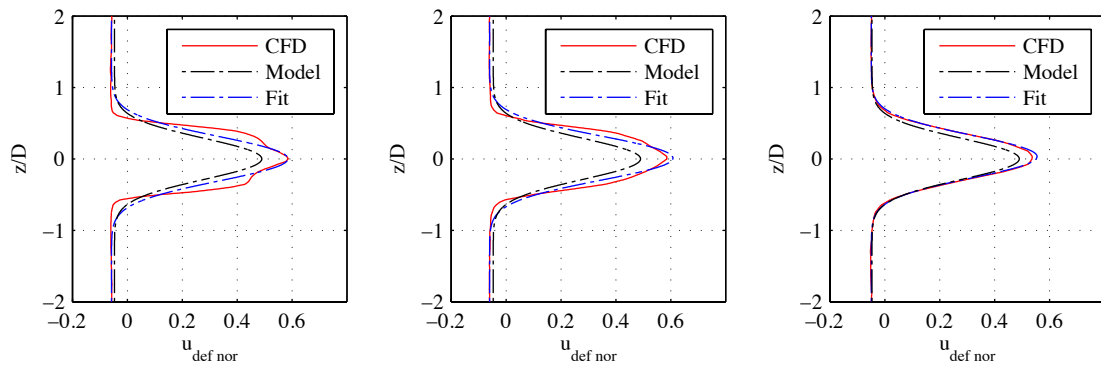

Figure 105: Parametric model of wake velocity deficit (λ = 4.5; 1D, 2D, 5D).
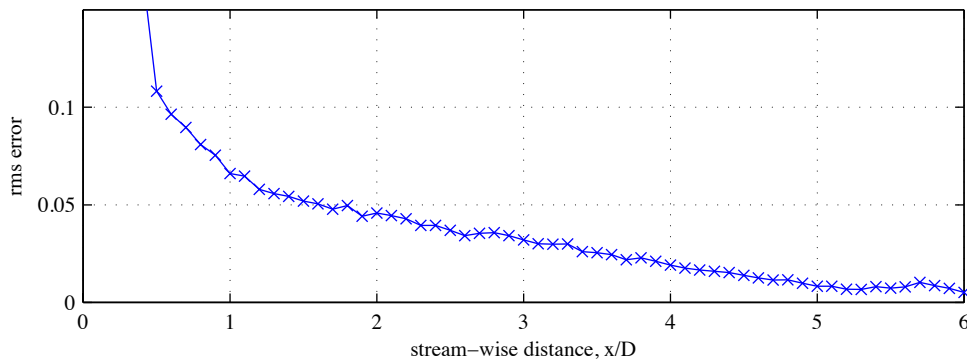
Figure 106: Root mean square error of least-squares fit to simulation data, showing improvement of agreement with downstream distance ($\lambda = 4.5$).
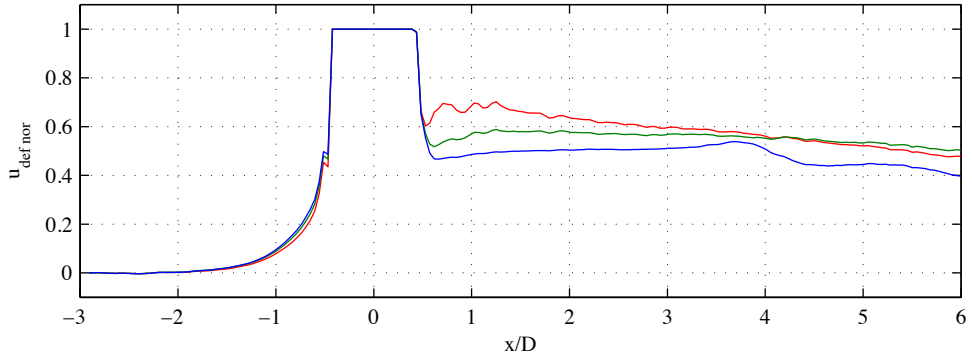

Figure 107: Parametric model of wake velocity deficit ($\lambda = 5.5$; 1D, 2D, 5D).

Figure 108: Centreline normalised velocity deficit profiles for $\lambda = 3.5$ (blue), $\lambda = 4.5$ (green), and $\lambda = 5.5$ (red).
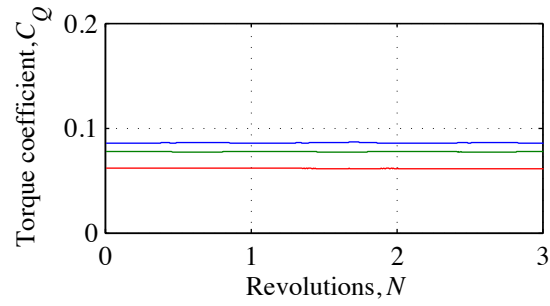
Figure 109: Rotor torque traces for the final revolutions of simulation for λ = 3.5 (blue), λ = 4.5 (green), and λ = 5.5 (red).

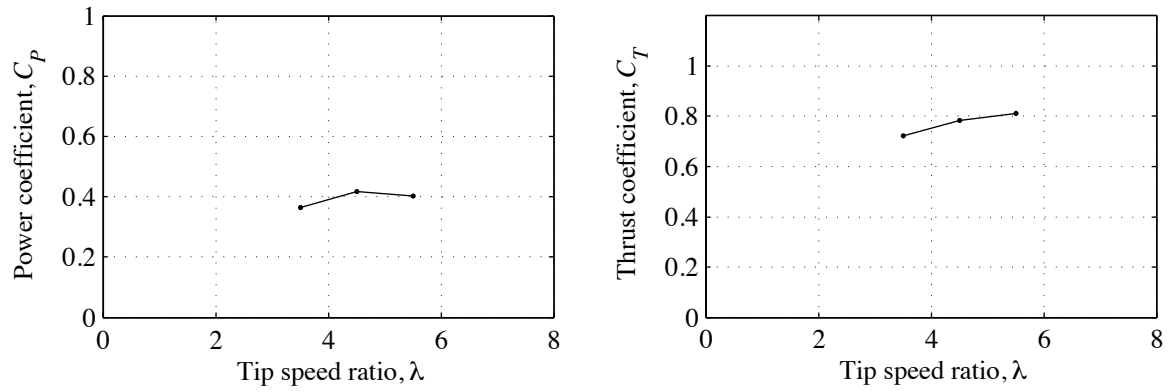## 7.17 Case P - Ducted Turbine - Uniform Flow
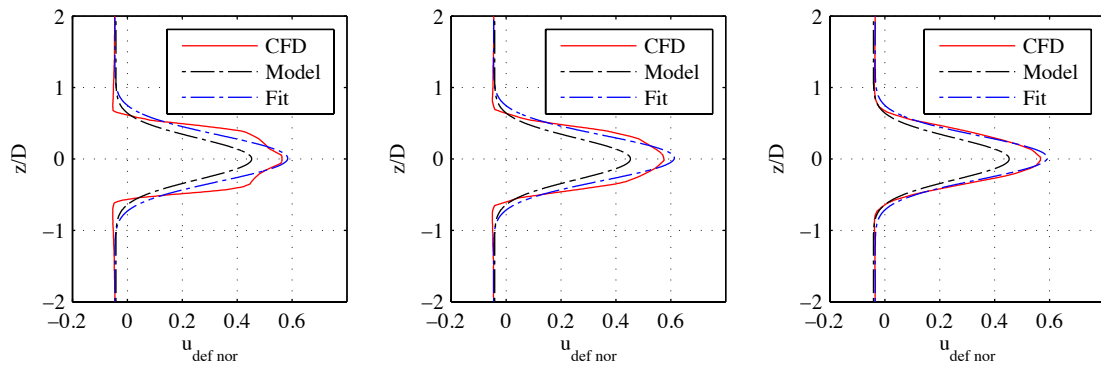

Figure 110: Power and thrust coefficients.

Figure 111: Parametric model of wake velocity deficit (λ = 4.5; 1D, 2D, 5D).
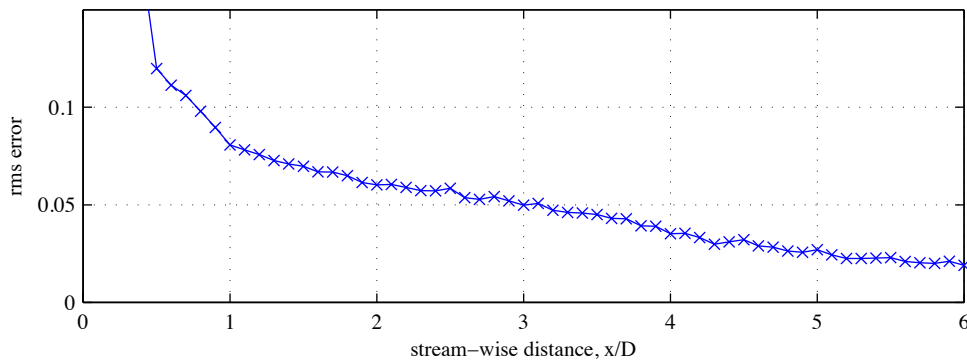

Figure 112: Root mean square error of least-squares fit to simulation data, showing improvement of agreement with downstream distance (λ = 4.5).

Figure 113: Centreline normalised velocity deficit profiles for $\lambda = 3.5$ (blue), $\lambda = 4.5$ (green), and $\lambda = 5.5$ (red).

Figure 114: Rotor torque traces for the final revolutions of simulation for $\lambda = 3.5$ (blue), $\lambda = 4.5$ (green), and $\lambda = 5.5$ (red).

7.18 Case Q - Ducted Turbine - Base Case - Low Shear
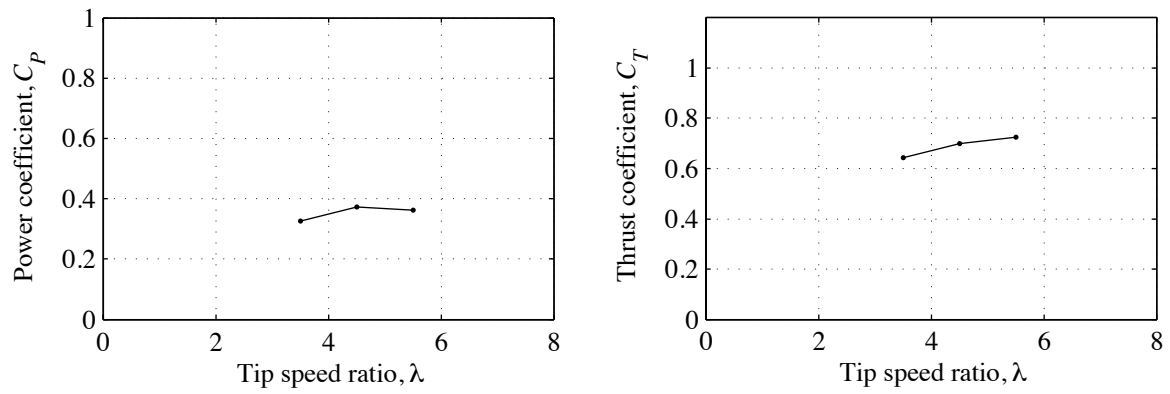
Figure 115: Power and thrust coefficients.
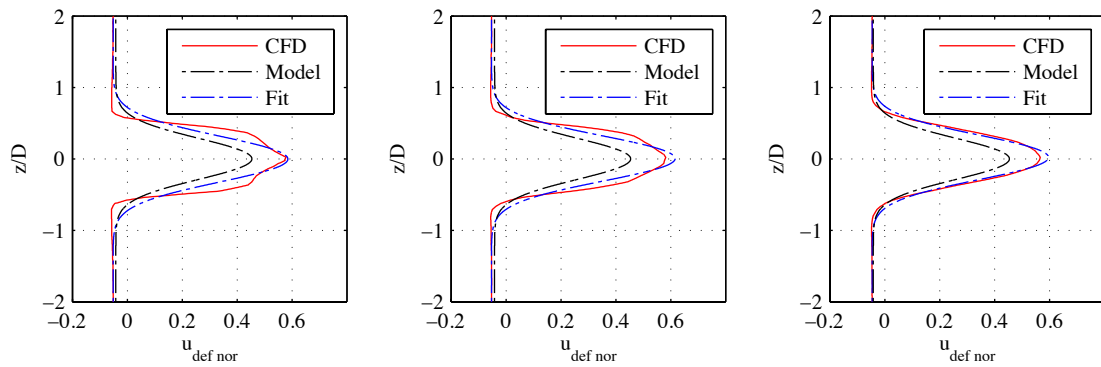
Figure 116: Parametric model of wake velocity deficit ($\lambda = 4.5$; $1D$, $2D$, $5D$).

Figure 117: Root mean square error of least-squares fit to simulation data, showing improvement of agreement with downstream distance ($\lambda = 4.5$).
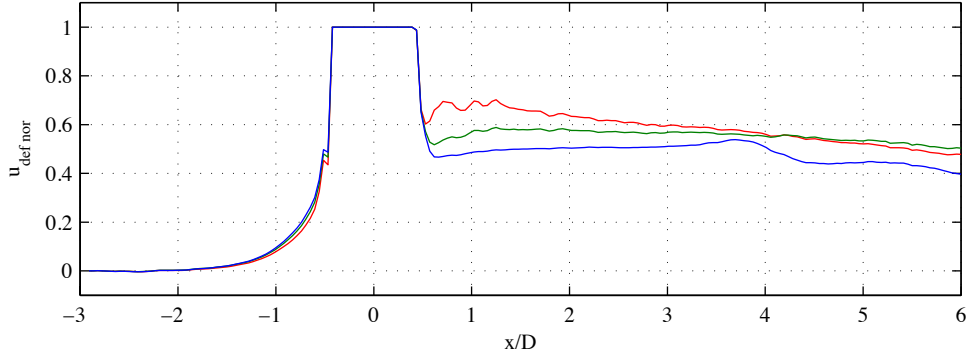
Figure 118: Centreline normalised velocity deficit profiles for $\lambda = 3.5$ (blue), $\lambda = 4.5$ (green), and $\lambda = 5.5$ (red).
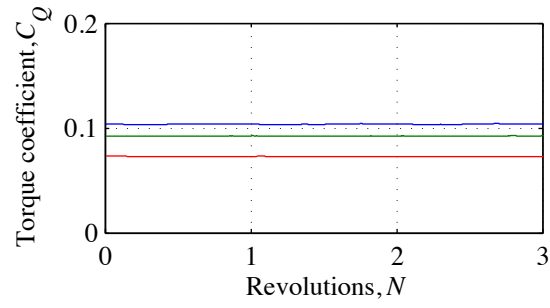

Figure 119: Rotor torque traces for the final revolutions of simulation for $\lambda = 3.5$ (blue), $\lambda = 4.5$ (green), and $\lambda = 5.5$ (red).

7.19 Case R - Ducted Turbine - Low Elevation
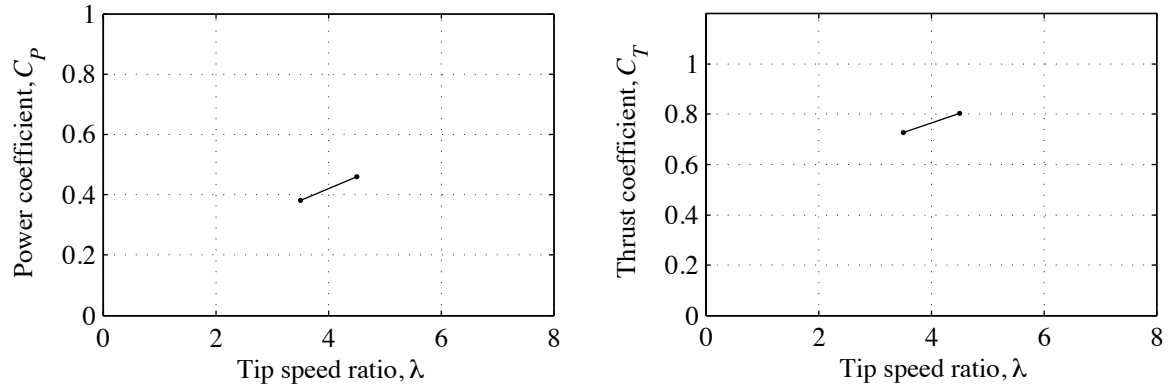

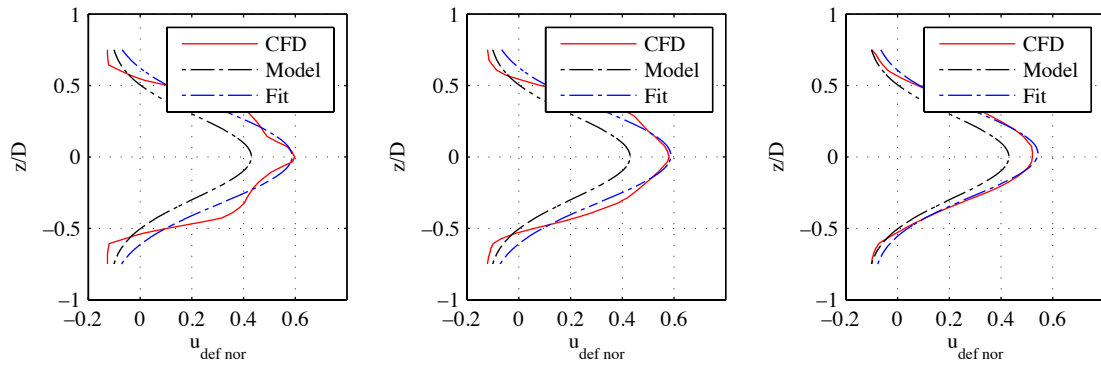Figure 120: Power and thrust coefficients.

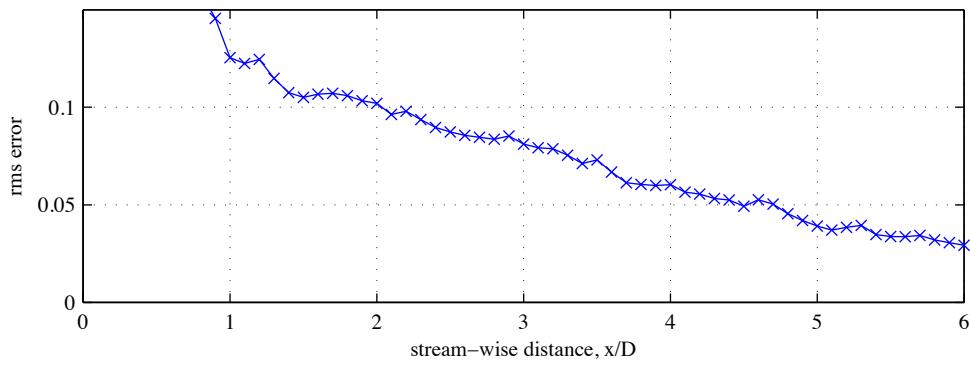Figure 121: Parametric model of wake velocity deficit ($\lambda = 4.5$; $1D$, $2D$, $5D$).

Figure 122: Root mean square error of least-squares fit to simulation data, showing improvement of agreement with downstream distance ($\lambda = 4.5$).
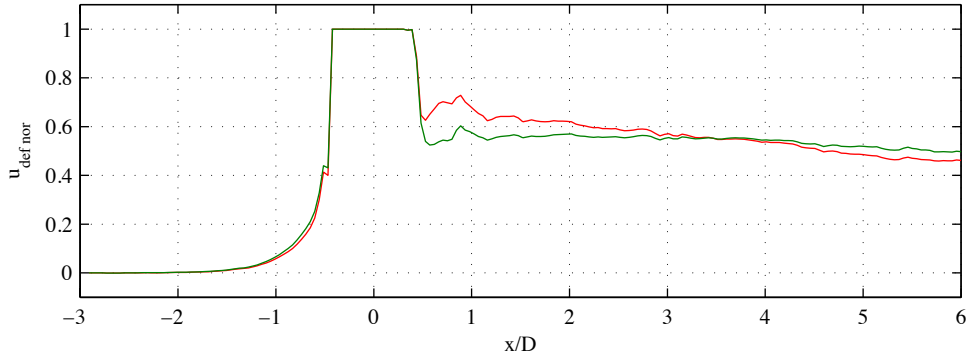
Figure 123: Centreline normalised velocity deficit profiles for $\lambda = 3.5$ (blue), $\lambda = 4.5$ (green), and $\lambda = 5.5$ (red).

Figure 124: Rotor torque traces for the final revolutions of simulation for $\lambda = 3.5$ (blue), $\lambda = 4.5$ (green), and $\lambda = 5.5$ (red).

7.20 Case S - Ducted Turbine - High Elevation

Figure 125: Power and thrust coefficients.

Figure 126: Parametric model of wake velocity deficit ($\lambda = 4.5$; $1D$, $2D$, $5D$).

Figure 127: Root mean square error of least-squares fit to simulation data, showing improvement of agreement with downstream distance ($\lambda = 4.5$).

Figure 128: Centreline normalised velocity deficit profiles for $\lambda = 3.5$ (blue), $\lambda = 4.5$ (green), and $\lambda = 5.5$ (red).
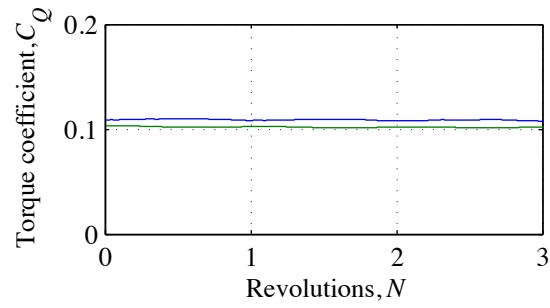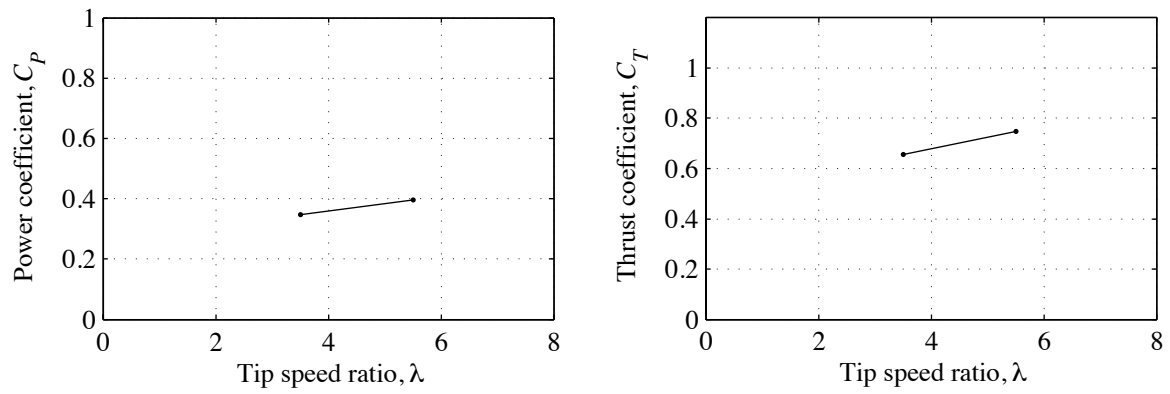

Figure 129: Rotor torque traces for the final revolutions of simulation for $\lambda = 3.5$ (blue), $\lambda = 4.5$ (green), and $\lambda = 5.5$ (red).

7.21 Case T - Ducted Turbine - Narrow Domain

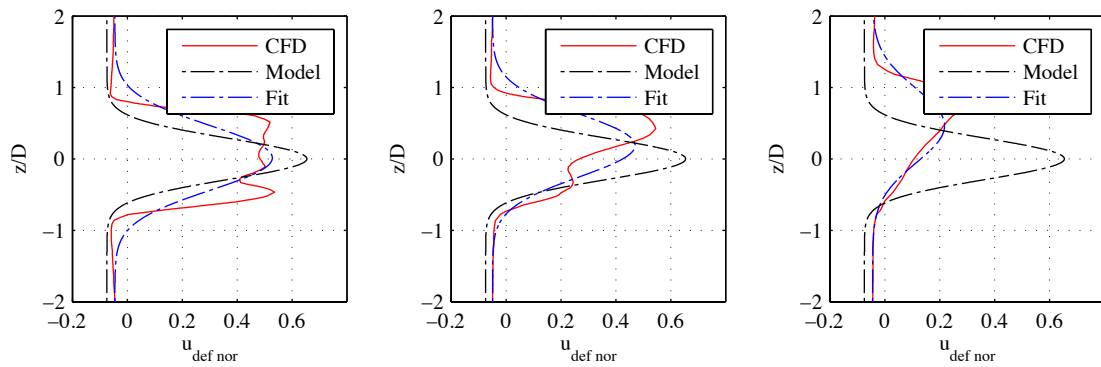Figure 130: Power and thrust coefficients.

Figure 131: Parametric model of wake velocity deficit (λ = 4.5; 1D, 2D, 5D).

Figure 132: Root mean square error of least-squares fit to simulation data, showing improvement of agreement with downstream distance (λ = 4.5).

Figure 133: Centreline normalised velocity deficit profiles for λ = 3.5 (red), λ = 4.5 (green), and λ = 5.5.

Figure 134: Rotor torque traces for the final revolutions of simulation for λ = 3.5 (blue), and λ = 4.5 (green).

7.22 Case U - Ducted Turbine - Low Yaw

Figure 135: Power and thrust coefficients.

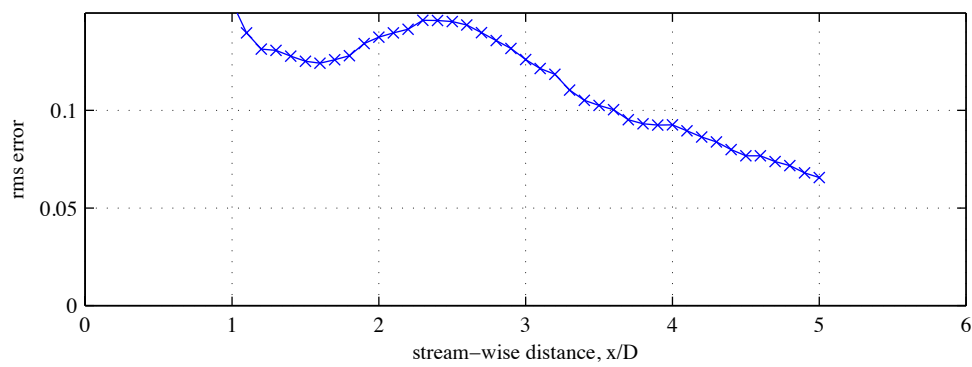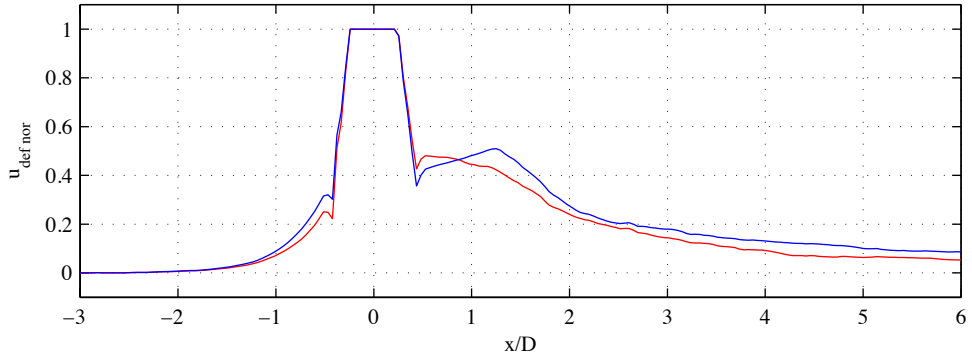Figure 136: Parametric model of wake velocity deficit ($\lambda = 5.5$; $1D$, $2D$, $5D$).

Figure 137: Root mean square error of least-squares fit to simulation data, showing improvement of agreement with downstream distance ($\lambda = 4.5$).

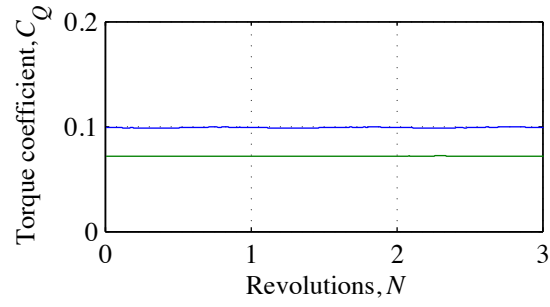Figure 138: Centreline normalised velocity deficit profiles for $\lambda = 3.5$ (blue), and $\lambda = 5.5$ (red).

Figure 139: Rotor torque traces for the final revolutions of simulation for $\lambda = 3.5$ (blue), and $\lambda = 5.5$ (green).

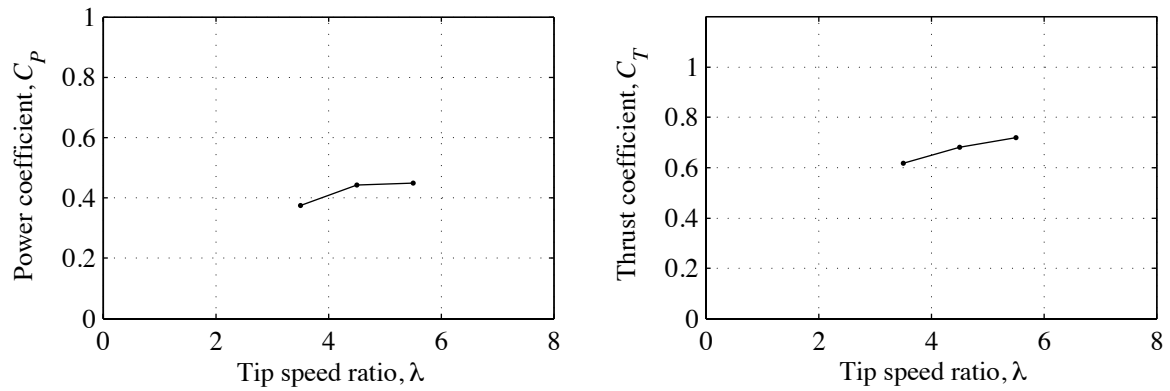## 7.23 Case V - Ducted Turbine - High Yaw
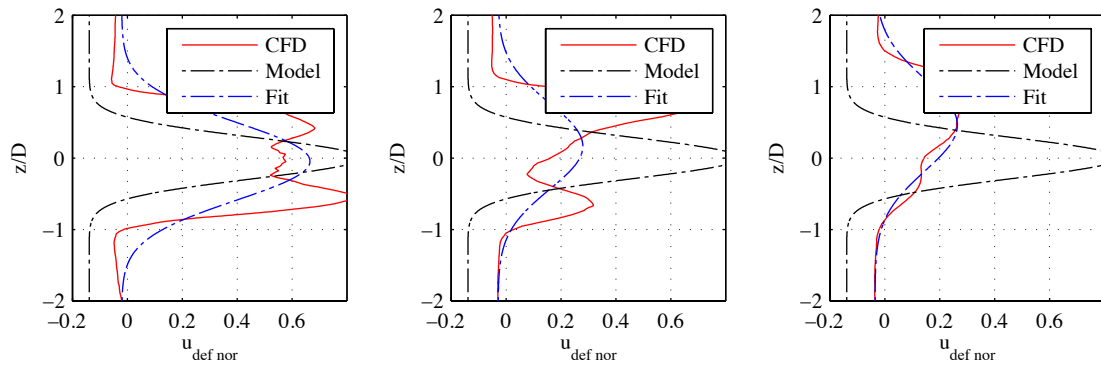

Figure 140: Power and thrust coefficients.

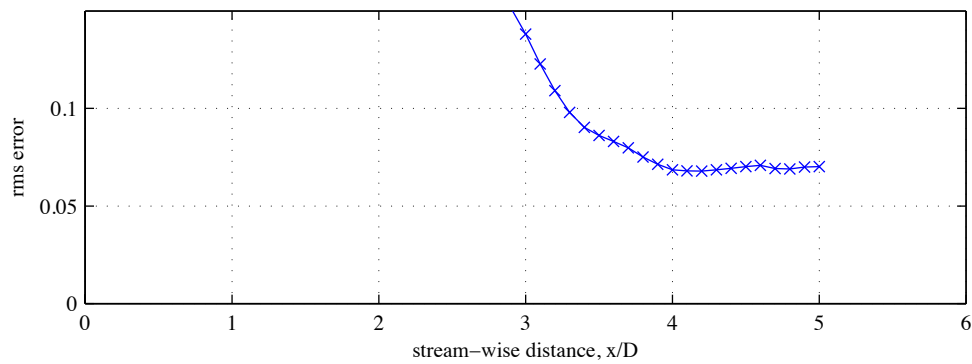Figure 141: Parametric model of wake velocity deficit ($\lambda = 4.5$; 1D, 2D, 5D).

Figure 142: Root mean square error of least-squares fit to simulation data, showing improvement of agreement with downstream distance ($\lambda = 4.5$).
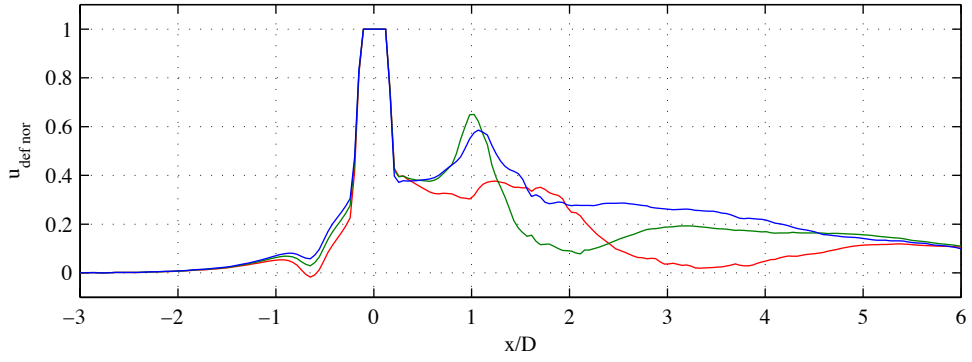
Figure 143: Centreline normalised velocity deficit profiles for λ = 3.5 (blue), λ = 4.5 (green), and λ = 5.5 (red).
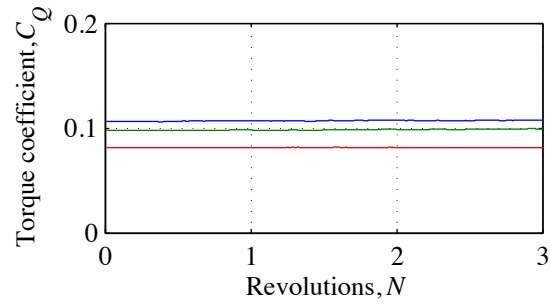

Figure 144: Rotor torque traces for the final revolutions of simulation for λ = 3.5 (blue), λ = 4.5 (green), and λ = 5.5 (red).